Large-scale structure of disc galaxies

Dissertation
zur Erlangung des Doktorgrades
der Mathematisch-Naturwisschenschaftlichen Fakultät
der Christian-Albrechts-Universität
zu Kiel

vorgelegt von
Meng Xiang-Grüß

Kiel
2009

Referent:
Korreferent:
Tag der mündlichen Prüfung:
Zum Druck genehmigt:

der Dekan

Für meine Eltern

Zusammenfassung

In der vorliegenden Doktorarbeit wird im ersten Teil der Zusammenhang zwischen senkrechten Magnetfeldern und dunkler Materie in Scheibengalaxien untersucht. Unter der Annahme, dass die untersuchten Störungen in diesen Galaxien stationär sind, leiten wir den mathematischen Zusammenhang zwischen der Masse der dunklen Materie und der magnetischen Feldstärke her. Dabei finden wir heraus, dass bereits mittlere Magnetfeldstärken mit der Masse der dunklen Materie stark korrelieren. Eine geringfügige Verstärkung des Magnetfeldes kann schon dazu führen, dass die Komposition aus einem stationären Zustand gebracht wird. Umgekehrt kann durch Variation der Magnetfeldstärke eine stationäre Struktur entstehen.

Im zweiten Teil wird die zeitliche Entwicklung von Scheibengalaxien mithilfe des N-body / SPH (smoothed particle hydrodynamics)-Codes GADGET-2 numerisch untersucht. Durch Verwendung von drei unterschiedlichen Methoden versuchen wir langlebige Dichtewellen in der Scheibe zu erzeugen, die zu der sogenannten ‘grand-design’ Struktur führen. Dabei werden Sternentstehung und stellares Feedback in Form von Supernova Explosionen berücksichtigt. Alle drei Methoden sind in der Lage, die erwünschten grand-design Spiralstrukturen zu erzeugen. Jedoch sind die Strukturen nach einer kurzen Zeitdauer verschwunden. Anhand einiger Beispiele wird gezeigt, dass der Grund für das schnelle Verschwinden in der Natur der Spiralarme liegt. Bei den erzeugten Spiralarmen handelt es sich stets um Materiearme, aber nicht um die erforderlichen klassischen Dichtewellen der Dichtewellentheorie. Materiearme bestehen aus denselben Teilchen und wickeln sich mit der Zeit auf. Dies ist bei den Simulationsergebnissen sichtbar. Die Gründe für das Ausbleiben der Dichtewelle und weitere notwendige Simulationen werden zum Schluss diskutiert.

Abstract

In the first part of the thesis at hand, the relation between vertical magnetic fields and dark matter in disc galaxies is studied. Under the assumption that the studied perturbations in these galaxies are stationary, we derive a mathematical relation between the mass of the dark matter and the magnetic field strength. Thereby, we find that already medium magnetic field strengths strongly correlate with the mass of the dark matter. A slight enhancement of the magnetic field can already destroy the stationarity of a composition. Vice versa a stationary structure can be produced by variation of the magnetic field strength.

In the second part the time evolution of an isolated galaxy by means of the N-body / SPH (smoothed particle hydrodynamics) code GADGET-2 is studied numerically. By applying three different methods, we try to produce long-lived density waves in the disc, which lead to the so-called 'grand-design' structure. Star formation and stellar feedback in terms of supernova explosions are included. All three methods are able to produce the desired grand-design spiral structures. However, the structures disappear after a short time span. With several examples, we show that the reason for the fast disappearance lies in the nature of the spiral arms. The created spiral arms are always material arms but not the required classical density waves of the density wave theory. Material arms consist of the same particles and wind up with time. This is visible in the simulation results. The reasons for the absence of the density wave and further simulations to be done are discussed finally.

Contents

1 Introduction

More than 50 % of all galaxies in the universe belong to the class of spiral galaxies. Spiral galaxies generally consist of a flat disc and a central concentration of stars which is called bulge. The disc is composed of gas, dust and stars. Today, it is also well accepted that the visible components of spiral galaxies are embedded in a huge spherical halo composed of dark matter particles.

Spiral galaxies can be classified into grand-design and flocculent spiral galaxies according to their large-scale appearance. Grand-design spiral galaxies have long spiral arms (usually two arms), which are highly symmetric. In comparison to that, flocculent spiral galaxies show multiple spiral arms, which are arranged more or less irregularly around the center of the galaxy. Figure 1.1 shows two prominent examples of a grand-design (picture on the left) and a flocculent spiral galaxy (picture on the right). Tightly wound spiral arms can be found in grand-design as well as in flocculent spiral galaxies. They are characterized by a very small pitch angle of the arms.

The search for the different mechanisms which can produce such various spiral patterns in the galaxies is one of the most challenging on-going research since more than 40 years.

Today, there are two different approaches to describe grand-design spiral galaxies. Based on observations of merging events, such as M51, the idea came upon astronomers in the 60s, that grand-design spiral galaxies could be produced by interactions between galaxies and companions (Toomre & Toomre 1972). Subsequent numerical studies have shown that the grand-design spiral structure in a galaxy can indeed be produced by gravitational interactions (e. g. Toomre & Toomre 1977). But although companions can be observed for many spiral galaxies, a general claim that all grand-design spiral structures in the universe are produced by gravitational interaction events is not possible since there are still grand-design spiral galaxies without visible companions. Also, the time evolution of spiral structures produced by this way must still be studied in detail.

The second and most promising theory for the description of long-lived grand-design spiral

Figure 1.1: The grand-design spiral galaxy M81 (left), Credit: NASA/JPL-Caltech and flocculent spiral galaxy NGC 2841 (right), Credit: NASA/JPL-Caltech

galaxies is the density wave theory first introduced by Lin & Shu in 1964. The density wave theory (DWT) describes the grand-design spiral structure as a quasi-stationary structure produced by the propagation of a density perturbation in a disc. However, due to the viscosity in a real disc and the radial propagation of the density wave (Toomre 1969), the density wave cannot persist for a long time. Also the origin of the density wave is unknown. These two problems have dominated the study of density waves during the last 40 years.

As can be seen from the above two theories, the description of grand-design spiral galaxies is still uncomplete. The main goal of this work is therefore to study grand-design spiral galaxies by using previous theoretical results and current computational capacities.

The following work is devided into two parts. In the first part, a modified form of the density wave theory is used for studying possible relations between dark matter content and magnetic field strength of a disc galaxy. In the second part, the evolution of disc galaxies is studied with numerical simulations. The main goal of the second part is a numerical production of large-scale density waves and the study of the lifetime of density waves.

2

Dark matter and magnetic fields in disc galaxies

2.1 Introduction

Since the seminal studies of the galactic density wave theory in the 1960's pioneered by Lin & Shu (1964, 1966), a lot of advanced work has been done to describe the large-scale dynamics of 'grand-design' spiral structures in disc galaxies. In terms of theoretical development, it is natural to first concentrate on linear perturbation theories. As synchrotron radio observations have revealed since the early 1970's that magnetic fields are ubiquitous in disc galaxies (e.g. Sofue, Fujimoto & Wielebinski 1986; Beck et al. 1996; Zweibel & Heiles 1997; Brown, Taylor, Wielebinski & Mueller 2003), magnetic fields have been recognized as an important aspect in the model treatment of spiral galaxies and thus the magnetohydrodynamic (MHD) density wave theory was developed (Fan & Lou 1997; Lou & Fan 1998). Over the past decade, a research area has been developed on the so-called scale-free discs and perturbation structures therein (e.g. Syer & Tremaine 1996; Shu et al. 2000; Shen & Lou 2004; Lou & Zou 2004; Shen, Liu & Lou 2005; Lou & Zou 2006; Wu & Lou 2006; Lou & Bai 2006). The scale-free condition corresponds to a power-law dependence of all physical quantities on the cylindrical radius r. As an example, the background surface mass density is $\Sigma_0 \propto r^{-2\beta-1}$ with β being a constant scaling index. Such analysis was first initiated for relatively simple models of only one gas disc. We are now able to explore a composite system of a stellar disc and an isopedically magnetized gas disc embedded in a dark matter halo. For this overall configuration, we study possible large-scale perturbation structures and stationary MHD density waves. To simplify the mathematical treatment, the stellar disc is approximated as a fluid and the magnetized gaseous disc as a magnetofluid. Both are

assumed to be geometrically razor-thin and scale-free discs. In general, the scaling exponent β may vary radially in a certain range for different disc galaxies. For roughly flat rotation curves which can be grossly determined in many spiral galaxies from large radii to the centre (e.g. Bosma 1981; Persic & Salucci 1988; Persic et al. 1996), index β may be regarded as zero. According to the classical Newtonian gravity theory, a significantly larger amount of mass than the visible mass of the disc is needed in order to sustain observed grossly flat rotation curves. As a consequence of this discrepancy between the visible and the required mass as well as the disc stability property, the presence of a massive dark matter halo has been proposed (e.g. Ostriker & Peebles 1973; Ostriker et al. 1974; Binney & Tremaine 1987). Nowadays, the inclusion of a massive axisymmetric dark matter halo is a common practice for studying large-scale galactic dynamics.

Meanwhile, observations of disc galaxies can be used to estimate open magnetic field strengths and configurations on both sides of a galactic disc plane. While these open magnetic fields are most certainly interlaced with closed coplanar magnetic fields, at this stage of our theoretical model development, we consider only open magnetic fields crossing the disc plane almost vertically.[1] Shu & Li (1997) introduced the so-called isopedic condition of $B_z(r,\ \theta,\ t) \propto \Sigma^{(g)}$ where B_z is the $z-$component of the magnetic field and $\Sigma^{(g)}$ is the gas disc surface mass density. The ratio $\Sigma^{(g)}/B_z$ thus remains constant in time and space. This situation is referred to as the isopedic magnetic field configuration. In fact, this constant ratio can be actually inferred by the magnetic field-freezing effect according to the ideal magnetohydrodynamic (MHD) equations (Lou & Wu 2005). Effective modifications to the gravitational potential and the gas pressure are derived by Shu & Li (1997) for a single isopedically magnetized gas disc. This isopedic condition was first proposed as an *ansatz* based on numerical simulations of magnetized cloud core formation through ambipolar diffusions (e.g. Nakano 1979; Lizano & Shu 1989; Shu & Li 1997 and references therein). On the basis of earlier work of Shu & Li (1997), Lou & Wu (2005) generalize their results into theorems for two gravitationally coupled discs where only the gas disc is isopedically magnetized. Moreover, they actually demonstrated that a constant ratio $\lambda = 2\pi\sqrt{G}\Sigma^{(g)}/B_z$, with G being the gravitational constant, can be proved as a consequence of frozen-in condition by the standard ideal nonlinear MHD equations. In this model analysis, we shall adopt the same expressions of Lou & Wu (2005) for the effect of an isopedic magnetic field anchored in the gas disc component.

In order to catch the essence of MHD density wave equations from analytical and numerical explorations, a few assumptions and simplifications are invoked such as the stationary condition in our frame of reference. As first advanced and hypothesized by Lin & Shu (1966), the quasi-stationary spiral structure (QSSS) has been studied since the early 1960's (e.g. Bertin & Lin 1996

[1]The studies of coplanar magnetic fields in a rotating thin disc system can for example be found in Lou & Zou (2004, 2006) and Lou & Bai (2006).

and extensive references therein). There the pattern speed of density wave travels very slowly compared to the differential rotation speed v_θ of the disc matter. Our stationary requirement can be simply regarded as a limiting case of the QSSS approximation. Based on observations of the nearby spiral galaxy M81, Visser (1980a, b) has shown that the density wave theory does indeed account for gross aspects of the large-scale dynamics of this spiral galaxy.

Kendall et al. (2008) presented further observational data analysis of galaxy M81, where the large-scale spatial offset between the (old) stellar spiral wave and the gas shock front was examined. Theoretical considerations (e.g. Gittins & Clarke 2004; Chakrabarti 2008) have shown that the offset between the gas shock front (i.e. the maximum gas density) and the spiral potential minimum (determined by the spiral pattern in the old stellar disc component) may yield clues about the lifetime of a spiral pattern. By comparing observational results with the predictions of Gittins & Clarke (2004), Kendall et al. (2008) found that galaxy M81 probably possesses a long-lived spiral pattern. Regarding the spiral structure in the gaseous disc component, Chakrabarti et al. (2003) have shown, that the so-called ultraharmonic resonances that the gas experiences in a fixed stellar spiral potential can lead to highly time-dependent gas responses, not allowing long-lived spiral patterns in the gas disc. In our model of a composite disc system, there is no fixed stellar potential but rather stellar and gaseous discs are gravitationally coupled to each other in terms of dynamical adjustment. While the simulation results reveal only a long-lived stellar spiral pattern, for our semi-analytical calculations, a stationary requirement for both spiral patterns in stellar and gaseous discs may be imposed without inconsistency. This offers a useful construct for modelling large-scale patterns in isopedically magnetized spiral galaxies.

Theoretically, two classes of stationary MHD density wave solutions with in-phase and out-of-phase density perturbations are expected to exist in a composite disc system according to Lou & Shen (2003). The physical reason for these two different couplings between the stellar and gaseous discs is a dynamic interplay between star formation and gas clumping processes (Shen & Lou 2004). When the surface mass densities are out of phase, the self-gravity of the composite disc system is reduced. The azimuthal propagation of the density wave is therefore faster and if a stationary configuration is desired, then the disc should rotate faster. When the surface mass densities are in phase, the self-gravity is enhanced. The azimuthal propagation of the density wave is slower and the disc should then rotate slower in order to maintain a stationary configuration (Lou & Shen 2003).

Our present investigation mainly focuses on the variation of the amount of dark matter in the halo needed to sustain stationary perturbation configurations as the isopedic magnetic field strength varies. Therefore, we use typical values of disc galaxies for different parameters such as the ‘sound speed’ or the surface mass density. By invoking several physical requirements for the dark matter halo such as a non-negative potential ratio, the physical parameter range of stationary

perturbation solutions can be identified.

In Section 2.2, the problem formulation, the basic formulae and the coupled fluid and magnetofluid equations for the two discs are presented. In Section 2.3, the scale-free condition for the parameters is introduced. In Section 2.4, we discuss effective modifications to the gravitational potential and the enthalpy in the gas disc when an isopedic magnetic field is introduced. In Section 2.5, several relevant relations for the background rotational equilibrium configuration are derived. In Section 2.6, MHD perturbations are introduced and the relevant global stationary dispersion relation is derived. For globally stationary MHD perturbation configurations, we calculate the dark matter amount and discuss which parameters affect this amount. Section 2.7 describes briefly the values for the parameters adopted for this model analysis. In Section 2.8, aligned cases are studied where perturbations of different radii can be aligned radially. In Section 2.9, unaligned logarithmic spiral cases with a constant radial flux of angular momentum are studied. Such unaligned cases have MHD perturbations which are systematically phase shifted azimuthally as a function of radius r. In unaligned cases, MHD density waves propagate in both azimuthal and radial directions. The constant radial flux of angular momentum is realized by setting the perturbation scale-free index β_1 to $1/4$ (e.g. Goldreich & Tremaine 1979; Shen et al. 2005). In Section 2.10, we discuss two limiting cases of no magnetic field and only a single isopedically magnetized gaseous disc. In the last Section 2.11, we summarize our work and draw conclusions.

2.2 Nomenclature and magnetohydrodynamic (MHD) equations

We first introduce notations for the relevant physical variables used in our model formulation and analysis. We largely adopt the same nomenclature of Wu & Lou (2006) for a model of a single scale-free disc with an isopedic magnetic field. Whenever the superscript (i) is attached to a physical variable, the relevant equation is valid for both stellar (s) and gaseous (g) discs in parallel. Cylindrical coordinates $(r,\ \theta,\ z)$ are adopted for our model formulation and we confine our analysis within the $z = 0$ plane for an infinitely thin composite disc system in differential rotation. For example, variable $\Sigma^{(s)}(r,\ \theta,\ t)$ is the two-dimensional surface mass density of the stellar disc and $\Sigma^{(g)}(r,\ \theta,\ t)$ is that of the isopedically magnetized gas disc. The total surface mass density $\Sigma(r,\ \theta,\ t) = \Sigma^{(s)} + \Sigma^{(g)}$ is the sum of these two disc surface mass densities. Two different coplanar bulk flow velocities are possible in the two discs: the radial bulk flow velocity $v_r^{(i)}(r,\ \theta,\ t)$ and the azimuthal bulk flow velocity $v_\theta^{(i)}(r,\ \theta,\ t)$. For the background rotational equilibrium disc configuration of axisymmetry, the radial flow velocities should vanish. The two-dimensional pressure (i.e. vertically integrated pressure) in each disc is described by $\Pi^{(i)}(r,\ \theta,\ t)$. Between

the two-dimensional variables and their three-dimensional counterparts, the following integral relations exist,

$$\Pi^{(i)}(r,\ \theta,\ t) = \int\limits_{\Delta z} p^{(i)}(r,\ \theta,\ z,\ t)dz\ , \quad \Sigma^{(i)}(r,\ \theta,\ t) = \int\limits_{\Delta z} \rho^{(i)}(r,\ \theta,\ z,\ t)dz\ , \tag{2.1}$$

where $p^{(i)}$ is the three-dimensional pressure and $\rho^{(i)}$ is the three-dimensional mass density, and Δz is the disc thickness presumed to be very small compared to radius r. Thus, $\Pi^{(i)}$ is the vertical integral of pressure $p^{(i)}$. The three-dimensional polytropic equation of state is $p^{(i)} = k_3^{(i)}[\rho^{(i)}]^{\gamma}$, with γ being the polytropic index and $k_3^{(i)}$ being related to the disc entropy. The vertically integrated barotropic equation of state can then be expressed as

$$\Pi^{(i)} = k^{(i)} \left[\Sigma^{(i)}\right]^n\ , \tag{2.2}$$

where index $n > 0$ is the barotropic index, $k^{(i)} > 0$ for a *warm* disc and $k^{(i)} = 0$ for a *cold* disc. The barotropic sound speed $a^{(i)}$ in each disc is then defined by

$$\left[a^{(i)}\right]^2 = \mathrm{d}\Pi^{(i)}/\mathrm{d}\Sigma^{(i)} = nk^{(i)}\left[\Sigma^{(i)}\right]^{n-1} = n\Pi^{(i)}/\Sigma^{(i)}\ . \tag{2.3}$$

The 'sound speed' $a^{(s)}$ in the stellar disc is effectively related to the velocity dispersion of stars. The enthalpy $H^{(i)}$ in each disc is given by

$$H^{(i)} = \int \frac{\mathrm{d}\Pi^{(i)}}{\Sigma^{(i)}} = \frac{nk^{(i)}[\Sigma^{(i)}]^{n-1}}{(n-1)} = \frac{[a^{(i)}]^2}{(n-1)} \tag{2.4}$$

and is proportional to the square of 'sound speed' in each disc. The gravitational coupling between the stellar and magnetized gaseous discs is described by the well-known Poisson integral

$$\Phi(r,\theta,t) = \oint \mathrm{d}\psi \int \frac{-\mathrm{G}\Sigma(r',\ \psi,\ t)r'\mathrm{d}r'}{[r'^2 + r^2 - 2rr'\cos(\psi-\theta)]^{1/2}}\ , \tag{2.5}$$

where $\mathrm{G} = 6.67 \times 10^{-8}\ \mathrm{g}^{-1}\ \mathrm{cm}^3\ \mathrm{s}^{-2}$ is the gravitational constant. The gravitational potentials of the two discs can be separately written as

$$\Phi^{(s)}(r,\theta,t) = \oint \mathrm{d}\psi \int \frac{-\mathrm{G}\Sigma^{(s)}(r',\ \psi,\ t)r'\mathrm{d}r'}{[r'^2 + r^2 - 2rr'\cos(\psi-\theta)]^{1/2}}\ , \tag{2.6}$$

$$\Phi^{(g)}(r,\theta,t) = \oint \mathrm{d}\psi \int \frac{-\mathrm{G}\Sigma^{(g)}(r',\ \psi,\ t)r'\mathrm{d}r'}{[r'^2 + r^2 - 2rr'\cos(\psi-\theta)]^{1/2}}\ , \tag{2.7}$$

with $\Phi = \Phi^{(s)} + \Phi^{(g)}$. In a disc galaxy, an axisymmetric massive dark matter halo is represented by a gravitational potential $\overline{\Phi}$. A recent numerical exploration (e.g. Diemand et al. 2008) has shown that the dark matter halo is not smooth and uniform, but rather consists of many smaller clumpy subhalos. For simplicity, we assume the dark matter halo to be grossly axisymmetric on large scales and unperturbed in our model analysis at this stage. The composite system of two coupled discs with an axisymmetric dark matter halo is described by coupled nonlinear fluid equations $(2.8) - (2.10)$ below.

$$\frac{\partial \Sigma^{(i)}}{\partial t} + \frac{1}{r}\frac{\partial}{\partial r}\left[r\Sigma^{(i)}v_r^{(i)}\right] + \frac{1}{r}\frac{\partial}{\partial \theta}\left[\Sigma^{(i)}v_\theta^{(i)}\right] = 0\,, \tag{2.8}$$

$$\frac{\partial v_r^{(i)}}{\partial t} + \frac{v_r^{(i)}\partial v_r^{(i)}}{\partial r} + \frac{v_\theta^{(i)}}{r}\frac{\partial v_r^{(i)}}{\partial \theta} - \frac{\left[v_\theta^{(i)}\right]^2}{r} =$$
$$= -\frac{1}{\Sigma^{(i)}}\frac{\partial \Pi^{(i)}}{\partial r} - \frac{\partial(\Phi+\overline{\Phi})}{\partial r} = -\frac{\partial\left[H^{(i)}+\Phi+\overline{\Phi}\right]}{\partial r}\,, \tag{2.9}$$

$$\frac{\partial v_\theta^{(i)}}{\partial t} + v_r^{(i)}\frac{\partial v_\theta^{(i)}}{\partial r} + \frac{v_\theta^{(i)}}{r}\frac{\partial v_\theta^{(i)}}{\partial \theta} + \frac{v_\theta^{(i)}v_r^{(i)}}{r} =$$
$$= -\frac{1}{\Sigma^{(i)}}\frac{\partial \Pi^{(i)}}{r\partial \theta} - \frac{\partial(\Phi+\overline{\Phi})}{r\partial \theta} = -\frac{\partial\left[H^{(i)}+\Phi+\overline{\Phi}\right]}{r\partial \theta}\,. \tag{2.10}$$

Equation (2.8) is the mass conservation, and Equations (2.9) and (2.10) are the radial and azimuthal momentum equations. These fluid equations for both stellar and gaseous discs are confined to the two-dimensional disc plane at $z = 0$, while Poisson integral Equation (2.5) is three-dimensional. These equations do not involve an isopedic magnetic field at this stage.

2.3 Scale-free discs and relevant parameter ranges

Scale-free discs are represented by power-law forms with a few disc index parameters. A self-consistent form of disc solution can be written as

$$v_r^{(g)} = e^{(g)}(\varphi)r^{-\beta}\,, \qquad v_r^{(s)} = e^{(s)}(\varphi)r^{-\beta}\,, \tag{2.11}$$

$$v_\theta^{(g)} = b^{(g)}(\varphi)r^{-\beta}\,, \qquad v_\theta^{(s)} = b^{(s)}(\varphi)r^{-\beta}\,, \tag{2.12}$$

$$\Sigma^{(g)} = S^{(g)}(\varphi)r^{-2\beta-1}\,, \qquad \Sigma^{(s)} = S^{(s)}(\varphi)r^{-2\beta-1}\,, \tag{2.13}$$

$$\Pi^{(g)} = k^{(g)}\left[\Sigma^{(g)}\right]^n\,, \qquad \Pi^{(s)} = k^{(s)}\left[\Sigma^{(s)}\right]^n\,, \tag{2.14}$$

$$H^{(g)} = Q^{(g)}(\varphi)r^{-2\beta}\,, \qquad H^{(s)} = Q^{(s)}(\varphi)r^{-2\beta} \tag{2.15}$$

$$\Phi = -P(\varphi)r^{-2\beta}\,, \qquad \overline{\Phi} = -\overline{P}r^{-2\beta}\,, \tag{2.16}$$

where $e^{(i)}$, $b^{(i)}$, $S^{(i)}$, $Q^{(i)}$, and P are functions of only φ which is an argument abbreviation $\varphi \equiv \theta + \mu \ln r$ with μ being a parameter, and $\overline{P}$ for the dark matter halo is a constant coefficient independent of φ. The detailed mathematical procedure of constructing such self-similar scale-free solutions can be found in Lynden-Bell & Lemos (1999). By comparing Equations (2.4) and (2.15), we immediately obtain a relation between the two power-law indices n and β, namely

$$(2\beta + 1)(n - 1) = 2\beta \qquad \rightarrow \qquad n = (1 + 4\beta)/(1 + 2\beta) \; . \tag{2.17}$$

Based on expressions (2.2) and (2.3), we find that for warm discs with $k^{(i)} > 0$, the barotropic index n must also be positive in order to ensure a positive right-hand side (RHS) of Equation (2.3) (i.e. a real sound speed). This physical requirement for warm discs leads to either $\beta > -1/4$ or $\beta < -1/2$. For cold discs with $k^{(i)} \rightarrow 0$, there is no constraint on the barotropic index n. Another empirical constraint which arises from observational results is that $\Sigma^{(i)}$ should decrease with increasing r which requires a β larger than $-1/2$. With the assumption of decreasing $\Sigma^{(i)}$, a singularity of mass would arise in the central region as $r \rightarrow 0^{+}$. This problem can be remedied by requiring a finite integral

$$\lim_{r \to 0} \int_0^r \int_0^{2\pi} \Sigma^{(i)}(r, \theta) r \mathrm{d}r \mathrm{d}\theta = \int_0^{2\pi} S^{(i)}(\theta) \mathrm{d}\theta \lim_{r \to 0} \left[\frac{r^{1-2\beta}}{1 - 2\beta} \right]_0^r < +\infty \tag{2.18}$$

which leads to $\beta < 1/2$. Therefore for warm discs with $k^{(i)} > 0$, the scaling index range is $\beta \in (-1/4,\ 1/2)$ and for cold discs with $k^{(i)} = 0$, we simply require $\beta \in (-1/2,\ 1/2)$.

2.4 An Isopedic magnetic field across a scale-free thin gaseous disc

Effective modifications of the gravitational potential and the pressure in a composite system of two discs due to the very presence of an isopedic magnetic field were derived in reference to the study of singular isothermal discs (SIDs) by Lou & Wu (2005). Following Li & Shu (1996), we define a constant dimensionless ratio λ as

$$\lambda = 2\pi \mathrm{G}^{1/2} \Sigma^{(g)} / B_z \equiv 2\pi \mathrm{G}^{1/2} \Lambda = \text{constant} > 0 \; . \tag{2.19}$$

Parameters λ and Λ indicate how strong the magnetic field is as compared to the surface mass density of the gas disc; they are proportional to B_z^{-1} such that for weak or strong magnetic fields they become very large or small, respectively. Parameter η is a dimensionless ratio of the total

horizontal gravitational acceleration $|\vec{f}_{\parallel}| = |\vec{f}_{\parallel}^{(g)} + \vec{f}_{\parallel}^{(s)}|$ (continuous across the thin disc along the vertical direction) to the total vertical gravitational acceleration just above the two discs with a total surface mass density $\Sigma = \Sigma^{(g)} + \Sigma^{(s)}$, namely

$$\eta \equiv \frac{|\vec{f}_{\parallel}|}{2\pi \mathrm{G}\Sigma} = \frac{|\vec{f}_{\parallel}^{(g)}|}{2\pi \mathrm{G}\Sigma^{(g)}} \,, \tag{2.20}$$

where the gaseous disc contribution to $\vec{f}_{\parallel}$ is $\vec{f}_{\parallel}^{(g)} = -\vec{\nabla}_{\parallel}\Phi^{(g)}$. The two-dimensional gradient operation $\vec{\nabla}_{\parallel}$ within the disc plane coincident with $z = 0$ and in terms of cylindrical coordinates $(r,\ \theta,\ z)$ is

$$\vec{\nabla}_{\parallel} = \frac{\partial}{\partial r}\vec{e}_r + \frac{1}{r}\frac{\partial}{\partial \theta}\vec{e}_{\theta} \,, \tag{2.21}$$

where $\vec{e}_r$ and $\vec{e}_{\theta}$ are unit vectors along the radial and azimuthal directions, respectively. The sum of the magnetic tension force and the horizontal gravity force acting on the isopedically magnetized gaseous disc is

$$\vec{f}^{(g)} = \vec{f}_{\rm ten}^{(g)} + \vec{f}_{\parallel}^{(g)} = \epsilon \vec{f}_{\parallel}^{(g)} \,, \tag{2.22}$$

with $\vec{f}_{\rm ten}^{(g)}$ as the magnetic tension force acting in the magnetized gaseous disc and $\epsilon \equiv 1 - 1/\lambda^2$. In other words, the magnetic tension force $\vec{f}_{\rm ten}^{(g)}$ and the horizontal gravity of gaseous disc $\vec{f}_{\parallel}^{(g)}$ act always in opposite directions. Effectively, Equation (2.22) leads to the modification of the gravitational potential for the gaseous disc as

$$\Phi^{(g)} \rightarrow \epsilon \Phi^{(g)} \,, \tag{2.23}$$

where ϵ is referred to as the *reduction factor* because it is always less than unity and may become negative. The situation of $\epsilon < 0$ happens when the magnetic tension force overwhelms the gas disc horizontal gravity. Due to the additional magnetic pressure, the total pressure in the magnetized gaseous disc is effectively enhanced by

$$\Pi^{(g)} \rightarrow \Theta \Pi^{(g)} \,, \text{with } \Theta = 1 + \frac{1+\eta^2}{\hat{\lambda}^2 + \eta^2} \,,\ \hat{\lambda} = \left(1 + \delta^{-1}\right)\lambda \,,\ \delta = \Sigma^{(g)}/\Sigma^{(s)} \,. \tag{2.24}$$

Here, Θ is referred to as the *enhancement factor* because we always have $\Theta > 1$. For the effective modification of disc enthalpy $H^{(g)}$, we assume for simplicity that Θ is independent of the cylindrical coordinates r and θ and get $H^{(g)} \rightarrow \Theta H^{(g)}$.

In summary, the gravitational potential $\Phi^{(g)}$, the pressure $\Pi^{(g)}$ and the enthalpy $H^{(g)}$ in an isopedically magnetized gaseous disc are effectively modified according to $\Phi^{(g)} \rightarrow \epsilon\Phi^{(g)}$, $\Pi^{(g)} \rightarrow \Theta\Pi^{(g)}$ and $H^{(g)} \rightarrow \Theta H^{(g)}$ while the counterparts of these variables remain unchanged in

the stellar disc. The magnetosonic speed squared in the isopedically magnetized gaseous disc is then

$$\Theta \frac{\mathrm{d}\Pi^{(g)}}{\mathrm{d}\Sigma^{(g)}} = n\Theta k^{(g)} \left[\Sigma^{(g)}\right]^{n-1} = \Theta \left[a^{(g)}\right]^2 \ . \tag{2.25}$$

In reference to Equations $(2.8) - (2.10)$, an isopedic magnetic field in the gaseous disc leads to the following modified set of coupled equations.

$$\frac{\partial \Sigma^{(i)}}{\partial t} + \frac{1}{r}\frac{\partial}{\partial r}\left[r\Sigma^{(i)} v_r^{(i)}\right] + \frac{1}{r}\frac{\partial}{\partial \theta}\left[\Sigma^{(i)} v_\theta^{(i)}\right] = 0 \ , \tag{2.26}$$

$$\frac{\partial v_r^{(s)}}{\partial t} + v_r^{(s)}\frac{\partial v_r^{(s)}}{\partial r} + \frac{v_\theta^{(s)}}{r}\frac{\partial v_r^{(s)}}{\partial \theta} - \frac{\left[v_\theta^{(s)}\right]^2}{r} = -\frac{1}{\Sigma^{(s)}}\frac{\partial \Pi^{(s)}}{\partial r}$$
$$-\frac{\partial\left[\Phi^{(s)} + \Phi^{(g)} + \overline{\Phi}\right]}{\partial r} = -\frac{\partial\left[H^{(s)} + \Phi^{(s)} + \Phi^{(g)} + \overline{\Phi}\right]}{\partial r} \ , \tag{2.27}$$

$$\frac{\partial v_r^{(g)}}{\partial t} + v_r^{(g)}\frac{\partial v_r^{(g)}}{\partial r} + \frac{v_\theta^{(g)}}{r}\frac{\partial v_r^{(g)}}{\partial \theta} - \frac{\left[v_\theta^{(g)}\right]^2}{r} = -\frac{1}{\Sigma^{(g)}}\frac{\partial\left[\Theta\Pi^{(g)}\right]}{\partial r}$$
$$-\frac{\partial\left[\Phi^{(s)} + \epsilon\Phi^{(g)} + \overline{\Phi}\right]}{\partial r} = -\frac{\partial\left[\Theta H^{(g)} + \Phi^{(s)} + \epsilon\Phi^{(g)} + \overline{\Phi}\right]}{\partial r} \ , \tag{2.28}$$

$$\frac{\partial v_\theta^{(s)}}{\partial t} + v_r^{(s)}\frac{\partial v_\theta^{(s)}}{\partial r} + \frac{v_\theta^{(s)}}{r}\frac{\partial v_\theta^{(s)}}{\partial \theta} + \frac{v_\theta^{(s)} v_r^{(s)}}{r} = -\frac{1}{\Sigma^{(s)} r}\frac{\partial \Pi^{(s)}}{\partial \theta}$$
$$-\frac{\partial\left[\Phi^{(s)} + \Phi^{(g)} + \overline{\Phi}\right]}{r\partial \theta} = -\frac{\partial\left[H^{(s)} + \Phi^{(s)} + \Phi^{(g)} + \overline{\Phi}\right]}{r\partial \theta} \ , \tag{2.29}$$

$$\frac{\partial v_\theta^{(g)}}{\partial t} + v_r^{(g)}\frac{\partial v_\theta^{(g)}}{\partial r} + \frac{v_\theta^{(g)}}{r}\frac{\partial v_\theta^{(g)}}{\partial \theta} + \frac{v_\theta^{(g)} v_r^{(g)}}{r} = -\frac{1}{\Sigma^{(g)} r}\frac{\partial\left[\Theta\Pi^{(g)}\right]}{\partial \theta}$$
$$-\frac{\partial\left[\Phi^{(s)} + \epsilon\Phi^{(g)} + \overline{\Phi}\right]}{r\partial \theta} = -\frac{\partial\left[\Theta H^{(g)} + \Phi^{(s)} + \epsilon\Phi^{(g)} + \overline{\Phi}\right]}{r\partial \theta} \ . \tag{2.30}$$

Equations $(2.26) - (2.30)$ bear very similar form of hydrodynamic equations $(2.8) - (2.10)$ with the effect of an isopedic magnetic field being subsumed into two dimensionless parameters Θ and ϵ related to the magnetized gaseous disc component (Shu & Li 1997; Wu & Lou 2006).

2.5 Equilibrium configuration of a composite rotating disc system

In a stationary equilibrium, the stellar and gas discs in a composite disc system rotate with *different* angular speeds in general while satisfying the basic nonlinear fluid-magnetofluid equations. For both discs in coupled rotational equilibrium of axisymmetry, the gravitational acceleration caused by the dark matter halo and the two discs together is the same in the two radial force balance

conditions [i.e. Equations (2.31) and (2.32) below]. Meanwhile, the gas pressure and magnetic Lorentz forces together in the gaseous disc are different from the effective pressure force produced by stellar velocity dispersion in the stellar disc in general. These naturally lead to two different angular speeds of the two discs. Equilibrium variables of a composite rotating disc configuration are denoted by a subscript 0. For a rotating disc configuration in a stationary axisymmetric equilibrium, radial velocities vanish with $v_{r0}^{(g)} = v_{r0}^{(s)} = 0$ and $v_{\theta 0}^{(g)} = \Omega_0^{(g)} r$, $v_{\theta 0}^{(s)} = \Omega_0^{(s)} r$ with $\Omega_0^{(i)} \equiv \Omega_0^{(i)}(r)$ being the differential angular rotation speed of each disc. The mass conservation equations are consistently satisfied by our prescription. Radial momentum Equations (2.27) and (2.28) then lead to two balance conditions

$$\frac{\left[v_{\theta 0}^{(s)}\right]^2}{r} = \frac{\partial\left[H_0^{(s)} + \Phi_0^{(s)} + \Phi_0^{(g)} + \overline{\Phi}_0\right]}{\partial r} \,, \tag{2.31}$$

$$\frac{\left[v_{\theta 0}^{(g)}\right]^2}{r} = \frac{\partial[\Theta H_0^{(g)} + \Phi_0^{(s)} + \epsilon\Phi_0^{(g)} + \overline{\Phi}_0]}{\partial r} \,. \tag{2.32}$$

In general, the radial derivative of disc enthalpy is related to the 'sound speed' as follows

$$\frac{\partial H_0^{(i)}}{\partial r} = \frac{\partial}{\partial r}\left[\frac{nk^{(i)}}{(n-1)}\left[S_0^{(i)}\right]^{n-1} r^{(-2\beta-1)(n-1)}\right] = -\frac{\left[a^{(i)}\right]^2}{r}(2\beta+1) \,. \tag{2.33}$$

For the total surface mass density in a rotational equilibrium configuration, we take

$$\Sigma_0 = \Sigma_0^{(g)} + \Sigma_0^{(s)} = S_0^{(g)} r^{-2\beta-1} + S_0^{(s)} r^{-2\beta-1} = S_0 r^{-2\beta-1} \,, \tag{2.34}$$

where $S_0^{(s)}$ and $S_0^{(g)}$ are two positive constant coefficients (see also Equation (2.13)) and S_0 is the sum of these two coefficients $S_0^{(s)}$ and $S_0^{(g)}$. Prescribed as such, one can make use of formulae in Qian (1992) for the total gravitational potential

$$\Phi_0 = -\mathrm{G} r \Sigma_0 Y_0(\beta) = -\mathrm{G} Y_0(\beta) S_0 r^{-2\beta} \,, \tag{2.35}$$

where the coefficient factor $Y_0(\beta)$ is related to the standard Γ functions by

$$Y_0(\beta) \equiv \frac{\pi\Gamma(1/2-\beta)\Gamma(\beta)}{\Gamma(1-\beta)\Gamma(1/2+\beta)} \,. \tag{2.36}$$

For later global non-axisymmetric perturbation analysis, we also introduce below a generalization of $Y_0(\beta)$ as $Y_m(\beta)$ defined by

$$Y_m(\beta) \equiv \frac{\pi\Gamma(m/2-\beta+1/2)\Gamma(m/2+\beta)}{\Gamma(m/2-\beta+1)\Gamma(m/2+\beta+1/2)} \,, \tag{2.37}$$

where m is an integer in the complex phase factor $\exp(-im\theta)$ for characterizing non-axisymmetric coplanar perturbations. As shown by Qian (1992), the valid range for expression (2.37) is $-m/2 < \beta < (m+1)/2$. For the smallest $m = 1$, the valid range of β is $(-1/2,\ 1)$ which is wider than the derived β range $(-1/4,\ 1/2)$ for warm background discs; and therefore we do not worry about the parameter regime of β in our subsequent global perturbation analysis. This leads to the following relation for the horizontal-to-perpendicular gravity ratio η as defined by Equation (2.20), viz.

$$\eta = \frac{|-\vec{\nabla}_{\parallel}\Phi_0|}{2\pi \mathrm{G}\Sigma_0} = \frac{|-2\mathrm{G}\beta Y_0(\beta) r^{-2\beta-1} S_0 \vec{e}_r|}{2\pi \mathrm{G} S_0 r^{-2\beta-1}} = \frac{\beta Y_0(\beta)}{\pi} \equiv \eta(\beta)\ . \tag{2.38}$$

For each equilibrium configuration in the composite disc system, the gravitational potential and its first radial derivative are given by

$$\Phi_0^{(i)} = -\mathrm{G}r\Sigma_0^{(i)} Y_0(\beta) = -\mathrm{G}Y_0(\beta) r^{-2\beta} S_0^{(i)}\ , \tag{2.39}$$

$$\frac{\partial \Phi_0^{(i)}}{\partial r} = 2\beta \mathrm{G} Y_0(\beta) \Sigma_0^{(i)}\ . \tag{2.40}$$

To measure the effect of a dark matter halo, we introduce a gravitational potential ratio parameter f as

$$f \equiv \frac{\overline{\Phi}_0}{\left[\Phi_0^{(s)} + \Phi_0^{(g)}\right]} = \frac{\overline{\Phi}_0}{\Phi_0} \tag{2.41}$$

for the ratio between the dark matter halo potential to the background potential of the two coupled discs together. The radial derivative of the axisymmetric dark matter halo potential can now be expressed as

$$\frac{\partial \overline{\Phi}_0}{\partial r} = f \frac{\partial \left[\Phi_0^{(s)} + \Phi_0^{(g)}\right]}{\partial r} = f 2\beta \mathrm{G} Y_0(\beta) \Sigma_0\ . \tag{2.42}$$

With the expressions for enthalpies and gravitational potentials derived above, radial force balances (2.31) and (2.32) become

$$\left[v_{\theta 0}^{(s)}\right]^2 + \left[a^{(s)}\right]^2 (2\beta+1) = 2\beta r \mathrm{G} Y_0(\beta) \left[\Sigma_0^{(s)} + \Sigma_0^{(g)}\right](1+f)\ , \tag{2.43}$$

$$\left[v_{\theta 0}^{(g)}\right]^2 + \Theta\left[a^{(g)}\right]^2 (2\beta+1) = 2\beta r \mathrm{G} Y_0(\beta) \left\{\left[\Sigma_0^{(s)} + \Sigma_0^{(g)}\right](1+f) - (1-\epsilon)\Sigma_0^{(g)}\right\}\ . \tag{2.44}$$

The physical properties of the two discs are related by equilibrium conditions (2.43) and (2.44). The two polytropic sound speeds $a^{(s)}$ and $a^{(g)}$ in the axisymmetric background stellar and gaseous

discs are respectively

$$\left[a^{(s)}\right]^2 = nk^{(s)}\left[\Sigma_0^{(s)}\right]^{n-1} = \frac{n\Pi_0^{(s)}}{\Sigma_0^{(s)}} = \frac{(1+4\beta)}{(1+2\beta)}k^{(s)}\left[S_0^{(s)}\right]^{2\beta/(1+2\beta)}r^{-2\beta}\,, \tag{2.45}$$

$$\left[a^{(g)}\right]^2 = nk^{(g)}\left[\Sigma_0^{(g)}\right]^{n-1} = \frac{n\Pi_0^{(g)}}{\Sigma_0^{(g)}} = \frac{(1+4\beta)}{(1+2\beta)}k^{(g)}\left[S_0^{(g)}\right]^{2\beta/(1+2\beta)}r^{-2\beta}\,. \tag{2.46}$$

Combining Equations (2.43) and (2.44), one can readily deduce the equilibrium surface mass densities of two discs as

$$\Sigma_0^{(s)} = \frac{\left[v_{\theta 0}^{(s)}\right]^2 + \left[a^{(s)}\right]^2(2\beta+1)}{2\beta r\mathrm{G}Y_0(\beta)(1+f)(1+\delta_0)}\,, \tag{2.47}$$

$$\Sigma_0^{(g)} = \frac{\left[v_{\theta 0}^{(g)}\right]^2 + \Theta\left[a^{(g)}\right]^2(2\beta+1)}{2\beta r\mathrm{G}Y_0(\beta)(f+1/\delta_0+f/\delta_0+\epsilon)}\,, \tag{2.48}$$

with $\delta_0 \equiv \Sigma_0^{(g)}/\Sigma_0^{(s)}$ being the ratio of gaseous to stellar disc surface mass densities. As the surface mass densities are positive, we obtain a necessary inequality between the potential ratio f and the ratio λ by using the fact that the quantities δ_0, $Y_0(\beta)$ and r are all positive

$$f + 1/\delta_0 + f/\delta_0 + \epsilon > 0 \qquad \text{for} \qquad \beta > 0\,. \tag{2.49}$$

$\epsilon = 1 - 1/\lambda^2$ may be negative for a strong isopedic magnetic field. This is the first requirement on potential ratio f parameter which will be used later. Since $\beta > -1/4$ for all discs, the numerators of Equations (2.47) and (2.48) are always positive which leads to the condition that β in the denominator must be positive since all other factors are positive. This condition restricts our exploration to the range of $\beta = (0,\ 1/2)$.

2.6 Two-dimensional coplanar MHD perturbation equations

For coplanar MHD perturbations in a background rotating axisymmetric disc system with $v_r^{(i)} = v_{r0}^{(i)} + v_{r1}^{(i)}$, $v_\theta^{(i)} = v_{\theta 0}^{(i)} + v_{\theta 1}^{(i)}$, $\Sigma^{(i)} = \Sigma_0^{(i)} + \Sigma_1^{(i)}$, $\Phi^{(i)} = \Phi_0^{(i)} + \Phi_1^{(i)}$ and $H^{(i)} = H_0^{(i)} + H_1^{(i)}$ in Equations $(2.8) - (2.10)$, where superscript i within parentheses can be set as s and g for stellar and magnetized gaseous discs respectively, it is straightforward to obtain linearized perturbation

equations below

$$\frac{\partial \Sigma_1^{(i)}}{\partial t} + \frac{1}{r}\frac{\partial}{\partial r}\left[r\Sigma_0^{(i)} v_{r1}^{(i)}\right] + \frac{1}{r}\frac{\partial}{\partial \theta}\left[\Sigma_0^{(i)} v_{\theta 1}^{(i)} + \Sigma_1^{(i)} v_{\theta 0}^{(i)}\right] = 0 \ , \quad (2.50)$$

$$\frac{\partial v_{r1}^{(s)}}{\partial t} + \Omega_0^{(s)}\frac{\partial v_{r1}^{(s)}}{\partial \theta} - 2\Omega_0^{(s)} v_{\theta 1}^{(s)} = -\frac{\partial\left[H_1^{(s)} + \Phi_1^{(s)} + \Phi_1^{(g)}\right]}{\partial r} \ , \quad (2.51)$$

$$\frac{\partial v_{r1}^{(g)}}{\partial t} + \Omega_0^{(g)}\frac{\partial v_{r1}^{(g)}}{\partial \theta} - 2\Omega_0^{(g)} v_{\theta 1}^{(g)} = -\frac{\partial\left[\Theta H_1^{(g)} + \Phi_1^{(s)} + \epsilon\Phi_1^{(g)}\right]}{\partial r} \ , \quad (2.52)$$

$$\frac{\partial v_{\theta 1}^{(s)}}{\partial t} + v_{r1}^{(s)}\left[\Omega_0^{(s)} + r\frac{\mathrm{d}\Omega_0^{(s)}}{\mathrm{d}r}\right] + \Omega_0^{(s)}\frac{\partial v_{\theta 1}^{(s)}}{\partial \theta} + \Omega_0^{(s)} v_{r1}^{(s)} = -\frac{\partial\left[H_1^{(s)} + \Phi_1^{(s)} + \Phi_1^{(g)}\right]}{r\partial \theta} \ , \quad (2.53)$$

$$\frac{\partial v_{\theta 1}^{(g)}}{\partial t} + v_{r1}^{(g)}\left[\Omega_0^{(g)} + r\frac{\mathrm{d}\Omega_0^{(g)}}{\mathrm{d}r}\right] + \Omega_0^{(g)}\frac{\partial v_{\theta 1}^{(g)}}{\partial \theta} + \Omega_0^{(g)} v_{r1}^{(g)} = -\frac{\partial\left[\Theta H_1^{(g)} + \Phi_1^{(s)} + \epsilon\Phi_1^{(g)}\right]}{r\partial \theta} \ , \quad (2.54)$$

where $v_{r0}^{(i)} = 0$ for the background disc configuration. Equation (2.50) represents the two mass conservation equations, Equations (2.51) and (2.52) are the two radial momentum equations, and Equations (2.53) and (2.54) are the two azimuthal momentum equations; effects of the isopedic magnetic field are subsumed in the two parameters Θ and ϵ (see Equations 2.23 and 2.24) for the magnetized gaseous disc in momentum Equations (2.52) and (2.54); and the gravitational coupling between the stellar and gaseous discs is represented by the sum of gravitational potential perturbations $\Phi_1^{(s)} + \Phi_1^{(g)}$ or $\Phi_1^{(s)} + \epsilon\Phi_1^{(g)}$ in two-dimensional perturbation Equations (2.51) to (2.54). As the axisymmetric gravitational potential of a massive dark matter halo is presumed to be unperturbed for simplicity, its perturbation does not appear on the right-hand sides of Equations (2.51) to (2.54).[2] For perturbations cast in the form of Fourier decomposition, we write for example

$$v_{r1}^{(i)} = A^{(i)}(r)\exp[i(\omega t - m\theta)] \ , \quad v_{\theta 1}^{(i)} = B^{(i)}(r)\exp[i(\omega t - m\theta)] \ , \quad (2.55)$$

where m is an integral number to characterize azimuthal variations, ω is the angular perturbation frequency, $A^{(i)}(r)$ and $B^{(i)}(r)$ are small-magnitude functions of radius r, and superscript $i = s,\ g$ stand for associations with stellar and gaseous discs, respectively. Two new frequency parameters are now introduced below for simplicity. The first one is the abbreviation $\overline{\omega}^{(i)} \equiv \omega - m\Omega_0^{(i)}$ and

[2]The assumption of an unperturbed axisymmetric dark matter halo corresponds to a limiting case. It would be interesting to explore the case where the dark matter halo is perturbed and coupled to disc perturbations gravitationally.

the second one is the so-called epicyclic frequency $\kappa_0^{(i)}$ of a rotating disc defined by

$$\left[\kappa_0^{(i)}\right]^2 = \frac{r\mathrm{d}\left[\Omega_0^{(i)}\right]^2}{\mathrm{d}r} + 4\left[\Omega_0^{(i)}\right]^2 = 2\left[b_0^{(i)}\right]^2(1-\beta)r^{-2\beta-2} = 2(1-\beta)\left[\Omega_0^{(i)}\right]^2 . \quad (2.56)$$

Substituting all expressions of Fourier harmonics into Equations (2.50)−(2.54), we obtain the following perturbation equations

$$\Sigma_1^{(i)} i\overline{\omega}^{(i)} + \frac{1}{r}\frac{\partial}{\partial r}\left[r\Sigma_0^{(i)} v_{r1}^{(i)}\right] - \frac{im}{r}\Sigma_0^{(i)} v_{\theta 1}^{(i)} = 0 , \quad (2.57)$$

$$v_{r1}^{(s)} i\overline{\omega}^{(s)} - 2\Omega_0^{(s)} v_{\theta 1}^{(s)} = -\frac{\partial\left[H_1^{(s)} + \Phi_1^{(s)} + \Phi_1^{(g)}\right]}{\partial r} , \quad (2.58)$$

$$v_{r,1}^{(g)} i\overline{\omega}^{(g)} - 2\Omega_0^{(g)} v_{\theta 1}^{(g)} = -\frac{\partial\left[\Theta H_1^{(g)} + \Phi_1^{(s)} + \epsilon\Phi_1^{(g)}\right]}{\partial r} , \quad (2.59)$$

$$v_{\theta 1}^{(s)} i\overline{\omega}^{(s)} + v_{r1}^{(s)}\frac{\left[\kappa_0^{(s)}\right]^2}{2\Omega_0^{(s)}} = \frac{im\left[H_1^{(s)} + \Phi_1^{(s)} + \Phi_1^{(g)}\right]}{r} , \quad (2.60)$$

$$v_{\theta 1}^{(g)} i\overline{\omega}^{(g)} + v_{r1}^{(g)}\frac{\left[\kappa_0^{(g)}\right]^2}{2\Omega_0^{(g)}} = \frac{im\left[\Theta H_1^{(g)} + \Phi_1^{(s)} + \epsilon\Phi_1^{(g)}\right]}{r} , \quad (2.61)$$

for both stellar and isopedically magnetized gaseous discs coupled by gravity. Furthermore, the perturbation of surface mass density is set to the following form of Fourier harmonics

$$\Sigma_1^{(i)} = S_1^{(i)} r^{-2\beta_1 - 1}\exp[i(\omega t - m\theta + \nu\ln r)] = S_1^{(i)} r^{-2\beta_1^d - 1}\exp[i(\omega t - m\theta)] \quad (2.62)$$

with $S_1^{(i)}$ being small-magnitude coefficients to justify the perturbation approach and

$$\beta_1^d \equiv \beta_1 - i\nu/2 \quad (2.63)$$

being complex in general for $\nu \neq 0$. The unit complex factor $\exp(-im\theta)$ represents periodic azimuthal variations and the unit complex factor $\exp(i\nu\ln r)$ represents radial variations with ν closely related to the radial wavenumber. In general, β_1 parameter for perturbations can be different from β parameter used for characterizing the background axisymmetric equilibrium disc in rotation. According to several formulae derived by Qian (1992), the corresponding perturbation of gravitational potential associated with a surface mass density perturbation is given by

$$\Phi_1^{(i)} = -\mathrm{G}Y_m(\beta_1^d) S_1^{(i)} r^{-2\beta_1^d}\exp[i(\omega t - m\theta)] = -\mathrm{G}rY_m(\beta_1^d)\Sigma_1^{(i)} \quad (2.64)$$

analytically and the corresponding perturbation of enthalpy is given by

$$H_1^{(i)} = \frac{\mathrm{d}H_0^{(i)}}{\mathrm{d}\Sigma_0^{(i)}}\Sigma_1^{(i)} = nk^{(i)}\left[\Sigma_0^{(i)}\right]^{n-2}\Sigma_1^{(i)} = \frac{\left[a^{(i)}\right]^2}{\Sigma_0^{(i)}}\Sigma_1^{(i)} \,. \tag{2.65}$$

It follows immediately that

$$H_1^{(s)} + \Phi_1^{(s)} + \Phi_1^{(g)} = \mathrm{G}r\Sigma_1^{(s)}K^{(s)} \,, \text{ with } K^{(s)} \equiv \frac{\left[a^{(s)}\right]^2}{\mathrm{G}r\Sigma_0^{(s)}} - Y_m(\beta_1^d)(1+\delta_1) \,; \tag{2.66}$$

$$\Theta H_1^{(g)} + \Phi_1^{(s)} + \epsilon\Phi_1^{(g)} = \mathrm{G}r\Sigma_1^{(g)}K^{(g)} \,, \text{ with } K^{(g)} \equiv \frac{\Theta\left[a^{(g)}\right]^2}{\mathrm{G}r\Sigma_0^{(g)}} - Y_m(\beta_1^d)(\epsilon+\delta_1^{-1}) \,, \tag{2.67}$$

where $\delta_1 \equiv \Sigma_1^{(g)}/\Sigma_1^{(s)}$ is a constant ratio for surface mass density perturbations by expression (2.62), and $K^{(s)}$ and $K^{(g)}$ defined by Equations (2.66) and (2.67) respectively are two dimensionless constants because $\left[a^{(i)}\right]^2 \propto r^{-2\beta}$ and $r\Sigma_0^{(i)} \propto r^{-2\beta}$. For coplanar perturbations in the stellar disc in rotation, we then have the following perturbation equations

$$\Sigma_1^{(s)}i\overline{\omega}^{(s)} + \frac{1}{r}\frac{\partial}{\partial r}\left[r\Sigma_0^{(s)}v_{r1}^{(s)}\right] - \frac{im}{r}\Sigma_0^{(s)}v_{\theta 1}^{(s)} = 0 \,, \tag{2.68}$$

$$v_{r1}^{(s)}i\overline{\omega}^{(s)} - 2\Omega_0^{(s)}v_{\theta 1}^{(s)} = -\mathrm{G}K^{(s)}\frac{\partial}{\partial r}\left[\Sigma_1^{(s)}r\right] \,, \tag{2.69}$$

$$v_{\theta 1}^{(s)}i\overline{\omega}^{(s)} + v_{r1}^{(s)}\frac{\left[\kappa_0^{(s)}\right]^2}{2\Omega_0^{(s)}} = im\mathrm{G}\Sigma_1^{(s)}K^{(s)} \,. \tag{2.70}$$

Meanwhile for coplanar MHD perturbations in the isopedically magnetized gaseous disc in rotation, we obtain in parallel

$$\Sigma_1^{(g)}i\overline{\omega}^{(g)} + \frac{1}{r}\frac{\partial}{\partial r}\left[r\Sigma_0^{(g)}v_{r1}^{(g)}\right] - \frac{im}{r}\Sigma_0^{(g)}v_{\theta 1}^{(g)} = 0 \,, \tag{2.71}$$

$$v_{r1}^{(g)}i\overline{\omega}^{(g)} - 2\Omega_0^{(g)}v_{\theta 1}^{(g)} = -\mathrm{G}K^{(g)}\frac{\partial}{\partial r}\left[\Sigma_1^{(g)}r\right] \,, \tag{2.72}$$

$$v_{\theta 1}^{(g)}i\overline{\omega}^{(g)} + v_{r1}^{(g)}\frac{\left[\kappa_0^{(g)}\right]^2}{2\Omega_0^{(g)}} = im\mathrm{G}\Sigma_1^{(g)}K^{(g)} \,. \tag{2.73}$$

From Equations $(2.69)-(2.70)$ and $(2.72)-(2.73)$, we directly derive expressions for radial and azimuthal velocity perturbations $v_{r1}^{(i)}$ and $v_{\theta 1}^{(i)}$ as given below.

$$v_{r1}^{(i)} = \frac{i\mathrm{G}K^{(i)}}{\left[\overline{\omega}^{(i)}\right]^2 - \left[\kappa_0^{(i)}\right]^2}\left(-\frac{2m\Omega_0^{(i)}}{r} + \overline{\omega}^{(i)}\frac{\partial}{\partial r}\right)\left[\Sigma_1^{(i)} r\right] \ , \tag{2.74}$$

$$v_{\theta 1}^{(i)} = \frac{\mathrm{G}K^{(i)}}{\left[\overline{\omega}^{(i)}\right]^2 - \left[\kappa_0^{(i)}\right]^2}\left(\frac{m\overline{\omega}^{(i)}}{r} - \frac{\left[\kappa_0^{(i)}\right]^2}{2\Omega_0^{(i)}}\frac{\partial}{\partial r}\right)\left[\Sigma_1^{(i)} r\right] \ . \tag{2.75}$$

Substituting these expressions into the mass conservation equations and using expression (2.62), we finally arrive at

$$\frac{\overline{\omega}^{(i)} r}{\mathrm{G}K^{(i)}\Sigma_0^{(i)}} \equiv Q^{(i)} = \frac{\left[m^2 - 4(\beta_1^d)^2 + 2\beta_1^d\right]\overline{\omega}^{(i)} - 2m\beta\Omega_0^{(i)}}{\left[\overline{\omega}^{(i)}\right]^2 - \left[\kappa_0^{(i)}\right]^2} - \frac{4(\beta+1)\left[m\Omega_0^{(i)} + \beta_1^d\overline{\omega}^{(i)}\right]\overline{\omega}^{(i)}\omega}{\left[[\overline{\omega}^{(i)}]^2 - [\kappa_0^{(i)}]^2\right]^2} \tag{2.76}$$

for both stellar and magnetized gaseous discs, respectively, and for defining the corresponding $Q^{(i)}$. A combination of these two equations for perturbations in stellar and gaseous discs leads to the dispersion relation of the gravity coupled disc configuration, namely

$$\left\{\left[a^{(s)}\right]^2 - \mathrm{G}\Sigma_0^{(s)} r Y_m(\beta_1^d) - \frac{\overline{\omega}^{(s)} r^2}{Q^{(s)}}\right\} \left\{\Theta\left[a^{(g)}\right]^2 - \epsilon\mathrm{G}\Sigma_0^{(g)} r Y_m(\beta_1^d) - \frac{\overline{\omega}^{(g)} r^2}{Q^{(g)}}\right\} = \mathrm{G}\Sigma_0^{(s)} r Y_m(\beta_1^d)\mathrm{G}\Sigma_0^{(g)} r Y_m(\beta_1^d) \ . \tag{2.77}$$

Dispersion relation (2.77) is of great importance as it contains all useful information about disc dynamics in the presence of coplanar perturbations. Depending on the purpose of investigation, one can define different parameter regimes by using this dispersion relation. The regime of small ω corresponds to the quasi-stationary situations for the QSSS hypothesis (e.g. Bertin & Lin 1996 and extensive references therein). To be specific and for simplicity, we set $\omega = 0$ in our frame of reference to study the case of non-axisymmetric stationary perturbations with $m \neq 0$ and $\omega = 0$ which can be either aligned or unaligned logarithmic spirals. For the stationary case of $\omega = 0$,

Equation (2.77) reduces to

$$\left\{\left[a^{(s)}\right]^2 - \mathrm{G}\Sigma_0^{(s)} r Y_m(\beta_1^d) - \left[\Omega_0^{(s)}\right]^2 r^2 \left[\frac{m^2 - 2(1-\beta)}{m^2 - 4(\beta_1^d)^2 + 2\beta_1^d + 2\beta}\right]\right\}$$
$$\times \left\{\Theta\left[a^{(g)}\right]^2 - \epsilon\mathrm{G}\Sigma_0^{(g)} r Y_m(\beta_1^d) - \left[\Omega_0^{(g)}\right]^2 r^2 \left[\frac{m^2 - 2(1-\beta)}{m^2 - 4(\beta_1^d)^2 + 2\beta_1^d + 2\beta}\right]\right\}$$
$$= \left[\mathrm{G}\Sigma_0^{(s)} r Y_m(\beta_1^d)\right]\left[\mathrm{G}\Sigma_0^{(g)} r Y_m(\beta_1^d)\right] \tag{2.78}$$

where, according to expressions (2.43) and (2.44) for the background equilibrium disc system, we have disc angular rotation speeds given by

$$\Omega_0^{(s)} \equiv v_{\theta 0}^{(s)}/r\,, \quad \Omega_0^{(g)} \equiv v_{\theta 0}^{(g)}/r\,, \tag{2.79}$$

$$\left[v_{\theta 0}^{(s)}\right]^2 = 2\beta r \mathrm{G} Y_0(\beta)\left[\Sigma_0^{(s)} + \Sigma_0^{(g)}\right](1+f) - \left[a^{(s)}\right]^2(2\beta+1)\,, \tag{2.80}$$

$$\left[v_{\theta 0}^{(g)}\right]^2 = 2\beta r \mathrm{G} Y_0(\beta)\left[\left[\Sigma_0^{(s)} + \Sigma_0^{(g)}\right](1+f) - (1-\epsilon)\Sigma_0^{(g)}\right] - \Theta\left[a^{(g)}\right]^2(2\beta+1)\,. \tag{2.81}$$

As the gravitational potential ratio f should be the same in both Equations (2.43) and (2.44), a relation between $\left[v_{\theta 0}^{(s)}\right]^2$ and $\left[v_{\theta 0}^{(g)}\right]^2$ can therefore be established, namely

$$\left[v_{\theta 0}^{(s)}\right]^2 = \left[v_{\theta 0}^{(g)}\right]^2 + (2\beta+1)\left\{\Theta\left[a^{(g)}\right]^2 - \left[a^{(s)}\right]^2\right\} + 2\beta r \mathrm{G} Y_0(\beta)(1-\epsilon)\Sigma_0^{(g)}\,. \tag{2.82}$$

Using expressions $v_{\theta 0}^{(i)} = b_0^{(i)} r^{-\beta}$ and $\Sigma_0^{(i)} = S_0^{(i)} r^{-2\beta-1}$ for the background scale-free disc system, Equation (2.82) can be written as

$$\left[b_0^{(s)}\right]^2 = \left[b_0^{(g)}\right]^2 + (2\beta+1)\left\{\Theta\left[a^{(g)}\right]^2 - \left[a^{(s)}\right]^2\right\} r^{2\beta} + 2\beta \mathrm{G} Y_0(\beta)(1-\epsilon) S_0^{(g)} \tag{2.83}$$

without radial dependence. We now introduce the rotational Mach number $D^{(s)}$ for the stellar disc and the rotational magnetosonic Mach number $D^{(g)}$ for the isopedically magnetized gaseous disc, respectively.

$$D^{(s)} \equiv \frac{v_{\theta 0}^{(s)}}{a^{(s)}} = \frac{b_0^{(s)}}{a^{(s)} r^\beta}\,, \quad \rightarrow \quad b_0^{(s)} = a^{(s)} r^\beta D^{(s)}\,; \tag{2.84}$$

$$D^{(g)} \equiv \frac{v_{\theta 0}^{(g)}}{\sqrt{\Theta} a^{(g)}} = \frac{b_0^{(g)}}{\sqrt{\Theta} a^{(g)} r^\beta}\,, \quad \rightarrow \quad b_0^{(g)} = \sqrt{\Theta} a^{(g)} r^\beta D^{(g)}\,. \tag{2.85}$$

Using background disc equilibrium Equations (2.43), (2.44) and (2.83), the following relations can then be derived,

$$\left[D^{(s)}\right]^2 = \frac{2\beta \mathrm{G} Y_0(\beta) S_0^{(s)}(1+\delta_0)(1+f)}{\left[a^{(s)}\right]^2 r^{2\beta}} - (2\beta+1)\,, \tag{2.86}$$

$$\left[D^{(g)}\right]^2 = \frac{2\beta \mathrm{G} Y_0(\beta) S_0^{(g)}\left[f(1+\delta_0^{-1})+\delta_0^{-1}+\epsilon\right]}{\Theta\left[a^{(g)}\right]^2 r^{2\beta}} - (2\beta+1)\,, \tag{2.87}$$

$$\left[D^{(s)}\right]^2 = \left[D^{(g)}\right]^2 \Delta + (2\beta+1)(\Delta-1) + \frac{2\beta \mathrm{G} Y_0(\beta)(1-\epsilon) S_0^{(g)}}{\left[[a^{(s)}]^2 r^{2\beta}\right]}\,, \tag{2.88}$$

with ratio $\Delta \equiv \Theta\left[a^{(g)}\right]^2 / \left[a^{(s)}\right]^2$. With these defined quantities and relations (2.86), (2.87) and (2.88), stationary dispersion relation (2.78) can be cast into

$$\begin{aligned}
&\left\{1 - \frac{\mathrm{G} S_0^{(s)} Y_m(\beta_1^d)}{\left[a^{(s)}\right]^2 r^{2\beta}} - \left[D^{(s)}\right]^2 \left[\frac{m^2 - 2(1-\beta)}{m^2 - 4(\beta_1^d)^2 + 2\beta_1^d + 2\beta}\right]\right\} \\
&\times \left\{1 - \frac{\epsilon \mathrm{G} S_0^{(g)} Y_m(\beta_1^d)}{\Theta\left[a^{(g)}\right]^2 r^{2\beta}} - \left[D^{(g)}\right]^2 \left[\frac{m^2 - 2(1-\beta)}{m^2 - 4(\beta_1^d)^2 + 2\beta_1^d + 2\beta}\right]\right\} \\
&= \left\{\frac{\mathrm{G} S_0^{(s)} Y_m(\beta_1^d)}{\left[a^{(s)}\right]^2 r^{2\beta}}\right\}\left\{\frac{\mathrm{G} S_0^{(g)} Y_m(\beta_1^d)}{\Theta\left[a^{(g)}\right]^2 r^{2\beta}}\right\}\,.
\end{aligned} \tag{2.89}$$

By using Equations (2.45), (2.46), (2.86) and (2.87), stationary dispersion relation (2.89) can be written as

$$\begin{aligned}
&\left\{1 - \frac{(1+2\beta)\mathrm{G}(S_0^{(g)})^{1/(1+2\beta)} Y_m(\beta_1^d)}{(1+4\beta) k^{(s)} \delta_0^{1/(1+2\beta)}} - \right. \\
&\left[\frac{\mathrm{G}(S_0^{(g)})^{1/(1+2\beta)} 2\beta Y_0(\beta)(1+\delta_0)(1+f)}{(1+4\beta) k^{(s)} \delta_0^{1/(1+2\beta)}} - 1\right] \left.\frac{(2\beta+1)\left[m^2 - 2(1-\beta)\right]}{m^2 - 4(\beta_1^d)^2 + 2\beta_1^d + 2\beta}\right\} \\
&\times \left\{1 - \frac{(1+2\beta)\epsilon\mathrm{G}(S_0^{(g)})^{1/(1+2\beta)} Y_m(\beta_1^d)}{(1+4\beta)\Theta k^{(g)}} - \right. \\
&\left[\frac{2\beta\mathrm{G}(S_0^{(g)})^{1/(1+2\beta)} Y_0(\beta)(f(1+\delta_0^{-1})+\delta_0^{-1}+\epsilon)}{(1+4\beta)\Theta k^{(g)}} - 1\right] \left.\frac{(2\beta+1)\left[m^2 - 2(1-\beta)\right]}{m^2 - 4(\beta_1^d)^2 + 2\beta_1^d + 2\beta}\right\} = \\
&\frac{(1+2\beta)\mathrm{G}(S_0^{(g)})^{1/(1+2\beta)} Y_m(\beta_1^d)}{(1+4\beta) k^{(s)} \delta_0^{1/(1+2\beta)}} \frac{(1+2\beta)\mathrm{G}(S_0^{(g)})^{1/(1+2\beta)} Y_m(\beta_1^d)}{(1+4\beta)\Theta k^{(g)}}\,.
\end{aligned} \tag{2.90}$$

Dimensionless parameters β, m and β_1^d can be chosen within the allowed ranges. Dimensionless parameters ϵ and Θ depend on the isopedic magnetic field characterized by the dimensionless isopedic parameter λ. For parameters $S_0^{(g)}$, $k^{(s)}$, $k^{(g)}$ and δ_0, typical values of late-type spiral galaxies are adopted and described in detail in Section 2.7 below.

2.6.1 Relation between dark matter halo and magnetic field

The goal of our investigation is to explore the functional relation $f(\lambda)$ between the amount of dark matter and the isopedic magnetic field with other parameters specified. For this purpose, we further introduce several simplifying abbreviations for the derivation of $f(\lambda)$ relation, viz.

$$M \equiv \frac{m^2 - 2(1-\beta)}{m^2 - 4(\beta_1^d)^2 + 2\beta_1^d + 2\beta} \, , \; B^{(s)} \equiv \frac{\mathrm{G}S_0^{(s)}}{\left[a^{(s)}\right]^2 r^{2\beta}} \, , \; B^{(g)} \equiv \frac{\mathrm{G}S_0^{(g)}}{\Theta\left[a^{(g)}\right]^2 r^{2\beta}} \, , \tag{2.91}$$

which are all dimensionless. The simplified form of stationary dispersion relation (2.89) then appears as

$$\begin{aligned} \left\{1 - B^{(s)} Y_m(\beta_1^d) - \left[D^{(s)}\right]^2 M\right\} \left\{1 - \epsilon B^{(g)} Y_m(\beta_1^d) - \left[D^{(g)}\right]^2 M\right\} \\ = \left[B^{(s)} Y_m(\beta_1^d)\right] \left[B^{(g)} Y_m(\beta_1^d)\right] \, , \end{aligned} \tag{2.92}$$

where the two disc rotational Mach numbers squared are defined by

$$\left[D^{(s)}\right]^2 = 2\beta B^{(s)} Y_0(\beta)(1+\delta_0)(1+f) - 2\beta - 1 \, , \tag{2.93}$$

$$\left[D^{(g)}\right]^2 = 2\beta B^{(g)} Y_0(\beta)\left[f(1+\delta_0^{-1}) + \delta_0^{-1} + \epsilon\right] - 2\beta - 1 \, . \tag{2.94}$$

The two parameters M and $Y_m(\beta_1^d)$ are complex in general as parameter $\beta_1^d \equiv \beta_1 - i\nu/2$ is complex in general. But for two separate special cases $\beta_1^d = \beta_1$ (i.e. $\nu = 0$) and $\beta_1 = 1/4$ with $\nu \neq 0$, we have shown in Appendix A that both M and $Y_m(\beta_1^d)$ become real numbers. In literature, the situation of $\nu = 0$ is called the aligned case because perturbation patterns appear aligned along the radial direction; that is, only azimuthal variations but no radial variations are involved, and the situation of $\nu \neq 0$ is called unaligned case because perturbation patterns appear spiral-like.

From now on, we shall only focus on these two special real cases $\nu = 0$ with $\beta_1^d = \beta_1 = \beta$ and $\nu \neq 0$ with $\beta_1 = 1/4$. Unless otherwise stated, we have either $\beta_1^d = \beta$ or $\beta_1^d = 1/4 - i\nu/2$ in all the following equations. With our notations, stationary dispersion relation (2.92) for

non-axisymmetric stationary perturbations can be cast into the following form of

$$\begin{aligned}&[1-B^{(s)}Y_m(\beta_1^d)+(2\beta+1)M-2\beta B^{(s)}Y_0(\beta)(1+\delta_0)(1+f)M]\\ \times\big\{&-2\beta B^{(g)}Y_0(\beta)[f(1+\delta_0^{-1})+\delta_0^{-1}+\epsilon]M+1-\epsilon B^{(g)}Y_m(\beta_1^d)+(2\beta+1)M\big\}\\ &=B^{(s)}B^{(g)}\big[Y_m(\beta_1^d)\big]^2\,. \end{aligned}\tag{2.95}$$

In the absence of the gravitational coupling on the right-hand side (RHS) of Equation (2.95), the first and second factors on the left-hand side (LHS) represent stationary dispersion relations in stellar and magnetized gaseous discs separately. That is, for a single stellar disc, we can determine a f value for stationary perturbations. Or, for a single magnetized gaseous disc, we can also determine a f value for stationary MHD perturbations. When the two discs are coupled by gravity, we need to determine the f parameter in a joint manner by dispersion relation (2.95) for stationary perturbation patterns in both discs with different angular rotation speeds. Again, two notational abbreviations are introduced below for the convenience of further derivations, viz.

$$C_1\equiv 1-2\beta B^{(s)}Y_0(\beta)(1+\delta_0)M-B^{(s)}Y_m(\beta_1^d)+(2\beta+1)M\,,\tag{2.96}$$

$$C_2\equiv 1-2\beta B^{(g)}Y_0(\beta)(\epsilon+\delta_0^{-1})M-\epsilon B^{(g)}Y_m(\beta_1^d)+(2\beta+1)M\,.\tag{2.97}$$

Then stationary dispersion relation (2.95) for coplanar perturbations can be rearranged into the form of

$$\begin{aligned}&\big[C_1-2\beta B^{(s)}Y_0(\beta)(1+\delta_0)Mf\big]\\ \big[C_2-2\beta B^{(g)}Y_0(\beta)f(1+\delta_0^{-1})M\big]&-B^{(s)}B^{(g)}\big[Y_m(\beta_1^d)\big]^2=0\,.\end{aligned}\tag{2.98}$$

This leads to an explicit quadratic equation in terms of the gravitational potential ratio f given below

$$\begin{aligned}&f^2-f\frac{C_1B^{(g)}(1+\delta_0^{-1})+C_2B^{(s)}(1+\delta_0)}{2\beta B^{(s)}B^{(g)}Y_0(\beta)M(1+\delta_0)(1+\delta_0^{-1})}\\ &+\frac{C_1C_2-B^{(s)}B^{(g)}\big[Y_m(\beta_1^d)\big]^2}{4\beta^2B^{(s)}B^{(g)}[Y_0(\beta)]^2M^2(1+\delta_0)(1+\delta_0^{-1})}=0\,.\end{aligned}\tag{2.99}$$

By further introducing two notational abbreviations

$$V^{(g)}\equiv B^{(g)}(1+\delta_0^{-1})\,,\quad V^{(s)}\equiv B^{(s)}(1+\delta_0)\,,\tag{2.100}$$

the two roots f_1 and f_2 for the gravitational potential ratio f are

$$f_{1,2} = \frac{C_1 V^{(g)} + C_2 V^{(s)} \pm \sqrt{\left[C_1 V^{(g)} - C_2 V^{(s)}\right]^2 + 4\left[Y_m(\beta_1^d)\right]^2 V^{(s)} V^{(g)} B^{(s)} B^{(g)}}}{4\beta V^{(s)} V^{(g)} Y_0(\beta) M} \,, \quad (2.101)$$

where the two roots $f_1 \equiv f_+$ and $f_2 \equiv f_-$ correspond to the plus and minus signs, respectively. All variables are real numbers in our model study here for either $\beta_1^d = \beta$ or $\beta_1^d = 1/4 - i\nu/2$, and there always exist two roots for f which can be either both real or a pair of complex conjugates. By our definition of $f = \overline{\Phi}/\Phi$, we should identify the real positive solution(s) for f. This leads to the requirement that the determinant under the square root in expression (2.101) must be positive which turns out to be automatically satisfied. Another requirement is that in Equations (2.80) and (2.81), both v_{r0}^2 and $v_{\theta 0}^2$ should be non-negative which leads to the following conditions,

$$f \geq \frac{(1+4\beta) k^{(s)} \left[S_0^{(s)}\right]^{2\beta/(1+2\beta)}}{2\beta G Y_0(\beta) S_0} - 1 \,, \quad (2.102)$$

$$f \geq \frac{\Theta(1+4\beta) k^{(g)} \left[S_0^{(g)}\right]^{2\beta/(1+2\beta)}}{2\beta G Y_0(\beta) S_0} + \frac{(1-\epsilon) S_0^{(g)}}{S_0} - 1 \,. \quad (2.103)$$

Together with inequality (2.49), there are thus a total of four necessary conditions on gravitational potential ratio f, viz.

- a) $f \in \Re_+$,
- b) $\Sigma_0^{(g)}(f) > 0$,
- c) $\left[v_{\theta 0}^{(s)}\right]^2(f) > 0$,
- d) $\left[v_{\theta 0}^{(g)}\right]^2(f) > 0$,

in our model analysis for global stationary perturbation patterns.

2.7 Parameters for magnetized spiral galaxies

In dispersion relation (2.90), dimensionless parameters m, β, β_1^d, ϵ and Θ should be specified to characterize stationary perturbations in composite disc system. Physically, integer m indicates the number of spiral arms for a perturbation pattern, β is the power-law exponent to characterize radial variations of the different unperturbed background variables, β_1^d is the exponent to characterize radial variations of perturbations. Parameters ϵ and Θ are the reduction and enhancement factors associated with an isopedic magnetic field, respectively. For relevant coefficient $S_0^{(g)}$, we adopt

parameter ranges listed in Table 2.1 in reference to estimates from observations (e.g. Roberts 1962). In Table 2.1, numerical ranges for $S_0^{(g)}$ and $S_0^{(s)}$ are calculated for $\beta = [0,\ 0.5]$; the ranges for λ and ϵ are determined with the given ranges of Σ_0^g and B_z tabulated below. Two parameters

Variables	Values
Σ_0^g	$2 \times 10^{-4} - 2 \times 10^{-3}$ g cm^{-2}
$\Sigma_0^{(g)}(5\,\mathrm{kpc})$	10^{-3} g cm^{-2}
$S_0^{(g)} = \Sigma_0^{(g)} r^{2\beta+1}$	$(10^{19},\ 10^{41})$ g cm$^{2\beta-1}$
$\delta_0 = \Sigma_0^{(g)}/\Sigma_0^{(s)}$	0.05
$a^{(g)}(5\,\mathrm{kpc})$	1×10^5 cm s^{-1}
$a^{(s)}(5\,\mathrm{kpc})$	3×10^6 cm s^{-1}
B_z	$(1,\ 10)\ \mu$G
B_z in central regions	$(20,\ 40)\ \mu$G
λ	$(0.03,\ 3.25)$
ϵ	$(-1110,\ 1)$

Table 2.1: Typical parameters of late-type disc galaxies

$k^{(s)}$ and $k^{(g)}$ are functions of parameter β and closely relate to the sound speeds (as given in Table 2.1) according to Equations (2.45) and (2.46) with cgs unit of $\mathrm{cm}^{2\mathrm{n}}/(\mathrm{s}^2\ \mathrm{g}^{\mathrm{n}-1})$. Typical values for $k^{(s)}$ and $k^{(g)}$ are of the order of $10^{10}\ \mathrm{cm}^{2\mathrm{n}}/(\mathrm{s}^2\ \mathrm{g}^{\mathrm{n}-1})$. The range for Θ is a function of β and δ_0 and cannot be given here simply but can be computed in a straightforward manner. For the Gamma functions $\Gamma(z)$ involved in our computations, we use the code developed by Zhang & Jin (1996). Our study explores behaviours of potential ratio f dependence on isopedic parameter λ for globally aligned and unaligned logarithmic stationary perturbation patterns. Physically, this study reveals possible relationships of an isopedic magnetic field and the gravitational potential of an axisymmetric dark matter halo for stationary global perturbations. Since $Y_m(\beta_1^d) = Y_{-m}(\beta_1^d)$ (see footnote[3]) and $M(m^2) = M((-m)^2)$, we focus on the case of $m > 0$ without loss of generality. Only the cases for $m = 1$ and $m = 2$ are presented in the following since a previous analysis of Lou & Wu (2005) has shown that all curves for $m \geq 2$ bear similar form, whereas the case of $m = 1$ carries a unique form.

[3]A mathematical proof of this relation can be found in Appendix A of Wu & Lou (2006).

2.8 Global stationary aligned perturbations with $\nu = 0$ and $\beta_1 = \beta$

For global stationary aligned cases with $\nu = 0$, we have further taken a special case of $\beta_1^d = \beta_1 = \beta$ for perturbations carrying the same scale-free index as that of the background equilibrium disc configuration. Relations $f(\lambda)$ for different combinations of β and δ_0 are shown in Figures 2.1 and 2.2 as examples. First, it is noticeable that no sensible f_2 root can be found in

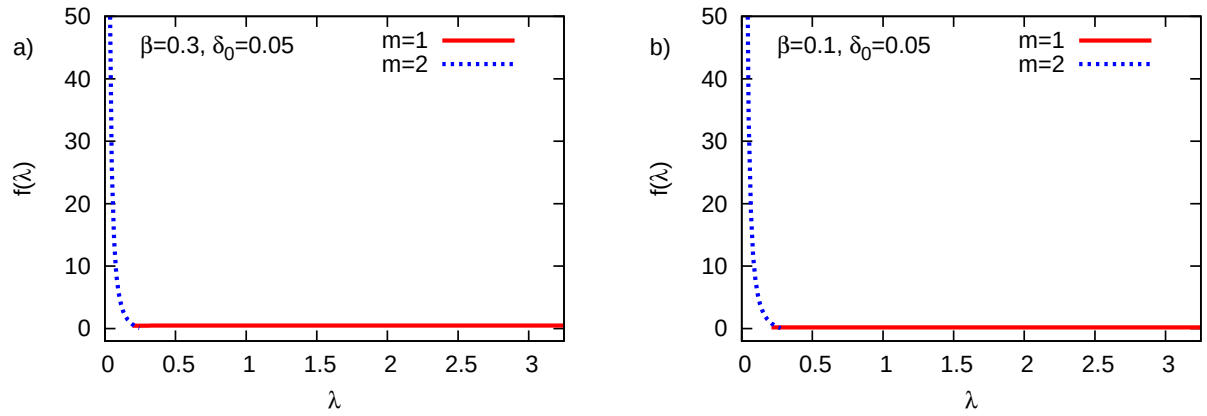

Figure 2.1: The dependence of the gravitational potential ratio f on the dimensionless ratio $\lambda = 2\pi G^{1/2}\Sigma_0^{(g)}/B_z$ and m in the stationary aligned case for late-type disc galaxies with $\delta_0 = 0.05$. Different β values are studied for the aligned case of $\nu = 0$ and $\beta_1 = \beta$. For this and all the following figures, values of all other parameters, which are not explicitly mentioned, are listed in Table 2.1 of Section 2.7. For $\beta = 0.1$ and $m = 1$ (b), $f \rightarrow\sim 0.2$, while for $\beta = 0.3$ and $m = 1$ (a), $f \rightarrow\sim 0.5$.

Figure 2.1 satisfying requirements c) and d) listed after inequalities (2.102) and (2.103). In the following, we only show stationary perturbation solutions with f satisfying all four requirements a)−d) above.

We have explored β values within the range $\beta = [0.01, 0.49]$. Figure 2.1 shows examples for two different β values. The numerical results of positive β values that we have studied do not show remarkable differences among all m values. While $m \geq 2$ give monotonically decreasing functions $f(\lambda)$ for all $\beta > 0$, $m = 1$ case leads to an almost constant $f(\lambda)$ whose value decreases with decreasing β. This latter trend of decrease cannot be easily discerned in the figures shown, but can be readily found by checking the specific numbers. For $\beta = 0.1$ and $m = 1$ (b), $f \rightarrow\sim 0.2$, while for $\beta = 0.3$ and $m = 1$ (a), $f \rightarrow\sim 0.5$.

For $m \geq 2$, stationary solutions for aligned perturbations can be found in all figures for

small λ corresponding to stronger magnetic fields. For $m = 1$, stationary solutions for aligned perturbations exist in a wide range of λ values. In general, $f = 10$ is a typical value for spiral galaxies containing dark matter halos. In Figure 2.1 of a late-type galaxy, $f = 10$ leads to $\lambda \cong 0.1$. For a gaseous surface mass density of $\Sigma_0^{(g)} = 2 \times 10^{-4}$ g cm^{-2}, one gets $B_z = 4\ \mu$G which is a realistic number and for $\Sigma_0^{(g)} = 2 \times 10^{-3}$ g cm^{-2}, the magnetic field strength is $B_z = 40\,\mu$G which may be reached in the central regions of spiral galaxies. It is then realistic to have stationary aligned $m = 1$ perturbations corresponding to lopsided patterns.

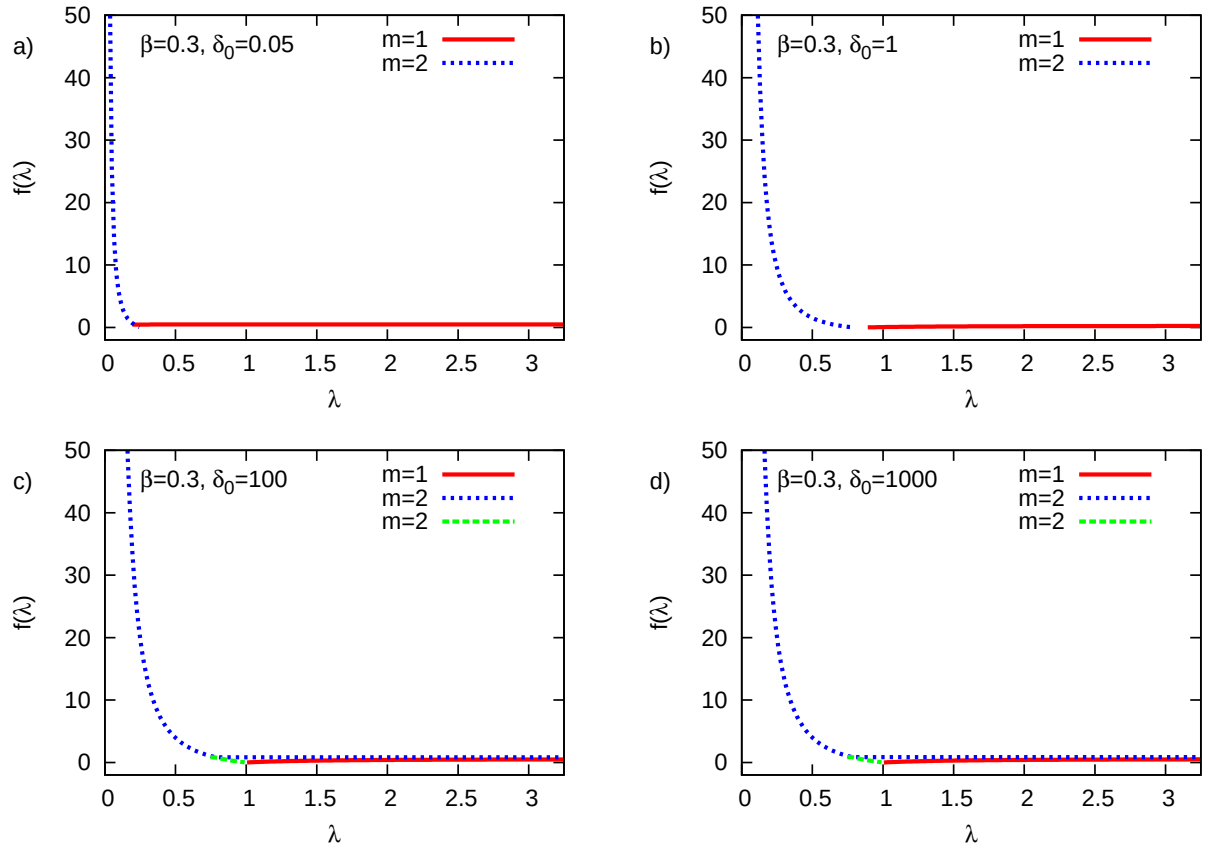

Figure 2.2: The aligned case with $\nu = 0$ and $\beta_1 = \beta$ is studied. The dependence of the dark matter amount f on the dimensionless ratio λ and m in the stationary case for a spiral galaxy with $\beta = 0.3$ and different δ_0 corresponding to different epochs of a spiral galaxy evolution.

An increase of δ_0 in Figure 2.2 should be understood as going back to earlier evolution phases of a spiral galaxy. This is because at early times, the gaseous disc contains more mass and during the course of evolution, the stellar disc becomes more and more massive as a result of star formation. When δ_0 is increased, the stationary range for $m \geq 2$ is also increased to larger λ values whereas that of $m = 1$ is decreased. For larger values of δ_0, $m \geq 2$ gives stationary

solutions in the entire range of λ. In addition, a second solution of $m = 2$ can be also found in the range $\lambda \in (0.7 \sim 1)$ for the two larger δ_0 values. In the limit of $\delta_0 \to \infty$, the stellar disc contains a negligible amount of mass as compared to that of the magnetized gaseous disc. Effectively, this situation can be understood as the presence of only one single isopedically magnetized gaseous disc which was investigated earlier by Wu & Lou (2006). For $\delta_0 > 0.05$, we study again the case of $f = 10$. Here, λ can be much larger than only 0.1 for late-type spiral galaxies. For $\delta_0 = 1000$, one gets $\lambda = 0.4$. In this case, magnetic fields are $B_z = 1\mu\mathrm{G}$ for $\Sigma_0^{(g)} = 2 \times 10^{-4}\mathrm{g\ cm^{-2}}$ which is also realistic and $B_z = 10\mu\mathrm{G}$ for $\Sigma_0^{(g)} = 2 \times 10^{-3}\mathrm{g\ cm^{-2}}$.

The case of $m = 1$ represents an exceptional case in our exploration so far. Observational evidence for the existence of such so-called lopsided galaxies can be found in Baldwin, Lynden-Bell & Sancisi (1980). For a late-type spiral galaxy with $\delta_0 \sim 0.05$ and a positive β value, the stationary solutions in Figure 2.1 can be roughly divided into two ranges of λ. On the left side with small λ or strong magnetic field strengths, stationary solutions for $m \geq 2$ are found. In almost the entire range of $0.2 \leq \lambda \leq 3.25$, the $m = 1$ case has stationary solutions. In general, in the range of weak magnetic fields only $m = 1$ has stationary solutions. For strong magnetic fields, only $m \geq 2$ can possess stationary solutions. The limit of $\lambda \to \infty$ can be regarded as the absence of magnetic fields which was analysed by Shen & Lou (2004).

For larger δ_0 corresponding to an earlier phase of an evolving spiral galaxy as shown in Figure 2.2, the stationary range of λ for $m = 1$ shrinks whereas that of $m \geq 2$ increases to all possible physical values of λ; within a certain range of λ, a second solution for $m \geq 2$ also comes into existence.

Independent of parameter variations, $f(\lambda)$ remains always almost constant for large λ or weak magnetic field strengths. This is sensible as weak magnetic fields are not expected to affect the entire perturbation configuration significantly (e.g. Wentzel 1963). For strong magnetic fields, we need to have a larger amount of dark matter to maintain stationary perturbation configurations. In the aligned case, this increase of f can reach values of several tens, e.g. in the limit of $\lambda = 0.03$, we have $f \sim 45,\ 55$ and 75 for $\beta = 0.49,\ 0.3$ and 0.1, respectively. The exploration of different δ_0 values has revealed additional information: in disc evolution in the early universe, magnetic field should have played a more important role in a spiral galaxy. This is because the range of λ with a significant change of f appears larger; thus weaker magnetic fields should have also affected f values. Note that the magnetic field cannot cause a growth of dark matter halo in a spiral galaxy. Nevertheless, this analysis reveals the relation between the dark matter (f ratio) and the isopedic magnetic field strength (λ parameter). As expected for weak magnetic fields, one may ignore B_z in general. While for strong magnetic fields, there is only one possible f for each λ in order to maintain globally stationary perturbation configurations. Physically, a larger f ratio also leads to a larger disc rotation speed $v_{\theta 0}^{(i)}$ according to Equations (2.80) and (2.81). For

example, one estimates $v_{\theta 0}^{(s)} \cong 270\ \mathrm{km\ s^{-1}}$ for $f = 20$, $r = 10\ \mathrm{kpc}$, $\beta = 0.1$, $a^{(s)} = 30\ \mathrm{km\ s^{-1}}$, $\Sigma_0^{(g)} = 10^{-4}\ \mathrm{g\ cm^{-2}}$ and $\delta_0 = 0.05$ for a late-type spiral galaxy; while for $f = 30$ with all other parameters unchanged, one obtains $v_{\theta 0}^{(s)} \cong 330\ \mathrm{km\ s^{-1}}$. Although very large disc rotational velocities have not been observed, large f can be regarded as theoretically plausible solutions for spiral galaxies.

2.9 Stationary unaligned logarithmic spiral configurations with $\nu \neq 0$ and $\beta_1 = 1/4$

When MHD density wave perturbations propagate in both radial and azimuthal directions, we have global unaligned logarithmic spiral patterns with $\nu \neq 0$ and $m \neq 0$. In our consideration here, we take $\beta_1^d = \beta_1 - i\nu/2 \neq \beta$ for $\nu \neq 0$. In this case, M and $Y_0(\beta_1^d)$ as defined by Equations (2.91) and (2.36) are complex in general, while dimensionless parameters $B^{(s)}$ and $B^{(g)}$ as defined by Equations (2.91) are always real. In the special case of $\beta_1 = 1/4$, we have shown that both M and $Y_0(\beta_1^d)$ are real (see Appendix A). Physically, this case of $\beta_1 = 1/4$ corresponds to a constant radial flux of angular momentum (e.g. Goldreich & Tremaine 1979). Again, the stationary condition for logarithmic spiral patterns implies a certain relation between f ratio (related to the dark matter halo) and λ parameter (related to the isopedic magnetic field). For $\nu \neq 0$, a special attention is further paid to $\nu-$dependence of $f(\lambda)$. For different ν values (related to the radial wave number) in a warm disc, the curves $f(\lambda)$ are shown in Figure 2.3. For small ν, at least one stationary solution exists for each $m > 0$. However for increasing ν towards the tight-winding regime, stationary perturbation solutions of $m = 1$ are shifted towards weaker magnetic fields. For $\nu = 50$, solutions for $m = 1$ are found within the range $\lambda \approx (1.1, 3.25)$ and for $\nu = 100$, they are within $\lambda \approx (1.2, 3.25)$. Meanwhile, stationary perturbation solutions for $m \geq 2$ grow into a larger range of λ. If ν is increased further (i.e. towards the extremely tight-winding regime), two stationary perturbation solutions exist corresponding to each m. Thus according to expression (2.101) for the two roots of f, f_1 and f_2 are the upper and lower curves in Figure 2.3, respectively. In the lower two panels, the two branches of f_1 and f_2 with $f_1 > f_2$ are shown for each $m = 2$. As shown in Appendix B, solutions for $m \geq 2$ are similar. Therefore, solutions for $m = 2$ can be generalized to solutions for $m \geq 2$. For small λ, f_1 and f_2 branches do not cross each other, although they appear to be extremely close. In the range of λ for stationary perturbation solutions, f_1 remains more or less constant so that a change of magnetic field strength appears independent of the amount of dark matter. Meanwhile, f_2 changes over a larger range of λ, indicating that the magnetic field and f_2 relate each other more closely. The magnetic field is directly connected to λ. If f_1 remains constant for all λ, then the reverse direction of reasoning cannot be used, i.e., for a

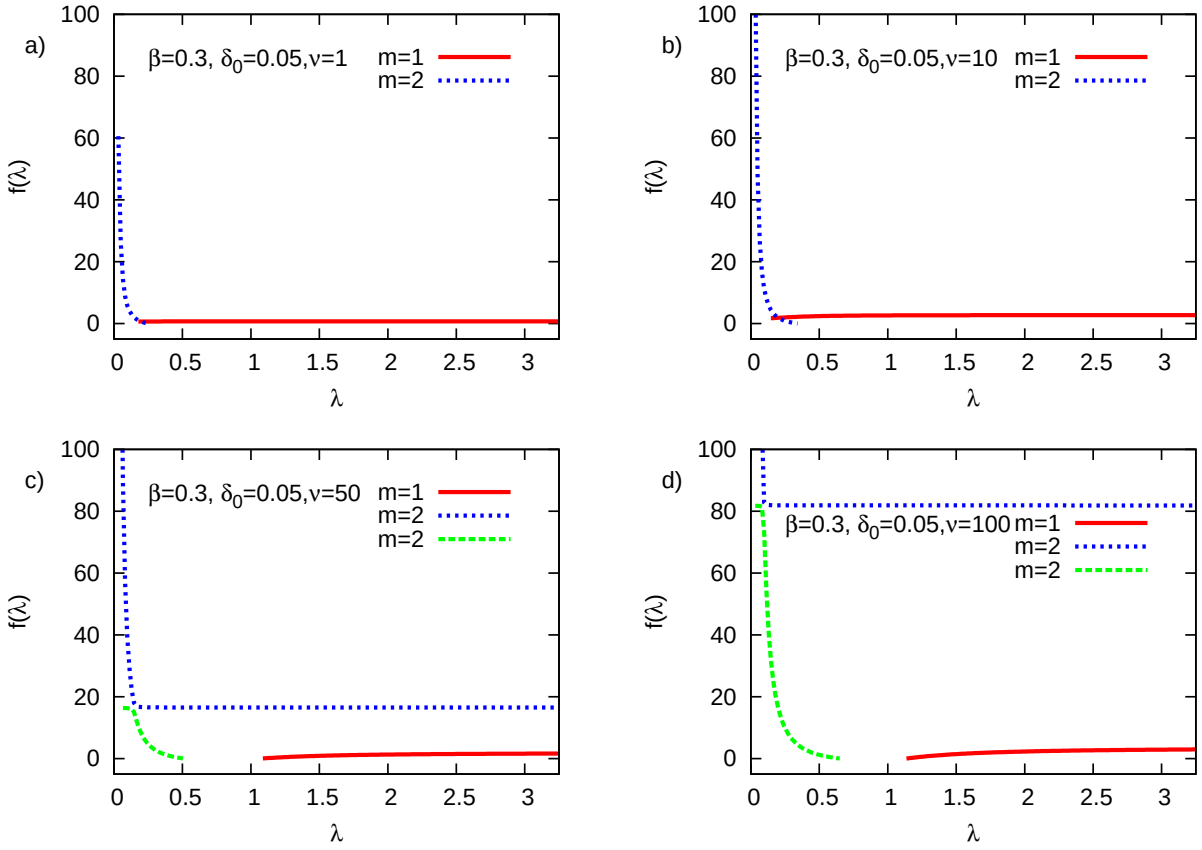

Figure 2.3: The function $f(\lambda,\ m)$ for $\beta = 0.3$ and $\delta_0 = 0.05$ in the unaligned logarithmic case with $\beta_1 = 1/4$. In the lower two panels, the two branches of f_1 and f_2 with $f_1 > f_2$ are shown for each $m \geq 2$. Note that for small λ, f_1 and f_2 branches do not cross each other, although they appear to be extremely close.

given $f_1 = 19$ and $\nu = 50$, the exact value of λ and so B_z cannot be determined with certainty. In contrast to f_1, f_2 varies for $\nu = 50$ over a larger range of $\lambda = (0.1, 0.5)$. In this range of λ, one can determine for each f_2 the associated λ and thus B_z through $B_z = 2\pi\sqrt{\mathrm{G}\Sigma_0^g}/\lambda$. The tighter the spiral arms are wound, the more dark matter is needed in order to maintain stationary logarithmic spiral patterns. This is a general trend of variation and is valid for both roots of f. Nevertheless, there exists a certain ν_0 value such that the second solution f_2 appears with a much less amount of dark matter for $\nu > \nu_0$. In other words, with increasing ν the dark matter amount also increases, except for the second solution with $\nu > \nu_0$. Physically, the two roots f_1 and f_2 are equally valid. But compared with the observational value of $f \approx 10$ for typical spiral galaxies, f_1 appears too large, e.g. for $\nu = 50$ and $f_1 \approx 19$ within the range of $\lambda = (0.2,\ 3.25)$. In comparison, the lower f_2 appears more plausible because of its smaller values instead of the very large values of f_1. For

$\nu = 100$, one can again find a relation between the f_2 curve and the magnetic field (represented by λ) and it is thus also possible to determine B_z through the f ratio. If the curve $f_2(\lambda)$ is sufficiently steep, so that a one-to-one relation is present between f_2 and λ, then the magnetic field strength B_z can be determined by integral (2.19) into

$$B_z = \frac{2\pi\sqrt{\mathrm{G}}\Sigma_0^g}{\lambda} \,. \tag{2.104}$$

The only additional variable that one needs to know is the surface mass density of the magnetized gas disc.

In this work, we have not explored situations of $\nu \neq 0$ and $\beta_1 \neq 1/4$ for which both parameters M and $Y_m(\beta_1 - i\nu/2)$ are complex. In this case, an additional study is needed to explore the variation of β_1 and its influence on the gravitational potential ratio f. Physically, β_1 is the constant scale-free index of surface mass density perturbations. A larger β_1 corresponds to a steeper radial profile of stationary coplanar perturbations in magnitudes.

2.10 Two limiting cases

In the first limit of large λ regime (i.e. $B_z \to 0$), we readily reproduce the model results of Shen & Lou (2004) where the gravitational coupling of two scale-free stellar and gaseous discs in the absence of magnetic field is analysed. For the absence of magnetic field, we choose a sufficiently large isopedic parameter $\lambda = 24$. The dependence of ratio f on the parameters β (a), δ_0 (b) and ν (c) is shown in Figure 2.4. For the choice of $\delta_0 = 0.05$ and $\nu = 0$, only the case of $m = 1$ has stationary perturbation solutions. The variation of δ_0 enables $m \geq 2$ to have stationary perturbation configurations as already mentioned in Section 2.8. For $\nu = 0$, each m corresponds to only one stationary perturbation solution. When ν is sufficiently small, only $m = 1$ perturbation configurations have stationary solutions. As ν is gradually increased, one can see clearly in Figure 2.4 panel c) that stationary perturbation solutions for $m \geq 2$ also appear.

In the second limit of large δ_0 (i.e. $\Sigma_0^{(s)} \to 0$) for young galaxies in the early universe, we recover the results of Lou & Wu (2005) where global MHD perturbation configurations in a single isopedically magnetized gaseous disc are studied. Figure 2.5 shows different variations of f ratio for the aligned and unaligned logarithmic cases in that regime. Two branches f_1 and f_2 roots are shown with $f_1 > f_2$ for each $m \geq 2$. While they appear very close, f_1 curve does not intersect f_2 curve at small λ. In principle, all m values can have corresponding stationary solutions for global perturbation configurations. This depends on the choice of λ and the combination of different parameters such as $k^{(s)}$, $k^{(g)}$ or $S^{(g)}$. For $m = 1$, the starting point of stationary

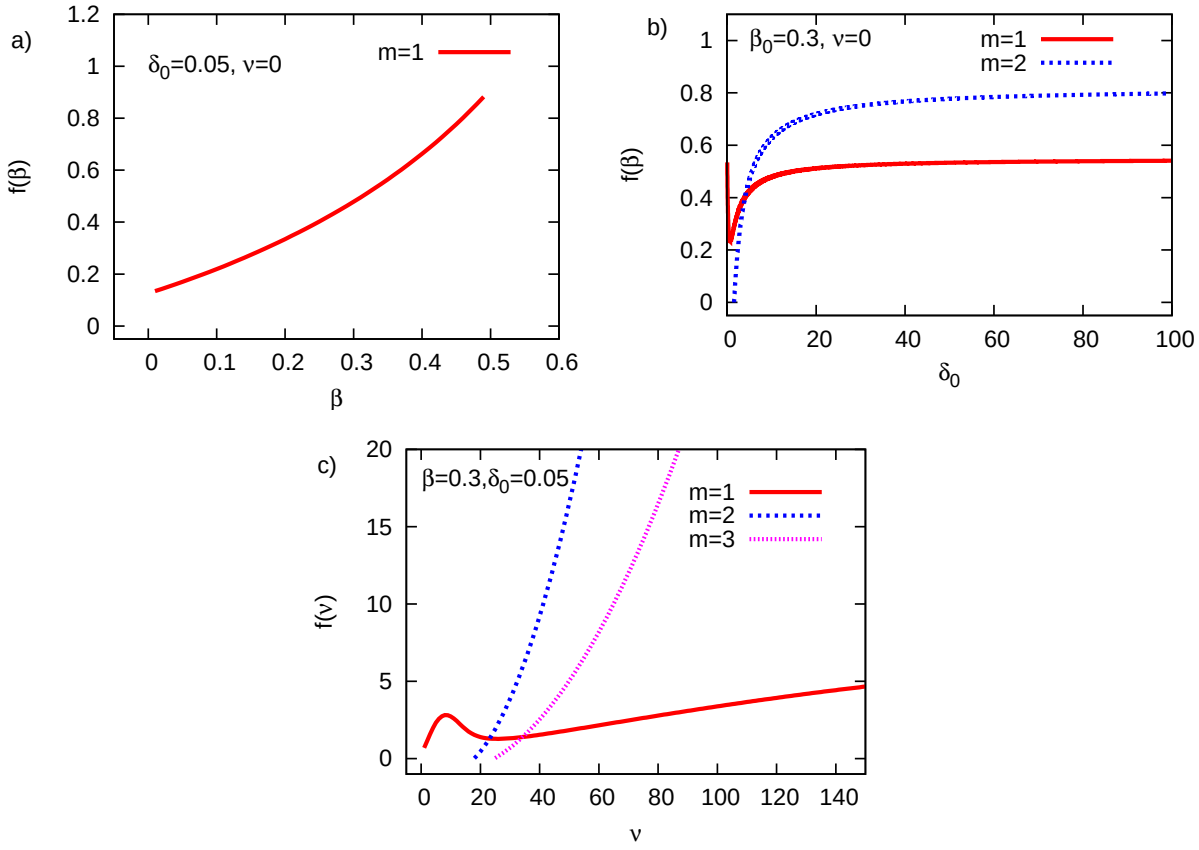

Figure 2.4: Study of the limiting case of no magnetic field is approximately realized by setting a large isopedic parameter $\lambda = 24$ and variation of β (a), δ_0 (b) and ν (c)

solutions for the aligned case is $\lambda \approx 1.1$ and for the unaligned case it is slightly shifted to $\lambda \approx 1.2$. For $m = 1$ the range of ratio $f = (0.01,\ 0.5)$ is very small for $\nu = 0$ as compared to range $f = (1,\ 60)$ for $\nu = 100$. For $m \geq 2$, a variation of β parameter in the range of $\beta = (0.1,\ 0.49)$ for the background composite disc configuration does not affect features of $f(\lambda)$ curves significantly. In the model of Wu & Lou (2006), potential ratio f is studied for different properties of the magnetized gaseous disc alone (such as the sound speed) at a certain specified value of λ parameter. The special case of one single magnetized gaseous disc in our model is complementary to their analysis.

Again, the basic fact that typically $f \lesssim 10$ must be kept in mind for applications to spiral galaxies. Due to their smaller values for $\nu = 100$, the minus-sign solution f_2 is regarded as more plausible.

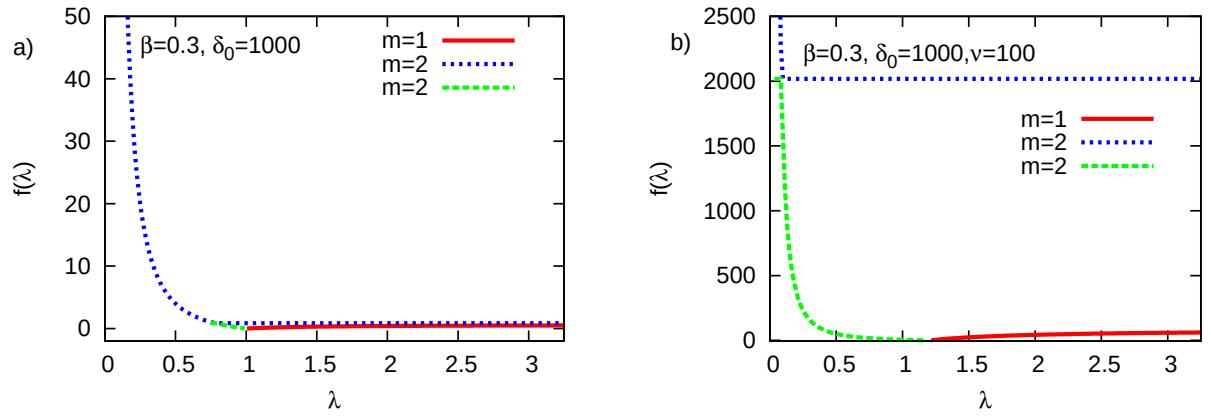

Figure 2.5: The limiting case of only one single isopedically magnetized gaseous disc is approximately achieved by setting $\delta_0 = 1000$. Two branches f_1 and f_2 roots are shown with $f_1 > f_2$ for each $m \geq 2$. While they appear very close, f_1 curve does not intersect f_2 curve at small λ.

2.11 Conclusion

Global stationary solutions for aligned and unaligned logarithmic perturbation configurations with a constant radial flux of angular momentum have been explored. Special attention has been paid to the roles of dark matter halos, represented by the f parameter, for the gravitational potential ratio and the isopedic parameter λ. For this purpose, the stationary dispersion relation for global perturbations is derived and a quadratic equation of f is obtained. In our model formulation, the stationary assumption is applied as a very special limiting case of the QSSS hypothesis (e.g. Bertin & Lin 1996 and references therein) which itself is already a very strong requirement to the disc dynamics. For a non-vanishing small pattern speed of a few $\mathrm{km\ s^{-1}\ kpc^{-1}}$ (adopted in the QSSS theory), a similar relation between f and B_z may be also derived.[4] Our sample calculations show that there are three possibilities for potential ratio f, corresponding to no solution, one solution and two solutions, respectively. In general, potential ratio f is a fairly complicated function of several independent model parameters involved. In order to explore the dependence of potential ratio f upon β, δ_0, λ, m and ν, we have chosen typical values for these relevant parameters to characterize late-type disc galaxies. Therefore, these results should be applicable to typical spiral galaxies for comparison. The main results are summarized below.

[4]Wu & Lou (2009, in preparation) obtained a dispersion relation for non-zero but small pattern speed and in the absence of the stellar disc component (see also our expression (2.77) and Wu & Lou 2006 for very small angular perturbation frequency ω). The range of potential ratio f should be determined in order to evaluate the importance of the isopedic magnetic field. Intuitively, the results for quasi-stationary and stationary configurations are expected to be qualitatively similar. Quantitative deviations are expected to be proportional to certain powers of pattern speed (e.g. Wu & Lou 2006).

2.11.1 $\nu = 0$ and $\beta_1 = \beta$

Global *aligned* perturbation configurations with $\nu = 0$ are studied for typical late-type galaxies with different β values, corresponding to various power-law radial fall-offs of the disc rotation curve. Examples of our numerical exploration show that in the estimated range of λ for disc galaxies, a variation of β parameter has no significant impact on global stationary perturbation configurations with $m \geq 1$. As a general trend, a stronger magnetic field allows existence of stationary perturbation configurations for $m \geq 2$. For weaker magnetic fields, only stationary perturbation configurations with $m = 1$ (i.e. lopsided cases) may exist. We have also explored stationary perturbation configurations for a disc galaxy at different epochs of evolution by varying the disc surface mass density ratio $\delta_0 = \Sigma_0^{(g)}/\Sigma_0^{(s)}$. By our sample calculations, the variation of δ_0 strongly affects the behaviour of $f(\lambda)$. This is a consequence of the fact that the magnetic field directly affects the gaseous disc and in an earlier stage of galaxy evolution, the gas fraction is higher in a composite disc system. With increasing δ_0 ratio towards earlier epochs (i.e. at higher cosmological redshifts in the early universe), the range of allowed stationary perturbation configurations for $m \geq 2$ also increases while that for $m = 1$ shrinks. In our simple scenario, δ_0 parameter marks the evolution of a disc galaxy in the expanding universe. At the beginning, a proto-spiral galaxy is presumably composed of a nebulous gas disc and a dark matter halo (e.g. Lou & Wu 2005; Wu & Lou 2006). During the evolution of a spiral galaxy, more and more stars are born and die, and thus the disc mass ratio δ_0 decreases slowly with time. With this scenario in mind, we interpret Figure 2.2 as follows. At an earlier stage of disc galaxy evolution, stationary solutions of global perturbation configurations with $m \geq 2$ exist over a wider range of λ. The influence of magnetic fields there is also stronger as the curve $f(\lambda)$ varies significantly over a larger range of λ, indicating a wider range for magnetic field strengths.

This brings out an extremely interesting evolutionary perspective for speculations. Observationally, the global star formation rate (SFR) in spiral galaxies is an important indicative parameter to characterize the galactic evolution. Conceptually, if one attempts to relate this SFR with disc instabilities, the application of Toomre's criterion (Safonov 1960; Toomre 1964) to a stellar disc alone would be insufficient because stars are directly born in the gaseous disc. Following this line of reasoning, one needs at least to explore instabilities in a composite system of stellar and gas discs (e.g. Lou & Fan 1998, 2000 and references therein) in the presence of a massive dark matter halo. The importance of magnetic fields is generally recognized in the dynamics of star-forming cloud cores. Nevertheless, how to specifically relate physical processes of star formation in clouds on much smaller scales and of large-scale disc instabilities remains a challenging problem due to the tremendous differences in scales. In spite of this challenge, we have developed intuitive feelings that regions of high gas density and strong magnetic fields on large scales are expected

to be vulnerable or favorable to active star formation processes. Now in a highly simplified dynamic manner, our model analysis brings together several important aspects for this physical consideration, viz. dark matter halo, magnetic field, and higher gas fraction (i.e. larger δ_0) in a composite disc system. The initial conditions for forming a proto-galactic disc nebula such as the dark matter halo, gas disc and magnetic field are expected to be statistical with fluctuations. The instability properties of such a magnetized disc system in the presence of a dark matter halo may then grossly determine the global SFR and thus the galactic evolution. In other words, different initial conditions can lead to different kinds of evolutionary tracks. In particular, it is conceivable that the SFR may have highs and lows along galactic evolutionary paths in the expanding universe. This information would be valuable for understanding the overall cosmological evolution in terms of global SFRs of spiral galaxies.

To compare a late-type spiral galaxy with an early-type spiral galaxy, we emphasize that stationary perturbation solutions for $m \geq 2$ are very different in these galaxies. In a late-type spiral galaxy of $\delta_0 \sim 0.05$, stationary perturbation configurations of $m \geq 2$ can only exist for strong magnetic fields while in an earlier stage of evolution, such solutions can exist for almost all λ values. These results suggest that multiple-armed disc galaxies may be more numerous in the early universe. It may be possible for disc galaxies to change patterns during the course of their evolution. Conceivably evolving on cosmological timescales, a disc galaxy pattern may alternately become stationary or quasi-stationary as evidenced by the fact of changing δ_0 and λ, e.g. f and $m \geq 2$ are shifted towards smaller λ for stationary configurations. This offers a novel perspective to relate global SFRs of disc galaxies and the galactic pattern speed evolution. For example in numerical simulations, one may start from initially stationary perturbation configurations and then explore time-dependent quasi-stationary behaviours as well as nonlinear effects of a composite disc system by adjusting one or several relevant parameters systematically.

2.11.2 $\beta_1 = 1/4$ and $\nu \neq 0$

Parameter ν characterizing radial variations of coplanar perturbations affects f ratio in many ways. For example, in spiral galaxies with more tightly wound logarithmic spiral arms (i.e. larger ν), more dark matter is needed in the massive halo to sustain stationary perturbation configurations. Furthermore, with increasing ν towards the Wentzel-Kramers-Brillouin-Jeffreys (WKBJ) regime, each f may correspond to multiple stationary configurations. For very small ν in the opposite limit, only perturbation configurations with $m = 1$ have stationary solutions (i.e. lopsided configurations). Stationary perturbations with $m = 1$ also have solutions for larger ν, but only in a certain range of $\lambda \approx (1.2,\ 3.25)$. Larger ν values have one stationary solution for all $m \geq 2$, namely the f_1 root of expression (2.101). If ν is increased further, then the second

root f_2 of expression (2.101) also fulfills all necessary physical requirements on f parameter. Here, f_2 root is always smaller than f_1 root and we expect that whenever there are two theoretical solutions possible, then f_2 tends to be the more realistic root because of its relatively lower values. The limiting case of $\nu \to \infty$ represents tightly wound spiral arms and the well-known WKBJ approximation (Lin & Shu 1964, 1966) should become applicable.

The curve $f_2(\lambda)$ shows that there is a one-to-one correspondence between f_2 root and strong magnetic fields. Therefore, by determining f_2 ratio through observations (e.g. rotation curves or gravitational lensing effects) and Equation (2.43), the magnetic field strength can also be determined. For weak magnetic fields, root f_2 does not vary significantly enough and thus, isopedic magnetic field strength B_z cannot be sensibly determined as a result of uncertainties in galactic observations.

2.11.3 Two limiting cases

The two limiting cases of $\lambda \to \infty$ and $\delta_0 \to \infty$ have been explored in the previous section. In the limit of $\lambda \to \infty$, the magnetic field almost vanishes and one comes back to a two gravitationally coupled hydrodynamic discs system with an axisymmetric dark matter halo. For late-type spiral galaxies, only perturbation configurations of $m = 1$ lead to stationary aligned solutions with a positive f ratio. For unaligned logarithmic perturbation configurations with $m \geq 2$, the existence of stationary solutions also depends upon the choice of dimensionless 'radial wavenumber' ν. For early-type spiral galaxies of higher δ_0, global stationary solutions of all m for perturbation configurations can be found. As already noted, this implies the possibility of more numerous multiple-armed spiral galaxies in the early universe.

For $\delta_0 \to \infty$ (see Figure 2.5 for large δ_0), stationary perturbation solutions for $m \geq 2$ can be found for every chosen parameter set. For $m = 1$, solutions exist in a certain range of λ. For example for $\nu = 100$ and $\delta_0 = 1000$, the case of $m = 1$ has f roots for $\lambda = (1.2,\ 3.25)$, which is shown in the right panel of Figure 2.5.

To conclude for $\delta_0 \to \infty$, for small ν or $\nu = 0$, all m values have one f root. But for larger ν, the case of $m \geq 2$ can have two f roots. This is equivalent to $\delta_0 = 0.05$. The difference lies in the values of f. The larger the 'radial wavenumber' ν value is, the larger are the potential ratios f_1 and f_2.

For late-type spiral galaxies and unaligned logarithmic cases, a weak magnetic field does not play a significant role as expected. The younger the spiral galaxy is, the more important is the role of a magnetic field, especially in the regime of stronger magnetic fields. For very strong magnetic fields, it appears that f ratio is more closely connected to the magnetic field and the effect of magnetic fields cannot be ignored. But for weak magnetic fields, f ratio remains more or less

constant for all types of spiral galaxies.

Our results can be summarized as follows. First of all, we emphasize that the lopsided global configuration $m = 1$ is an exceptional case for which the curve $f(\lambda)$ has a distinctly different shape as compared to those for the cases $m \geq 2$. For both aligned and unaligned logarithmic spiral cases with $m \geq 2$, strong magnetic fields, which still are chosen realistic in spiral galaxies, can bear a significant relation to the dark matter halo in maintaining globally stationary perturbation configurations.

Physically, we conclude that in spiral galaxies with or without radial variations in perturbations, weak magnetic fields do not influence stationary perturbation configurations. But when the magnetic field strength is increased, a globally stationary perturbation configuration would then become non-stationary if the f ratio is not high enough for the increased magnetic field strength. A change of perturbation patterns might be possible during the course of the galaxy evolution. For example, flocculent galaxies might represent the transitional phase for global pattern changes of galaxies. This prediction may be tested by numerical simulations and by deep survey of morphological observations for galaxies in the early universe.

Our model analysis has shown that the magnetic field needs to be sensibly chosen with other given disc parameters in order to maintain a global perturbation configuration with a stationary pattern in our frame of reference. Therefore, a variation or an adjustment of B_z may put a stationary perturbation configuration into a non-stationary one or a non-stationary perturbation configuration into a stationary one because there exists a one-to-one correspondence between the potential ratio f and a sufficiently strong magnetic field B_z for globally stationary perturbation configurations. For such a stationary disc balance in general, the potential ratio f can vary in a considerably large range depending on the choice of other relevant parameters in sensible regimes. As expected on intuitive ground, sufficiently weak magnetic fields exert fairly small influence on stationary perturbation configurations in our composite model. The main reason is that the magnetic pressure and tension together are not strong enough as compared with other forces which play important dynamic roles in our composite system.

In the regime of weak magnetic fields, there also exist instabilities widely explored in literature. The magneto-Jeans instability (MJI) is an instability which is based on background in-plane magnetic fields. In recent years, several authors (e.g. Kim & Ostriker 2001; Kim, Ostriker & Stone 2002; Shetty & Ostriker 2006) have performed numerical MHD simulations for galaxies. In particular, they studied azimuthal magnetic fields that lie in the disc plane (see also Lou & Zou 2004, 2006; Lou & Bai 2006). For our study of isopedic magnetic fields, as already mentioned, Lou & Wu (2005) have proven that a constant λ is a consequence of the frozen-in condition on magnetic flux (see also Wu & Lou 2006). Our composite MHD model offers a two-dimensional description of an isopedic magnetic field. Due to the idealization of razor-thin discs, perturbations

lie in the galactic plane and have no $\hat{z}-$components. Hence, a treatment of the magnetorotational instability (MRI) is impossible due to its necessary requirement of a perturbation $e^{ik_z z}$ along $\hat{z}-$direction (Chandrasekhar 1960; Balbus & Hawley 1991, 1998; Balbus 2003). When switching over to discs of finite thicknesses, the MRI must be included and a larger f is probably needed in order to counteract MRIs. With our theory, the range of strong vertical magnetic fields is well studied, whereas the effect of weak magnetic fields is underestimated since we do not account for MRIs which play an important role for weak magnetic fields. The results that we obtain here cannot be directly applied to coplanar magnetic fields, thus we can make no predictions for the MJIs.

The galactic application of our disc model results leads to two methods which may be utilised to determine either the isopedic magnetic field strength B_z or the mass of an axisymmetric dark matter halo. First, by using Equation (2.43) through observations of a disc galaxy, one can estimate the gravitational potential ratio f. In the case of a stationary pattern of a perturbation configuration, only one distribution of magnetic field strengths is possible for this f value. This is a new approach of determining the distribution of isopedic magnetic field strengths in disc galaxies. Proceeding in the opposite direction, these model results may also be applied to determine f ratio by using observationally inferred distribution of magnetic field strengths. This appears to be an alternative method to estimate the halo mass of dark matter. The real challenge of these procedures is to determine whether a perturbation pattern is stationary or quasi-stationary through independent observational diagnostics. In practice, the relevant parameters that need to be determined by galactic observations for our proposed method to work are m, β (the scaling index for radial variations of unperturbed disc variables), β_1^d (the scaling index for radial variations of perturbation disc variables), unperturbed disc surface mass densities $\Sigma_0^{(i)}(r)$, effective sound speeds $a^{(i)}$, either λ (for the determination of gravitational potential ratio f) or the other way around f (for the determination of distribution of magnetic field strengths B_z). It is indeed a challenging task for observations to specifically identify some of these parameters. To the best of our knowledge, galactic observations up to date have not yet determined completely all of these parameters with error bars in one galaxy.

In addition, this work can also be understood as a preparation for the subsequent study on MHD density waves in such a composite disc system since all relevant quantities and their relations among each other are presented in this work. In reference to singular isothermal disc (SID) models of Shu & Li (1997), Shu et al. (2000), Lou & Shen (2003), Lou & Zou (2004, 2006), Shen et al. (2005), there exist two classes of solutions for stationary magnetohydrodynamic (MHD) perturbation configurations with in-phase and out-of-phase density perturbations in the two discs. For the case of a scale-free stellar disc and an isopedically magnetized scale-free gaseous disc embedded in an axisymmetric dark matter halo, we expect that there are also two

classes of in- and out-of-phase density perturbations. The formulae and results obtained here can be applied later to analyse such MHD density waves.

3

Numerical simulations of disc galaxies

3.1 Introduction

In the past 20 years, computational technologies have advanced rapidly allowing astronomers today to perform simulations with a resolution that has never been reached in the past. Currently, simulations of large-scale evolutions in the universe (e.g. Springel et al. 2001; Yoshida et al. 2003) as well as star formation processes in gas and molecular clouds (e.g. Bonnell et al. 2006) are possible.

In the context of isolated galaxies, numerical studies have mainly concentrated on two different features. The first focus of these studies deals with the evolution study of isolated galaxies composed of stellar and gaseous particles in the presence of a dark matter halo (e.g. Li et al. 2005). The gross structure of the galaxies studied here are all flocculent. The second focus deals with the response of gas to a spiral potential. The spiral potential is assumed to be created by the more massive stellar disc in the galaxy (e.g. Dobbs & Bonnell 2007, 2008). The numerical simulation of an isolated galaxy with a long-lived grand-design spiral structure has still not been realized so far. The most promising theory for these long-lived features predicts the presence of density waves in the disc.

In this part of my work, numerical simulations of isolated galaxies with different methods of creating grand-design spiral galaxies are presented. The primary goal is to test whether large-scale density waves in realistic galaxies can be produced numerically with current computational resources as well as the study of lifetime of density waves. In the past, density waves have been realized numerically for rotating stellar discs (e.g. Griv & Chiueh 1994). The realization of density waves in galaxies with gas and stellar components however has still not been done. In the context of spiral arms, so-called material arms or kinematic density waves have accompanied

these studies for more than 40 years. Material arms consist of the same matter and can wind up very fast in time. This is called the 'winding problem'. Kinematic density waves also show the winding up mechanism of the arms, but slower. In contrast to them, classical density waves that were proposed by Lin & Shu (1964) do not wind up and can persist for a long time. Determining the presence of winding in numerical results is crucial for differing classical density waves (as proposed by Lin & Shu 1964) from material arms or kinematic density waves.

Due to observations of O- and B-stars in the spiral arm regions, a numerical realization of star formation there is also desired to match numerical and observational results. Another mechanism that is expected to play an important role in the interstellar medium (ISM) is stellar feedback. Possible influences of stellar feedback on the large-scale structure of spiral galaxies is therefore the final feature to study.

Simulations are performed with the publicly available simulation code GADGET-2 (Springel 2005), in combination with several additional routines. In Section 3.2, an explanation of the main features in respect to the results is presented. Given the complexity of the code, readers interested in all other features are referred to Springel (2005). Additional routines inserted into the original code are described in Section 3.3. These routines are star formation, stellar feedback, external potential and perturber.

Star formation takes place in every disc galaxy under certain particular circumstances. Stellar feedback is thought to play a fundamental role in the evolution of galaxies since supernovae (SNe) are considered as the most efficient mechanisms to eject metals and energy into the interstellar medium (ISM). On the other hand supernova events affect the star formation history and therefore the evolution of entire galactic systems.

For the production of the grand-design spiral structure in the disc, three different methods are applied in our simulations. The first method uses a perturber passing by the galaxy. The second and third method apply an artificial external gravitational potential. For all three methods, it must be studied, whether the produced spiral arms are density waves or material arms.

In Section 3.4, the model used for the simulations and the parameter samples for different resolution levels are presented. The results are devided into two main parts.

- The first part, presented in Section 3.5, discusses simulations of isolated disc galaxies without any perturbations such as a passing object or an external potential. The primary goal of this part is to study possible influences of stellar feedback on the disc dynamics and star formation processes.

- In the second part (Sections 3.6, 3.7 and 3.8), we focus our work on the creation of a classical density wave first proposed by Lin & Shu (1964). As mentioned above, three different methods are applied.

- The first method is the fly-by of a punctual massive object (Section 3.6). Since it is often observed that spiral galaxies have companions, it is physically and also numerically (Toomre & Toomre 1972, Oh et al. 2008) possible to create a large-scale spiral structure by using a companion. Our emphasis lies in the study of the time-dependent evolution of the spiral arms in order to identify its real nature.
- The second method is to apply an external gravitational potential to the disc matter in order to force it to create a spiral structure (Section 3.7).
- Since the external potential, which is used in Section 3.7, affects the whole disc, a third method is studied in addition by applying the external potential only in the regions of dense spiral arms (Section 3.8). This third method is thought to be most similar to the idea of classical density waves, where a density wave propagates in an unperturbed disc.

Numerical results, which show face-on views of the galaxies, are created with the visualization program SPLASH (Price 2007). In Section 3.9 finally, we summarize and discuss the numerical results.

3.2 Selection of some relevant features in GADGET-2

GADGET-2 is a hybrid N-body / smoothed particle hydrodynamics (SPH) simulation package, which is able to simulate two different sorts of particles; namely N-body and SPH particles. While N-body particles only experience gravitational forces, SPH particles, as their name implies, also experience hydrodynamic forces.

In the description of disc galaxies, N-body particles represent the dark matter halo, the bulge and the stars in the disc. The gaseous component in the disc is described by SPH particles since gas and dust clouds are able to collapse and form stars. In clouds, friction also plays a role like in fluids. By using the SPH method, a fluid can be described by a set of discrete tracer particles. The quantities of the continuous fluid (such as the density $\rho(\vec{r}, t)$) are defined by a kernel interpolation technique (Gingold & Monaghan 1977, Lucy 1977, Monaghan 1992), which will be described in detail in this Section.

3.2.1 Hydrodynamic variables of gas

For the description of the gaseous component, the usage of an equation of state is necessary. In GADGET-2, an ideal gas as well as an isothermal gas can be simulated. All relevant relations for both cases are shown in Table 3.1, where ρ is the density of the gas particle, S the entropy,

$k_\mathrm{B} = 1.38 \times 10^{23}$ J/K the Boltzmann constant, T the temperature, m_p the proton mass, and m the mass of the gas particle. For our simulations shown in this work we act on the assumption of an ideal gas.

	Ideal	isothermal
γ	5/3	1
pressure	$p = S \cdot \rho^\gamma$	$p = S \cdot \rho = S \cdot \rho$
thermal energy	$E_\mathrm{th} = \frac{mS\rho^{\gamma-1}}{\gamma-1} = \frac{mp}{\rho(\gamma-1)} = \frac{k_\mathrm{B}Tm}{\mu m_\mathrm{p}(\gamma-1)}$	$E_\mathrm{th} = \frac{mp}{\rho} = mS = \frac{k_\mathrm{B}Tm}{m_\mathrm{p}}$
internal energy	$u = \frac{S\rho^{\gamma-1}}{\gamma-1} = \frac{p}{\rho(\gamma-1)} = \frac{k_\mathrm{B}T}{\mu m_\mathrm{p}(\gamma-1)}$	$u = \frac{p}{\rho} = S = \frac{k_\mathrm{B}T}{m_\mathrm{p}}$
sound speed	$c_\mathrm{s} = \sqrt{\frac{\gamma p}{\rho}}$	$c_\mathrm{s} = \sqrt{\frac{p}{\rho}} = \sqrt{\frac{k_\mathrm{B}T}{m_\mathrm{p}}}$

Table 3.1: Relations between different hydrodynamic variables

3.2.2 Computation of acceleration

Gravitational acceleration

In a sample of N arbitrary distributed particles in space, the Newtonian interaction (gravitational) potential at a position $\vec{r}_i$ takes the form

$$\phi(\vec{r}_i) = \mathrm{G} \sum_{j=1, j\neq i}^{N} \frac{m_j}{|\vec{r}_j - \vec{r}_i|} \,, \tag{3.1}$$

with G as the gravitational potential. The interaction force $\vec{F}_{i,\mathrm{grav}}(\vec{r}_i)$ and respective acceleration $\vec{a}_{i,\mathrm{grav}}(\vec{r}_i)$ of a particle with the mass m_i and the coordinate $\vec{r}_i$ accordingly are

$$\vec{F}_{i,\mathrm{grav}}(\vec{r}_i) = -m_i \vec{\nabla}\phi(\vec{r}_i) = \mathrm{G} \sum_{j=1,\ j\neq i}^{N} \frac{m_i m_j}{|\vec{r}_i - \vec{r}_j|^3}(\vec{r}_i - \vec{r}_j) \,, \tag{3.2}$$

$$\vec{a}_{i,\mathrm{grav}}(\vec{r}_i) = \mathrm{G} \sum_{j=1,\ j\neq i}^{N} \frac{m_j}{|\vec{r}_i - \vec{r}_j|^3}(\vec{r}_i - \vec{r}_j) \,, \tag{3.3}$$

The sum is calculated over all $N-1$ neighbours of the particle with index i.

For the computation of the gravitational force, GADGET-2 uses a so-called tree algorithm since a trivial sum over all forces results in an N^2-scaling of the computational time. Tree algorithms are very fast and can scale with e.g. $O(N \log N)$. The tree algorithm used in GADGET-2 is described in detail in Springel (2005).

When using Equations (3.2) and (3.3) without any modifications, a numerical problem arises due to the large gravitational force between two particles with indices i and j which have very small distance r_{ij} to each other:

$$|\vec{F}_{ij}| = \mathrm{G}\frac{m_i m_j}{r_{ij}^2} \to \infty \text{ for } r_{ij} \to 0 \; . \tag{3.4}$$

Since the time steps are inversely proportional to the gravitational acceleration (see also Section 3.2.3), this would lead to infinitesimal small time steps, which prevent the simulation from making progress in time.

In order to avoid this problem, the gravitational softening length ϵ is introduced according to

$$|\vec{F}_{ij}| = \mathrm{G}\frac{m_i m_j}{(r_{ij}+\epsilon)^2} \; . \tag{3.5}$$

In this way, the gravitational force becomes finite at distance $r_{ij} = 0$. It is desirable to make the correction factor ϵ as small as possible since every $\epsilon \neq 0$ leads to a gravitational force that differs from the physical gravitational force. The minimum gravitational softening length is dependent on the masses of the particles and determines the resolution of the simulation.

Hydrodynamical acceleration

For each hydrodynamic simulation the computation of the densities is an essential component of the program. In GADGET-2, the density estimate for the particle with index i is done by using the SPH smoothing kernel W and the relations

$$\rho_i = \sum_{j=1, j\neq i}^{N} m_j W(|\vec{r}_{ij}|, h_i) \; , \tag{3.6}$$

$$W(r,h) = \frac{8}{\pi h^3} \begin{cases} 1 - 6\left(\frac{r}{h}\right)^2 + 6\left(\frac{r}{h}\right)^3 \; , & 0 \leq \frac{r}{h} \leq \frac{1}{2} \; , \\ 2\left(1-\frac{r}{h}\right)^3 \; , & \frac{1}{2} < \frac{r}{h} \leq 1 \; , \\ 0 \; , & \frac{r}{h} > 1 \; . \end{cases} \tag{3.7}$$

The sum is calculated over all particles with distances $|\vec{r}_{ij}| = |\vec{r}_j - \vec{r}_i| \neq 0$ relative to the coordinate $\vec{r}_i$. h and h_i are the smoothing length within which a certain number of SPH neighbours N_{ngb} is required. In our simulations we apply $N_{\mathrm{ngb}} = 40$. N is the total number of particles, but the definition of the SPH smoothing kernel W shows that only particles with a distance $|\vec{r}_{ij}| = r_{ij} \leq h$ or $\frac{r_{ij}}{h} \leq 1$ are considered for the density computation. In general, the smoothing kernel W is

normalized for $h \to \infty$ to

$$\int_0^\infty W(\vec{r} - \vec{r}', h) d\vec{r}' = 1 \, . \tag{3.8}$$

In our case, it is limited to a finite value of h,

$$\int_0^h W(\vec{r} - \vec{r}', h) d\vec{r}' = 1 \, . \tag{3.9}$$

As shown in Figure 3.1, the smoothing kernel $W_{ij}(h) = W(|\vec{r}_i - \vec{r}_j|, h)$ is a decreasing function of r. In this way, more distant neighbours of a particle with index i are weighted less than close neighbours in the computation of the hydrodynamic variables.

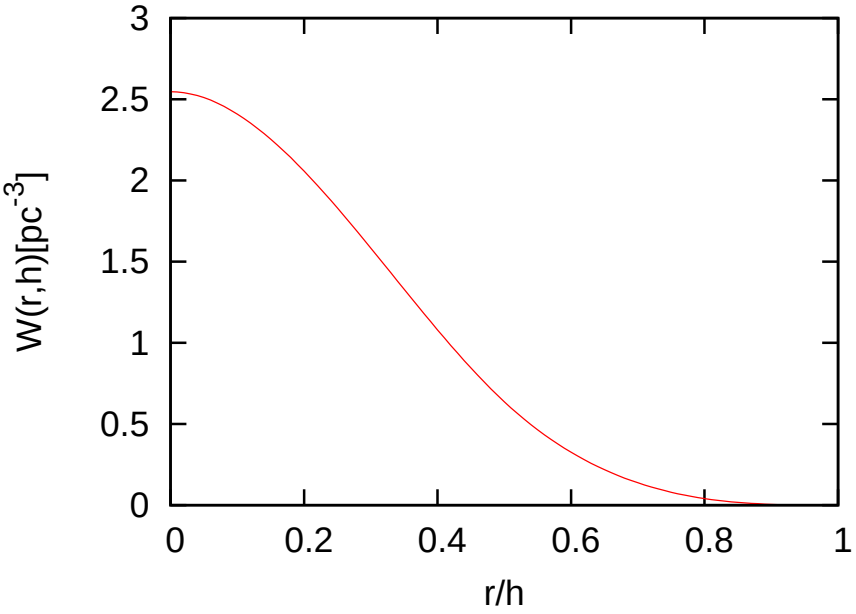

Figure 3.1: The smoothing length for $h = 1$ pc.

The hydrodynamical acceleration for SPH particles is given by (Springel 2005)

$$\frac{d\vec{v}_{i,\mathrm{hd}}}{dt} = \vec{a}_{i,\mathrm{hd}} = -\sum_{j=1}^{N} m_j \left[f_i \frac{p_i}{\rho_i^2} \vec{\nabla}_i W_{ij}(h_i) + f_j \frac{p_j}{\rho_j^2} \vec{\nabla}_i W_{ij}(h_j) \right] \, , \tag{3.10}$$

$$f_i = \left(1 + \frac{h_i}{3\rho_i} \frac{\partial \rho_i}{\partial h_i} \right)^{-1} \, . \tag{3.11}$$

p_i is the particle pressure for particle i with $p_i = S_i \rho_i^\gamma$ and S_i is the corresponding entropy. The

gradient of W can be expressed as

$$\vec{\nabla}_i W(r,h) = \begin{pmatrix} x_i - x_j \\ y_i - y_j \\ z_i - z_j \end{pmatrix} \frac{48}{\pi h^4} \begin{cases} \frac{1}{h}\left(\frac{3r}{h} - 2\right) , & 0 \leq \frac{r}{h} \leq \frac{1}{2} , \\ -\frac{1}{r}\left(1 - \frac{r}{h}\right)^2 , & \frac{1}{2} < \frac{r}{h} \leq 1 , \\ 0 , & \frac{r}{h} > 1 . \end{cases} , \tag{3.12}$$

Beside the standard hydrodynamical description of an ideal fluid, an artificial viscosity has to be included in order to capture the discontinuities that occur in the ideal gas. Thereby, kinetic energy is transformed into heat. The viscous force used in GADGET-2 is

$$\left.\frac{d\vec{v}_i}{dt}\right|_{\text{vis}} = \vec{a}_{i,\text{visc}} = -\sum_{j=1}^{N} m_j \Pi_{ij} \nabla_i \overline{W}_{ij} , \tag{3.13}$$

where $\overline{W}_{ij}$ is the arithmetic average of $W_{ij}(h_i)$ and $W_{ij}(h_j)$ and Π_{ij} is the viscous tensor. For Π_{ij}, many different forms can be used such as the Monaghan-Balsara form (Monaghan & Gingold 1983; Balsara 1995). GADGET-2 uses the modified Monaghan-Balsara form (Monaghan 1997)

$$\Pi_{ij} = -\frac{\alpha}{2} \frac{(c_i + c_j - 3w_{ij}) w_{ij}}{\rho_{ij}} , \tag{3.14}$$

with c_i and c_j denoting the sound speeds of the particles with indices i and j. α regulates the strength of the viscosity with typical values of $\alpha \cong 0.5 - 1$. w_{ij} is the relative velocity projected on to the separation vector, provided the particles approach each other.

$$w_{ij} = \begin{cases} \frac{\vec{v}_{ij} \cdot \vec{r}_{ij}}{|\vec{r}_{ij}|} & , \ \vec{v}_{ij} \cdot \vec{r}_{ij} < 0 \\ 0 & , \ \vec{v}_{ij} \cdot \vec{r}_{ij} > 0 \end{cases} . \tag{3.15}$$

For the artificial viscosity, a so-called viscosity-limiter is also used (Balsara 1995; Steinmetz 1996), since the single viscosity form (3.14) leads to spurious angular momentum transport when shear flows are present. Thereby, the viscous tensor Π_{ij} is multiplied by a factor $(f_i + f_j)/2$, with

$$f_i = \frac{|\vec{\nabla} \times \vec{v}|_i}{|\vec{\nabla} \cdot \vec{v}|_i + |\vec{\nabla} \times \vec{v}|_i} . \tag{3.16}$$

In contrast to a collisionless particle which only experiences a gravitational acceleration, the acceleration computed at each time step for a SPH particle is composed of three parts, namely the gravitational and the hydrodynamical acceleration and additionally the acceleration due to

artificial viscosity:

$$\vec{a}_{\rm tot} = \vec{a}_{\rm grav} + \vec{a}_{\rm hd} + \vec{a}_{\rm visc} \ . \tag{3.17}$$

Whenever the viscosity of a system is not zero, the thermal energy of the system will increase with time leading to an expansion of this system in space. A cooling mechanism is therefore necessary. Due to its complexity, we will not describe the whole cooling mechanism at this place. We refer the reader to Katz et al. (1996), which describes in detail all cooling processes that are included in our simulation. For our simulations, we assume primordial gas and a hydrogen abundance by mass of $X = 0.76$ and a helium abundance by mass of $Y = 0.24$.

3.2.3 Time step computation

For a collisionless particle with the index i the time step $\Delta t_{i,\rm grav}$ is computed via

$$\Delta t_{i,\rm grav} = \min \left[\Delta t_{\rm max}, \left(\frac{2\eta\epsilon}{|\vec{a}_{i,\rm grav}|} \right)^{1/2} \right] \ . \tag{3.18}$$

ϵ is the gravitational softening length of the particle, $\Delta t_{\rm max}$ the maximum allowed time step and η is an accuracy parameter. The current gravitational acceleration $\vec{a}_{i,\rm grav}$ is the only parameter needed for the calculation of the next time step.

For SPH particles, the next time step equals to $\min(\Delta t_{\rm i,grav}, \Delta t_{\rm i,HD})$. $\Delta t_{\rm i,grav}$ and $\Delta t_{\rm i,HD}$ are computed as follows:

$$\Delta t_{i,\rm grav} = \min \left[\Delta t_{\rm max}, \left(\frac{2\eta\epsilon}{|\vec{a}_{i,\rm tot}|} \right)^{1/2} \right] \ , \tag{3.19}$$

$$\vec{a}_{i,\rm tot} = \vec{a}_{i,\rm grav} + \vec{a}_{i,\rm hd} + \vec{a}_{i,\rm visc} \ , \tag{3.20}$$

$$\Delta t_{i,\rm HD} = \frac{C_{\rm courant} h_i}{\max_j (c_i + c_j - 3w_{ij})} \ , \tag{3.21}$$

$C_{\rm courant} = 0.3$ is the courant factor. The maximum is determined with respect to all neighbours j of the particle with index i.

3.3 Additional numerical subroutines

On the basis of the original simulation code, we have added several additional routines in order to describe star formation, stellar feedback, an external potential and the interaction of perturber.

In disc galaxies, star formation takes place in the ISM where molecular clouds satisfy the so-called *Jeans criterion*. The Jeans criterion describes the interplay between gravitational collapse and gas pressure of the clouds. When the gravitational force is stronger than the gas pressure, the cloud can collapse and form stars. This is fullfilled, when the Jeans mass for a certain density ρ is exceeded.

$$M_{\rm cloud} > M_{\rm J} = \left(\frac{5k_BT}{G\mu \cdot m_{\rm u}}\right)^{3/2} \left(\frac{3}{4\pi\rho}\right)^{1/2} , \tag{3.22}$$

with $k_{\rm B}$ being the Boltzmann constant, T the mean temperature of the cloud, G the gravitational constant, μ the mean mass of the gas atoms given in atomic mass unit u, $m_{\rm u}$ the atom mass constant and ρ the density. $\mu \cdot m_{\rm u}$ is also defined as the mean molar mass. Criterion (3.22) is derived by assuming a homogeneous and static sphere for the gas cloud.

Massive stars have at least 8 solar masses ($\mathrm{M}_\odot$). They lose mass during their evolution, which is called stellar wind. At the end of their lifetime stars with $M \lesssim 40\,\mathrm{M}_\odot$ explode as supernovae (SNe) leaving a remnant such as a neutron star or a black hole. The lifetime of a star with mass M can be expressed as

$$\tau[\mathrm{yr}] = 10^{10} \left(\frac{\mathrm{M}_\odot}{M}\right)^{2.5} . \tag{3.23}$$

Massive stars with SNe explosions hence have typical lifetimes between $\tau(8\,\mathrm{M}_\odot) = 5,5 \times 10^7\,\mathrm{yr}$ and $\tau(40\,\mathrm{M}_\odot) = 10^6\,\mathrm{yr}$.

3.3.1 Star formation

Based on known star formation processes in molecular clouds, a star formation module is inserted, which is adequate for the chosen resolution levels.

We use the method described by Katz (1992), which states that a gas particle can form stars when its density exceeds the critical density (Equation 3.24), it is in a converging flow (Equation 3.25) and it fullfills the third condition (3.26).

$$\rho_i \geq \rho_{\rm crit} , \tag{3.24}$$

$$\vec{\nabla} \cdot \vec{v}_i < 0 , \tag{3.25}$$

$$p_{\rm rand} < p_* , \; p_* = \frac{m_{\rm gas}}{m_*} \left[1 - \exp(-\frac{c\Delta t}{\tau_{\rm dyn}})\right] , \tag{3.26}$$

$$m_* = \epsilon^* \cdot m_{\rm gas,0} , \; \tau_{\rm dyn} = \frac{1}{\sqrt{4\pi \mathrm{G}\rho}} . \tag{3.27}$$

$p_{\rm rand}$ is a random number between 0 and 1, m_* the mass of the formed stellar mass, $m_{\rm gas}$ the mass of the considered gas particle, $c = 0.1$ the star formation efficiency, Δt the time-step of the code, $\tau_{\rm dyn}$ the dynamical time of the particle, ρ_i the density of the gas particle and $\vec{v}_i$ the velocity of the gas particle. ϵ^* is chosen to be 0.3. Criterion (3.26) is the physical requirement that the cooling time of the gas particle is shorter than the dynamical time $\tau_{\rm dyn}$ (Katz 1992). If the cooling time is longer than $\tau_{\rm dyn}$, the cloud first has to cool until it can form stars. Criterion (3.26) is only used for the case when $m_{\rm gas} > 0.3 \cdot m_{\rm gas,0}$, with $m_{gas,0}$ being the initial gas mass. If $m_{\rm gas}$ falls below $0.3 \cdot m_{\rm gas,0}$, the gas particle is directly converted into a stellar particle without testing criterion (3.26) in order to prevent stars that are too small.

The divergence of velocity is computed by using the basic form of density computation.

$$\rho_i = \sum_{j=1, j\neq i}^{N} m_j W(|\vec{r}_i - \vec{r}_j|, h_i) \; , \tag{3.28}$$

$$W(r,h) = \frac{8}{\pi h^3} \begin{cases} 1 - 6\left(\frac{r}{h}\right)^2 + 6\left(\frac{r}{h}\right)^3 \; , & 0 \leq \frac{r}{h} \leq \frac{1}{2} \; , \\ 2\left(1 - \frac{r}{h}\right)^3 \; , & \frac{1}{2} < \frac{r}{h} \leq 1 \; , \\ 0 \; , & \frac{r}{h} > 1 \; . \end{cases} \tag{3.29}$$

$$\vec{\nabla} \cdot \vec{v}_i = \frac{1}{\rho_i} \sum_{j=1, j\neq i}^{N} m_j (\vec{v}_j - \vec{v}_i) \cdot \vec{\nabla}_i W(|\vec{r}_i - \vec{r}_j|, h_i) \; . \tag{3.30}$$

The gradient $\vec{\nabla}_i W(r, h_i)$ in Equation 3.30 is determined to

$$\vec{\nabla}_i W(r, h_i) = \begin{pmatrix} x_i - x_j \\ y_i - y_j \\ z_i - z_j \end{pmatrix} \frac{48}{\pi h_i^4} \begin{cases} \frac{1}{h_i}\left(\frac{3r}{h_i} - 2\right) \; , & 0 \leq \frac{r}{h_i} \leq \frac{1}{2} \; , \\ -\frac{1}{r}\left(1 - \frac{r}{h_i}\right)^2 \; , & \frac{1}{2} < \frac{r}{h_i} \leq 1 \; , \\ 0 \; , & \frac{r}{h_i} > 1 \; . \end{cases} \; . \tag{3.31}$$

3.3.2 Stellar feedback

The stellar particles, which are formed from the gas particles, do not only represent single stars, but rather stellar clusters due to the large masses of their host gas particles. Single stars of several solar masses still cannot be resolved due to the required large numbers of particles.

For star forming regions observations can determine the so-called initial mass functions (IMF), which provide the relative number of stars in these regions as a function of their masses (e.g. Elmegreen 2000, Adams 2003). By using such an IMF, we are therefore able to determine the number of stars with $8\ {\rm M}_\odot \leq M_{\rm s} \leq 40\ {\rm M}_\odot$ for each stellar particle formed and simulate SNe for them.

We adopt the IMF (Miller & Scalo 1979) shown in Equation (3.32).

$$f(m) = \begin{cases} \mathrm{A} \cdot m^{-1.4} & 0.1 \leq m \leq 1 \\ \mathrm{A} \cdot m^{-2.5} & 1 \leq m \leq 10 \\ \mathrm{A} \cdot m^{-3.3} & m > 10 \end{cases} \quad m = \frac{M_\mathrm{s}}{\mathrm{M}_\odot} \,. \tag{3.32}$$

$f(m)$ is the number of single stars with masses $M_\mathrm{s} = m \cdot \mathrm{M}_\odot$. A is a normalizing constant, which can be determined by using

$$\sum_{m=0.1}^{50} f(m) M_\mathrm{s} = \sum_{m=0.1}^{50} f(m) m \mathrm{M}_\odot = M_* \,, \tag{3.33}$$

$$\mathrm{A} = \frac{M_*}{\mathrm{M}_\odot (\sum_0^{0.1} m^{-0.4} + \sum_1^{10} m^{-1.5} + \sum_{10}^{50} m^{-2.3})} \,. \tag{3.34}$$

M_* is the mass of the stellar particle formed representing a stellar cluster with stellar masses M_s between 0.1 and $50\ \mathrm{M}_\odot$.

The mass and thermal energy ejection of a stellar particle is computed by augmenting the masses and thermal energies of the neighbouring gas particles. For this mass and energy distribution in the environment of the stellar particle, an artificial density and smoothing length of the stellar particle are computed. Gas particles inside the smoothing length are considered for the SN process whereas gas particles outside the smoothing length get no mass and energy fractions.

The smoothing length of a stellar particle with SN event is determined by assuming a certain desired number of neighbouring gas particles. We apply $N_\mathrm{ngb} = 40$ neighbouring gas particles. This is the same number of neighbours as used for the computation of densities, pressures and other hydrodynamic variables. The smoothing length h_star is determined by using a similar procedure as the determination of gas smoothing lengths. The density for a stellar particle is determined according to

$$\rho_* = \sum_{i=1}^{N} m_i W(|\vec{r}_{i,*}|, h) \,, \tag{3.35}$$

where $W(|\vec{r}_{i,*}|, h)$ is the smoothing kernel specified in Equation (3.7). The sum is calculated over all neighbouring gas particles within the smoothing length h_star of the stellar particle. m_i is the mass of the i-th gas neighbour and $\vec{r}_{i,*}$ the vector from the stellar particle to the gas particle i.

The thermal energy ΔE_i (SN) and mass ΔM_i input to the i-th gas particle are

$$E_{\rm SN} = \sum_{i=1}^{N} \Delta E_i = \frac{E_{\rm SN} \sum_{i=1}^{N} m_i W(|\vec{r}_{i,*}|, h)}{\rho_*} \,, \tag{3.36}$$

$$\Rightarrow \Delta E_i = \frac{E_{\rm SN} m_i W(|\vec{r}_{i,*}|, h)}{\rho_*} \,, \tag{3.37}$$

$$M_{\rm SN} = \sum_{i=1}^{N} \Delta M_i = \frac{M_{\rm SN} \sum_{i=1}^{N} m_i W(|\vec{r}_{i,*}|, h)}{\rho_*} \,, \tag{3.38}$$

$$\Rightarrow \Delta M_i = \frac{M_{\rm SN} m_i W(|\vec{r}_{i,*}|, h)}{\rho_*} \,, \tag{3.39}$$

$$M_{\rm SN} = \sum_{m=8}^{40} f(m) m \mathrm{M}_\odot \,. \tag{3.40}$$

$M_{\rm SN}$ is the total mass of stars between $8\ \mathrm{M}_\odot$ and $40\ \mathrm{M}_\odot$, which is determined by using the above IMF and we treat it as the total ejection mass of a stellar particle. The total energy output of the SN explosion is assumed to be $E_{\rm SN} = 10^{49}\ \mathrm{erg/M}_\odot = 10^{42}\ \mathrm{J/M}_\odot$. The feedback event is computed $\tau = 10^6\ \mathrm{yr}$ after the star formation, which is approximately the lifetime of a star with $M_{\rm s} = 40\ \mathrm{M}_\odot$. The thermal energy input of a gas particle is implemented by augmenting the pressure and entropy of the gas particle with mass m_i and density ρ_i with

$$\Delta p_i = \frac{\Delta E_i \rho_i (\gamma - 1)}{m_i} \,, \tag{3.41}$$

$$\Delta S_i = \frac{\Delta E_i \rho_i^{1-\gamma} (\gamma - 1)}{m_i} \,. \tag{3.42}$$

In regions with extremly high densities, Katz (1992) showed that the feedback energy from the SN events is radiated away very quickly. So, if the cooling mechanism is not modified, no significant influence of the feedback is expected.

One way to circumvent this problem is to alter the density value (Thacker, Couchman 2000), since the computation of the cooling rate for a particle is based on its density value ρ_i. Hence, a modification of ρ_i corresponds to a physical modification of the cooling mechanism.

Another possiblity for solving this problem is simply turning off the cooling for gas particles, which are subject to SN energy feedback (Gerritsen 1997) for a certain relaxation time.

For our work, we adopt the second method and turn off cooling for gas particles. Thereby, for each gas particle experiencing stellar feedback, the cooling mechanism is turned off for $2 \times 10^7\ \mathrm{yr}$. After this time span, cooling is turned on again.

3.3.3 The external (gravitational) potential

The application of an external gravitational potential is motivated by the idea that with the external potential, a density wave with a grand-design spiral structure can be created in the disc.

In the presence of an external potential, each particle experiences an additional gravitational force. This external force and its resulting acceleration of a particle are characterized by

$$\vec{F}_{\mathrm{grav,ext}} = m\vec{a}_{\mathrm{grav,ext}} = -m\vec{\nabla}\Phi_{\mathrm{ext}} \ , \tag{3.43}$$

$$\vec{a}_{\mathrm{grav,ext}} = -\vec{\nabla}\Phi_{\mathrm{ext}} \ . \tag{3.44}$$

We apply the external potential (Dobbs et al. 2006, Cox & Gomez 2002) specified in Equations (3.45) - (3.49). This analytical expression was derived by Cox & Gomez (2002) for the first time to describe the shape of a spiral gravitational potential in galaxies. It can be easily adopted in any galaxy model.

$$\Phi_{\mathrm{ext}}(r,\theta,t) = -4\pi \mathrm{G} H \rho_0 \exp\left(-\frac{r-r_0}{R_{\mathrm{s}}}\right) \sum_{n=1}^{3} \frac{C_n}{K_n D_n} \cos(n\gamma) \ , \tag{3.45}$$

$$\gamma(r,\theta,t) = N\left[-\theta + \Omega_{\mathrm{p}} t - \frac{\ln(r/r_0)}{\tan(\alpha)}\right] \ , \tag{3.46}$$

$$K_n(r) = \frac{nN}{r\sin(\alpha)} \ , \tag{3.47}$$

$$D_n(r) = \frac{1 + K_n H + 0.3(K_n H)^2}{1 + 0.3 K_n H} \ , \tag{3.48}$$

$$C_1 = \frac{8}{3\pi} \ , C_2 = \frac{1}{2} \ , C_3 = \frac{8}{15\pi} \ . \tag{3.49}$$

N is the number of arms. $r_0 = 8$ kpc, $R_{\mathrm{s}} = 7$ kpc and $H = 0.18$ kpc are radial parameters. α is the pitch angle and ρ_0 the amplitude of the perturbation. Ω_{p} is the pattern speed. The external potential varies with time and leads to a rotating spiral structure. It is written in cylindrical coordinates r and θ. The transformation between cartesian (x, y, z) and cylindrical (θ, r, z) coordinates is

$$\begin{pmatrix} x \\ y \\ z \end{pmatrix} = \begin{pmatrix} r\cos\theta \\ r\sin\theta \\ z \end{pmatrix} \ , \ r = \sqrt{x^2+y^2} \ , \ \theta = \arctan\frac{y}{x} \ , \ z = z \ . \tag{3.50}$$

The minus sign in front of θ in Equation (3.46) assures the presence of trailing spiral arms in a galactic disc that rotates anti-clockwise. This is the case in our model.

An example of the applied external potential is shown in Figure 3.2 for $\alpha = 20°$, $N = 2$ and $\rho_0 = 1$ atom cm^{-3}. As can be seen there, the chosen parameters define a clear grand-design spiral structure.

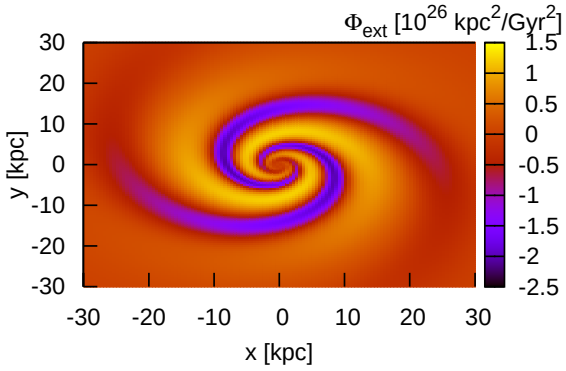

Figure 3.2: General shape and dimension of external gravitational potentials, which are applied in this work.

Due to the cylindrical description of the external potential, the easiest way to determine the external acceleration is to calculate the gradient of Φ_{ext} in cylindrical coordinates. The gradient of the external potential in cylindrical coordinates is

$$\vec{\nabla}\Phi_{\text{ext}} = \frac{\partial\Phi_{\text{ext}}}{\partial r}\vec{e}_r + \frac{1}{r}\frac{\partial\Phi_{\text{ext}}}{\partial\theta}\vec{e}_\theta + \frac{\partial\Phi_{\text{ext}}}{\partial z}\vec{e}_z\,, \tag{3.51}$$

$$\vec{e}_r = \begin{pmatrix}\cos\theta\\ \sin\theta\\ 0\end{pmatrix} = \begin{pmatrix}\frac{x}{r}\\ \frac{y}{r}\\ 0\end{pmatrix}\,,\ \vec{e}_\theta = \begin{pmatrix}-\sin\theta\\ \cos\theta\\ 0\end{pmatrix} = \begin{pmatrix}-\frac{y}{r}\\ \frac{x}{r}\\ 0\end{pmatrix}\,,\ \vec{e}_z = \begin{pmatrix}0\\ 0\\ 1\end{pmatrix}\,. \tag{3.52}$$

The three derivatives of Φ_{ext} are

$$\frac{\partial}{\partial\theta}\Phi_{\text{ext}} = -4\pi\text{G}H\rho_0\exp\left(-\frac{r-r_0}{R_\text{s}}\right)\sum_{n=1}^{3}\frac{nNC_n}{K_nD_n}\sin(n\gamma)\,, \tag{3.53}$$

$$\begin{aligned}\frac{\partial}{\partial r}\Phi_{\text{ext}} &= \frac{4\pi\text{G}H\rho_0}{R_\text{s}}\exp\left(-\frac{r-r_0}{R_\text{s}}\right)\sum_{n=1}^{3}\frac{C_n}{K_nD_n}\cos(n\gamma)\\ &-4\pi\text{G}H\rho_0\exp\left(-\frac{r-r_0}{R_\text{s}}\right)\left(\sum_{n=1}^{3}\frac{-C_n(K_nD_n)'}{K_n^2D_n^2}\cos(n\gamma) - \frac{nC_n\gamma'}{K_nD_n}\sin(n\gamma)\right)\,,\end{aligned} \tag{3.54}$$

$$\frac{\partial}{\partial z}\Phi_{\text{ext}} = 0\,, \tag{3.55}$$

with

$$(K_n D_n)' = K_n' D_n + K_n D_n' \,, \tag{3.56}$$

$$K_n' = \frac{\partial K_n}{\partial r} = -\frac{nN}{r^2 \sin(\alpha)} \,, \tag{3.57}$$

$$D_n' = \frac{\partial D_n}{\partial r} = \frac{(1+0.3K_nH)(HK_n' + 0.6K_nH^2K_n') - (1+K_nH+0.3(K_nH)^2)0.3HK_n'}{(1+0.3K_nH)^2} \,, \tag{3.58}$$

$$\gamma' = \frac{\partial \gamma}{\partial r} = -\frac{N}{r\tan(\alpha)} \,. \tag{3.59}$$

With the derivatives of Φ_{ext} given, the gradient of Φ_{ext} (Equation 3.51) can be calculated. Finally, the resulting total gravitational acceleration $\vec{a}_{\text{grav,tot}}$ is the sum of the normal gravitational acceleration $\vec{a}_{\text{grav}}$ and the acceleration due to the external potential $\vec{a}_{\text{grav,ext}}$,

$$\vec{a}_{\text{grav,tot}} = \vec{a}_{\text{grav}} + \vec{a}_{\text{grav,ext}} = \vec{a}_{\text{grav}} - \vec{\nabla}\Phi_{\text{ext}} \,. \tag{3.60}$$

3.3.4 Gravitational interaction with a perturber

Motivated by previous results of gravitational interactions of a disc galaxy with a perturber, we also study large-scale structures of disc galaxies with a fly-by event. Unlike previous authors, the orbit for the perturbers motion is not fixed (e.g. parabolic). Only a certain initial position and velocity of a perturber with a certain mass is used as initial configuration.

3.4 Galaxy model and resolution levels

At time $t = 0$, simulations start with a certain galaxy model. We concentrate our studies on a model for disc galaxies, which is similar to the composition of the Milky Way. The parameters for this model are described in this Section.

The initial galaxy model is composed of a spherical dark matter halo and an initially exponential disc composed of collisionless disc particles and gas particles (SPH). For this model, a halo concentration of $c = 5$, a spin parameter of $\lambda = 0.05$ and the Hubble constant $\mathrm{H}_0 = 70\,\mathrm{km\ s^{-1}\ Mpc^{-1}}$ are used. Beside these parameters, the following parameters are relevant for the initial model:

- rotational velocity v_{200} at the virial radius R_{200}[1] where the overdensity above the cosmic

[1]The virial radius R_{200} is used to refer to the radius of a sphere, centered on a galaxy (or a galaxy cluster), within which the average density is greater, by a factor of 200, than the critical density $\rho_{cr} = 3\mathrm{H_0}^2/(8\pi\mathrm{G})$.

average is 200,

- fraction of total halo mass in the disc $m_{\rm d}$,
- gas fraction in the disc mass $f_{\rm g}$,
- radial disc scale length $R_{\rm d}$ where the stellar surface density drops by e^{-1}.

In this model, no bulge is included. The values of the parameters are listed in Table 3.2.

v_{200} [km/s]	R_{200} [kpc]	M_{200} [10^{10} $\mathrm{M}_\odot$]	$m_{\rm d}$	$f_{\rm g}$	$R_{\rm d}$ [kpc]
160	228.57	136.0	0.05	0.2	4.51

Table 3.2: Parameter values of our studied galaxy model.

M_{200} is the total mass of the configuration within the virial radius R_{200}. For comparison, the Milky Way has $v_{200} = 160$ km/s, $R_{200} \approx 230$ kpc, $m_{\rm d} \approx 0.06$, $f_{\rm g} \approx 0.07$ and additionally a bulge with approximately 20% of the total mass inside R_{200}.

The dynamics of the dark matter (DM) halo is described by DM particles. The gas particles in the disc represent gas and molecular clouds. Beside the gas particles, collisionless particles are also present in the disc. These particles are divided into two different types of collisionless particles. The 'disc particles' are the only collisionless particles in the initial galaxy configuration. They represent the collisionless components in the disc such as old stars or small bodies, which do not interact with their vicinity via e.g. supernovae etc. During the simulation, 'stellar particles' can additionally be formed, which represent newly formed stellar clusters that interact with their vicinity via supernova explosions.

The number of each particle type also determines their resolutions. For all simulations, a ratio between the total numbers of each particle type $N_{\rm g} : N_{\rm h} : N_{\rm d} = 5 : 3 : 2$ is chosen, with $N_{\rm g}$ being the total number of gas particles, $N_{\rm h}$ the total number of halo particles and $N_{\rm d}$ the number of disc particles.

By knowing all parameters and the number of particles, the initial gas particle mass $M_{\rm g}$ can be determined to

$$M_{200} = \frac{v_{200}^3}{10 \mathrm{G H}_0} \,, \tag{3.61}$$

$$M_{\rm g} = \frac{f_{\rm g} m_{\rm d} M_{200}}{N_{\rm g}} \,. \tag{3.62}$$

The product $m_{\rm d} M_{200}$ is the total disc mass inside R_{200} determined by the disc mass fraction $m_{\rm d}$. The total gaseous mass in the disc inside R_{200} is $f_{\rm g} m_{\rm d} M_{200}$. Finally, the initial mass of each gas

particle $M_{\rm g}$ is the total gaseous mass in the disc divided by the number of gas particles $N_{\rm g}$. The initial mass of the disc particles $M_{\rm d}$ is determined by first calculating the total mass of all disc particles and then dividing it by the number of disc particles.

$$M_{\rm d} = \frac{(1 - f_{\rm g}) m_{\rm d} M_{200}}{N_{\rm d}} \,. \tag{3.63}$$

The dark matter particles in the halo have masses according to

$$M_{\rm h} = \frac{(1 - m_{\rm d}) M_{200}}{N_{\rm h}} \,. \tag{3.64}$$

The initial particle masses M_i for our model at different resolution levels are listed in Table 3.3. According to the different resolution levels, the gravitational softening lengths ϵ_i for the different

Resolution level	$N_{\rm tot}$ $[10^5]$	$M_{\rm g}$ $[10^4\,{\rm M}_\odot]$	$M_{\rm d}$ $[10^4\,{\rm M}_\odot]$	$M_{\rm h}$ $[10^4\,{\rm M}_\odot]$
R1	1	27.05	270.53	4283.32
R4	4	6.75	67.63	1070.83
R8	8	3.38	33.82	535.42

Table 3.3: Different resolution levels with the total numbers of particles $N_{\rm tot}$ and their corresponding initial masses for gas ($M_{\rm g}$), disc ($M_{\rm d}$) and halo particles ($M_{\rm h}$).

particle types must also be adjusted. In Table 3.4, we summarize the softening lengths used for the simulations. In addition, the relaxation time $\tau_{\rm rel}$ and critical density for star formation $\rho_{\rm crit}$ are listed. The relaxation time is the phase at the beginning of the simulation when no star formation

Resolution level	$\epsilon_{\rm g}$ [kpc]	$\epsilon_{\rm d}$ [kpc]	$\epsilon_{\rm h}$ [kpc]	$\epsilon_{\rm s}$ [kpc]	$\tau_{\rm rel}$ $[10^9$ yr]	$\rho_{\rm crit}$ $[{\rm M}_\odot/{\rm kpc}^3]$
R1	0.4	0.4	0.8	0.4	1	10^8
R4	0.2	0.2	0.4	0.2	0.6	10^9
R8	0.1	0.1	0.2	0.1	0.6	10^{10}

Table 3.4: Resolution levels R1, R4 and R8 with their corresponding gravitational softening lengths for different particle types, relaxation time and typical critical densities for star formation. $\epsilon_{\rm g}$ is applied to gas particles, $\epsilon_{\rm d}$ to disc particles, $\epsilon_{\rm h}$ to halo particles and $\epsilon_{\rm s}$ to stellar particles.

is active. Due to radiative cooling, the gas phase first has to settle down in a thin disc. This flattening of the disc produces turbulent motions in the disc, which have to disappear before star formation can be switched on. The critical densities for star formation shown in Table 3.4 are used for isolated galaxies in Section 3.5. Depending on the features that are studied in the subsequent Sections, their values are vary slightly.

Due to the small fraction $f_{\rm g} = 0.2$ of gas, the structure and dynamics of our chosen model disc is mainly given by the collisionless part of the disc, viz the 'disc particles'. The gas components are however expected to follow the main dynamics of the disc particles. Due to their dissipative nature, we also expect that the spiral features are more pronounced in the gas phase. Therefore, we will focus our study on the gaseous density distributions.

3.5 Study of isolated galaxies

In this Section, the large-scale gaseous structure of an isolated galaxy in the absence of external perturbations is studied in detail.

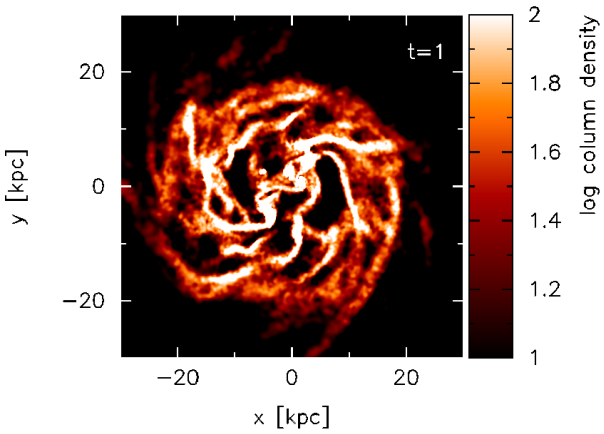

Figure 3.3: Face-on view of the galaxy at resolution level R1 and time $t = 1$ Gyr. The density distribution of gas is shown in logarithmic scale and internal unit 10^5 $\mathrm{M}_\odot/\mathrm{kpc}^3$.

For all face-on plots, the density distribution is shown in logarithmic scale. The densities shown in the plots are described in internal units, which is 10^5 $\mathrm{M}_\odot/\mathrm{kpc}^3$. Time values in the plots are given in Gyr. Figure 3.3 shows a face-on view of the chosen model at resolution level R1 and time $t = 1$ Gyr. The star formation process is turned on for R1 at time $t = 1$ Gyr. The reason for the suppression of star formation before $t = 1$ Gyr is that in the beginning phase, gaseous particles settle down in a thin disc due to radiative cooling. Star formation should therefore be turned on after the gas has relaxed until no large turbulence motions are left.

The galactic disc shows many flocculent spiral arms indicating the dissipative nature of the gas.

3.5.1 Large-scale structure

The evolution of a disc galaxy without external perturbations and stellar feedback is shown in Figure 3.4. The plots a) and c) show the density distributions of the gas. In b) and d), new stellar

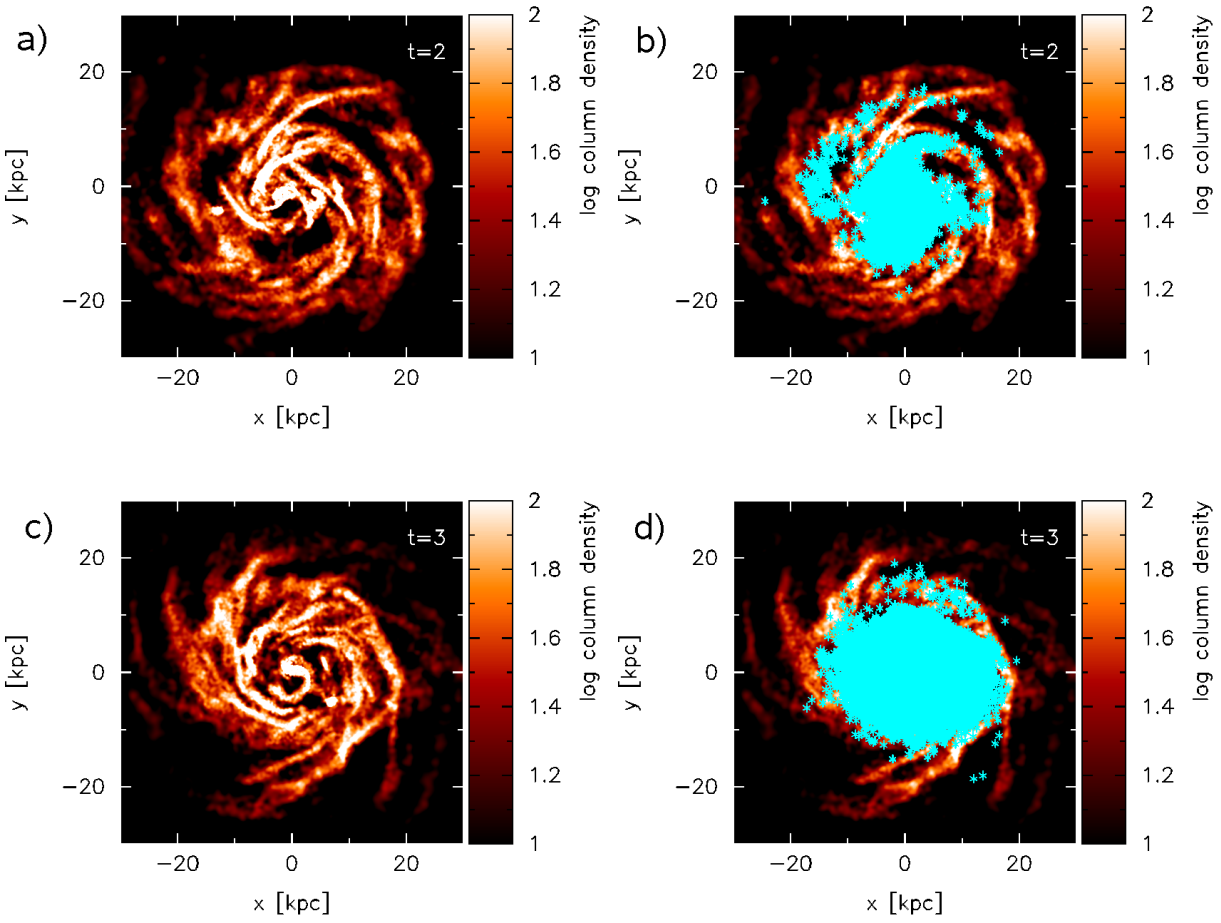

Figure 3.4: Density distribution of gas and newly formed stellar particles (turquoise stars) at $t = 2$ Gyr (a) and b)) and $t = 3$ Gyr (c) and d)) at resolution level R1, without stellar feedback. The critical density for star formation is 10^8 $\mathrm{M}_\odot/\mathrm{kpc}^3$.

particles (turquoise stars) are additionally shown. Snapshots at times $t = 2$ Gyr and $t = 3$ Gyr are shown. In all following plots only stellar particles formed within 0.1 Gyr before the given point in time are shown in order to prevent a large cumulation of stellar particles in the plots.

The regions with high gaseous densities mark well the (transient) flocculent spiral structure of the disc. Without any stellar feedback, a flocculent spiral structure is present in the gas disc, which originates only from the dissipative nature and differential rotation of the gas component.

Due to the decreasing surface mass density in the disc, higher densities can be reached more easily by centered regions. New stellar particles are mainly concentrated in a region around the galactic center within a certain radius. Hence, by diminishing the critical density for star formation, the star formation region can be enlarged and vice versa, a higher critical density for star formation leads to a smaller star formation region in the center.

In Figure 3.5, the same snapshots as shown in Figure 3.4 with and without new stellar particles are shown for the case of stellar feedback switched on. The influence of stellar feedback on the

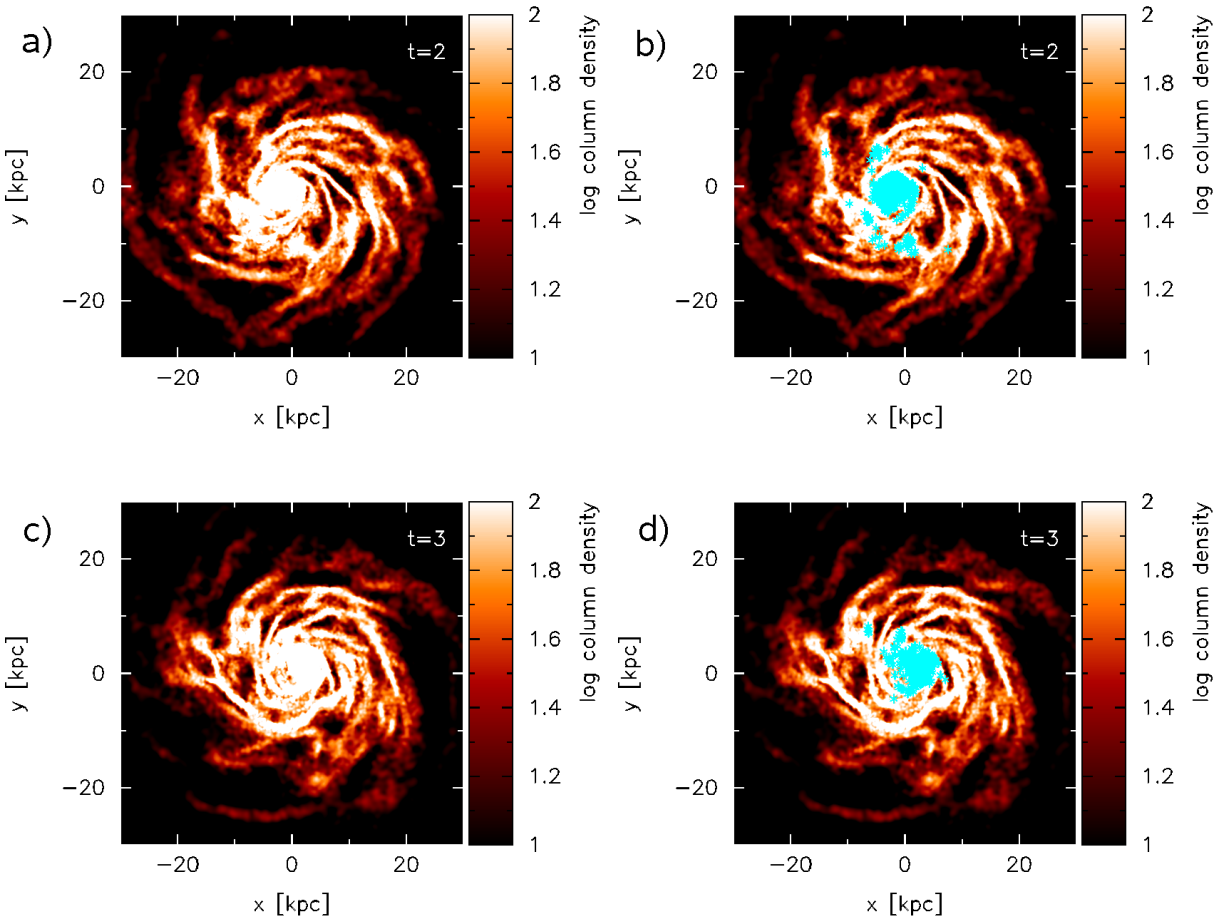

Figure 3.5: Density distribution of gas at $t = 2$ Gyr (a) and b)) and $t = 3$ Gyr (c) and d)) with stellar feedback. In b) and d), new stellar particles (turquoise stars) are plotted in addition to the gas density distribution. The critical density for star formation is 10^8 $M_\odot/\mathrm{kpc}^3$.

development of a galaxy was studied by Gerola & Seiden (1978) with a purely stochastic ansatz. In our simulation, a stochastic component is also present, which lies in the star formation process

(Equation (3.26)). Hence, there is an analogy in the treatment of the galactic evolution. The plots in Figure 3.5 show that the gas disc still possesses irregular flocculent structures. The large-scale structure evolution of the galaxy with stellar feedback is similar to that without stellar feedback. However, it is also remarkable that the densities are significantly larger than those shown in Figure 3.4. A closer look onto the number of new stellar particles (b) and d) of Figure 3.5) shows a much smaller number of new stellar particles than in Figure 3.4. Both the higher gas densities and the smaller number of new stellar particles are consequences of the stellar feedback mechanism, which prevents the gas from forming stellar particles although its density is high enough. Due to the absence of cooling for gas particles experiencing SNe, these gas particles have large entropies, which cannot be reduced via cooling. The large entropies and with them also the large pressures produce strong hydrodynamic decelerations of the gas particles precluding them from fullfilling all star formation criteria.

3.5.2 Star formation rate

In Figure 3.6, the total masses of stellar particles for the resolution level R1 are plotted against the simulation time without a) and with b) stellar feedback. The inclination of the curve can be

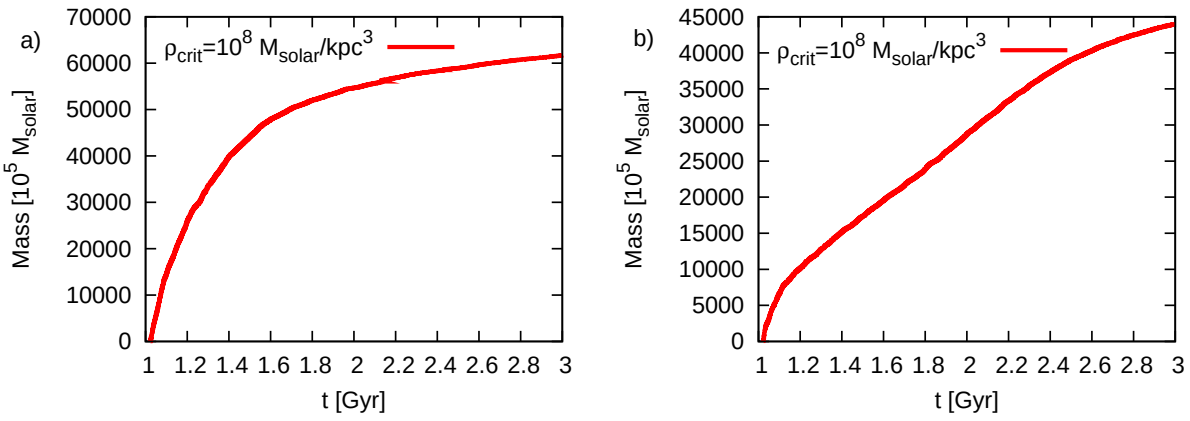

Figure 3.6: Total mass of new stellar particles without a) and with b) stellar feedback. The critical density for star formation is $10^8\ \mathrm{M}_\odot/\mathrm{kpc}^3$.

interpreted as the star formation rate. In panel a), a large number of stellar particles is created in the beginning phase after star formation is activated and the increase of total new stellar mass is very fast. The curve subsequently flattens corresponding to a decreasing star formation rate (SFR). The decrease of SFR is caused by the diminution of gas content in the galaxy due to star formation.

Compared to panel a) with initial strong star formation bursts, panel b) shows a much flatter curve in the beginning phase and a significantly smaller total mass of stellar particles. In a later phase, when the curve in a) flattens significantly, the curve in b) still shows an active star formation process indicated by the non-vanishing inclination (=SFR) of the curve. This is due to the much slower consumption of gas after stellar feedback has been turned on. Consequently, the star formation process can take place over a larger time span.

3.5.3 Resolution variation

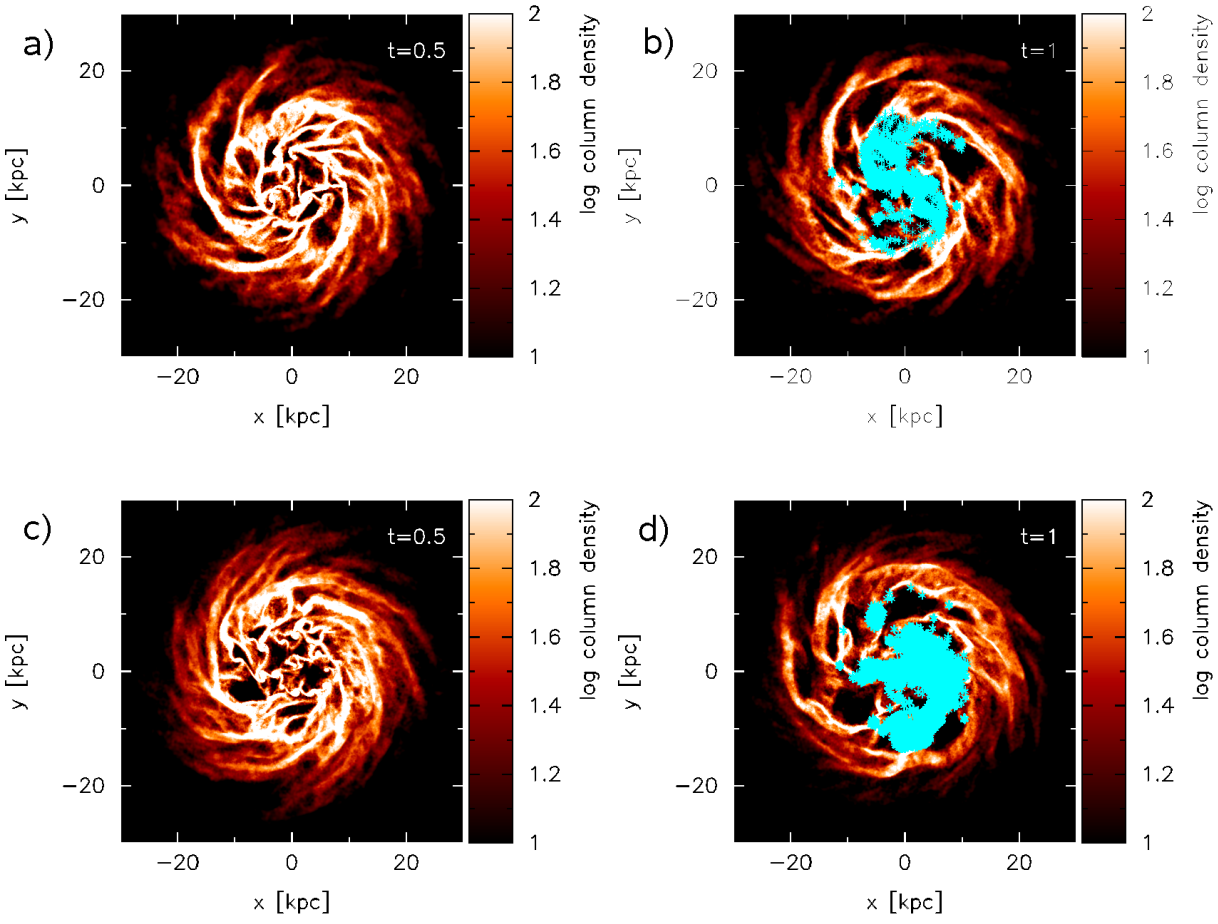

Figure 3.7: Density distribution of gas and new stellar particles (turquoise stars) at time steps $t = 0.5$ Gyr (a), c)) and $t = 1$ Gyr (b), d)), for resolution levels R4 (a) and b)) and R8 (c) and d)). Stellar feedback is deactivated. For R4, the critical density for star formation is 10^9 $M_\odot/kpc^3$. For R8, it is 10^{10} $M_\odot/kpc^3$.

Figure 3.7 shows for $t = 0.5$ Gyr (a) and c)) only the gas density distribution whereas for $t = 1$ Gyr (b) and d)), new stellar particles (turquoise stars) are also plotted. The higher the resolution level is, the more structure can be resolved. The flocculent spiral arms are clearly thinner and smoother. In addition, the density contrast between the arm and interarm regions is less for higher resolution levels, which resembles observed ratios of arm and interarm gaseous densities in a better way.

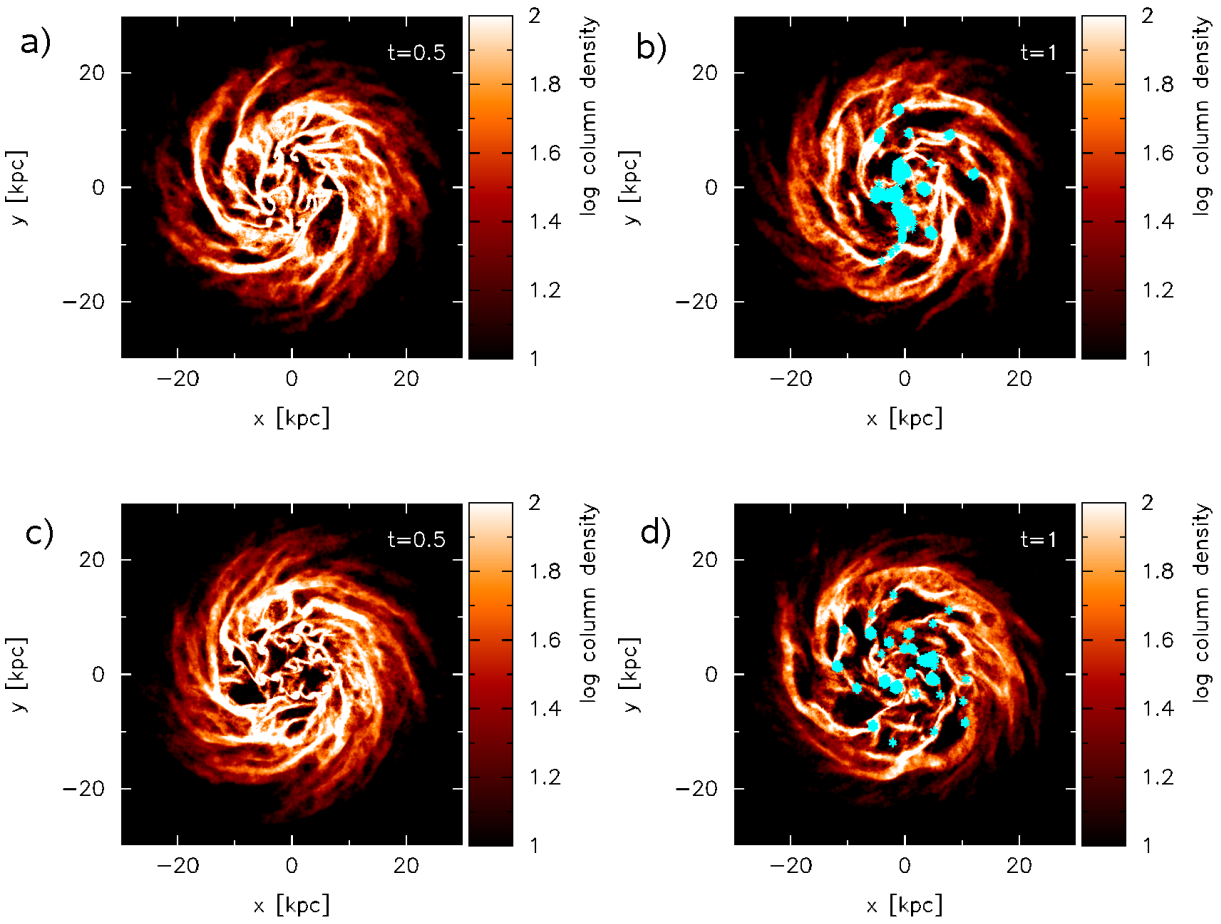

Figure 3.8: Density distribution of gas and new stellar particles (turquoise stars) at $t = 0.5$ Gyr (a), c)) and $t = 1$ Gyr (b), d)), for resolution levels R4 (a) and b)) and R8 (c) and d)). Stellar feedback is switched on. For R4, the critical density for star formation is 10^9 $\mathrm{M}_\odot/\mathrm{kpc}^3$. For R8, it is 10^{10} $\mathrm{M}_\odot/\mathrm{kpc}^3$.

Figure 3.8 shows the gas density distribution and new stellar particles (turquoise stars) at time $t = 0.5$ Gyr (a), c)) and $t = 1$ Gyr (b), d)). The resolution levels are R4 for a), b) and R8 for c), d). Stellar feedback is activated. Compared to the evolution without stellar feedback, the densities

of gas especially in the central regions are again larger for resolution levels R4 and R8. However, differences between the two cases without and with stellar feedback are smaller than those for resolution level R1. The smaller difference between the cases at higher resolution levels are due to the larger numbers of particles at higher resolution levels and consequently smaller regions, which experience any effects from the SNe.

Due to its larger total number of particles and therefore longer simulation time, resolution level R8 can only be simulated until $t \sim 1$ Gyr. In the subsequent simulations, a minimum evolution time of 3 Gyr is necessary for an adequate description of the time evolutions. Hence, we will restrict simulations to the levels R1 and R4.

3.6 Galaxy-perturber interaction

3.6.1 Simulation models

To study the galaxy - perturber interaction, simulations with various distances, initial velocities and masses of a punctual perturber passing a disc galaxy are performed. The configuration at time $t = 0$ for model d80_200_50_1 is shown in Figure 3.9 . The first number of the model name

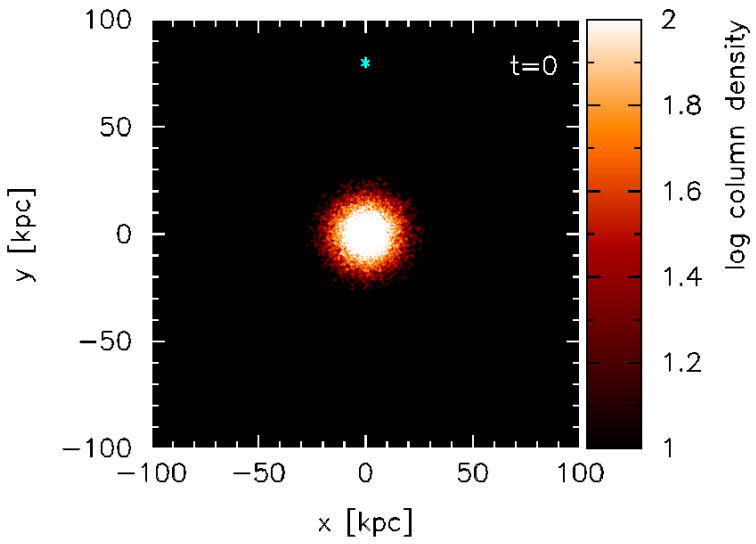

Figure 3.9: Configuration at time $t = 0$ for model d80_200_50_1 with the perturber (turquoise star) starting at position $(0|80|0)$ kpc.

specifies the distance of the perturber to the galaxy at time $t = 0$. The following two numbers

specify the negative values of the initial velocities of the perturber and the last number specifies its mass in units of the total disc mass of the galaxy. E.g. in model d80_200_50_1, the perturber with a mass equal to the total disc mass of the galaxy starts at position $(0|80|0)$ kpc with the velocity $(-200|-50|0)$ kpc/Gyr (see also Figure 3.9). The studied ranges are

- initial distance of perturber to the galaxy: [80, 150] kpc,
- mass of perturber: [0.25, 5] $\times$ total disc mass, which is 6.8×10^{10} $\mathrm{M}_{\odot}$ in our model,
- initial velocities: $v_x = [0, -150]$ kpc/Gyr and $v_y = [-100, -200]$ kpc/Gyr.

Table 3.5 shows a small repertory of the events studied.

Modelname	deactivation time [Gyr]
d80_200_0_1	1.1
d80_200_0_3	1.1
d80_200_50_1	1.1
d100_200_0_5	1.1
d100_200_150_025	0.7
d100_200_150_1	1.0
d150_200_150_1	1.4
d150_200_150_2	1.2
d150_200_150_5	1.2

Table 3.5: Sample of different studied galaxy-perturber interaction models with corresponding deactivation times of the perturber.

In the simulations, an additional mechanism is also included, which deactivates the perturber after an interacting time span (also shown in Table 3.5), in order to minimize simulation time. Physically, the gravitational effect of a passing perturber decreases with increasing distance. In the case of considerably small gravitational effect of the perturber, it can be neglected. This is realized numerically by the deactivation of the perturber.

Generally spoken, three different types of results can be identified, which are

- No spiral structure is created since the effect of the perturber is too small, e. g. too large distance to the galaxy and / or too small mass of the perturber.
- The circular form of the galaxy disc is destroyed since the effect of the perturber is too large, e.g. too small distance to the galaxy and / or the mass of the perturber is too large.
- A large-scale spiral structure is constructed, which however disappears after a time span

In the following we present results of the models d80_200_50_1 and d80_200_0_1, for which the desired large-scale spiral structures can be produced. On the basis of these two examples, the main numerical problems of creating a long-lived large-scale spiral structure by using the gravitational interaction are pointed out and discussed.

3.6.2 Model d80_200_50_1

In Figures 3.10 and 3.11, the results for model d80_200_50_1 at resolution levels R1 and R4 are shown. At time $t = 1.1$ Gyr, the perturber is deactivated.

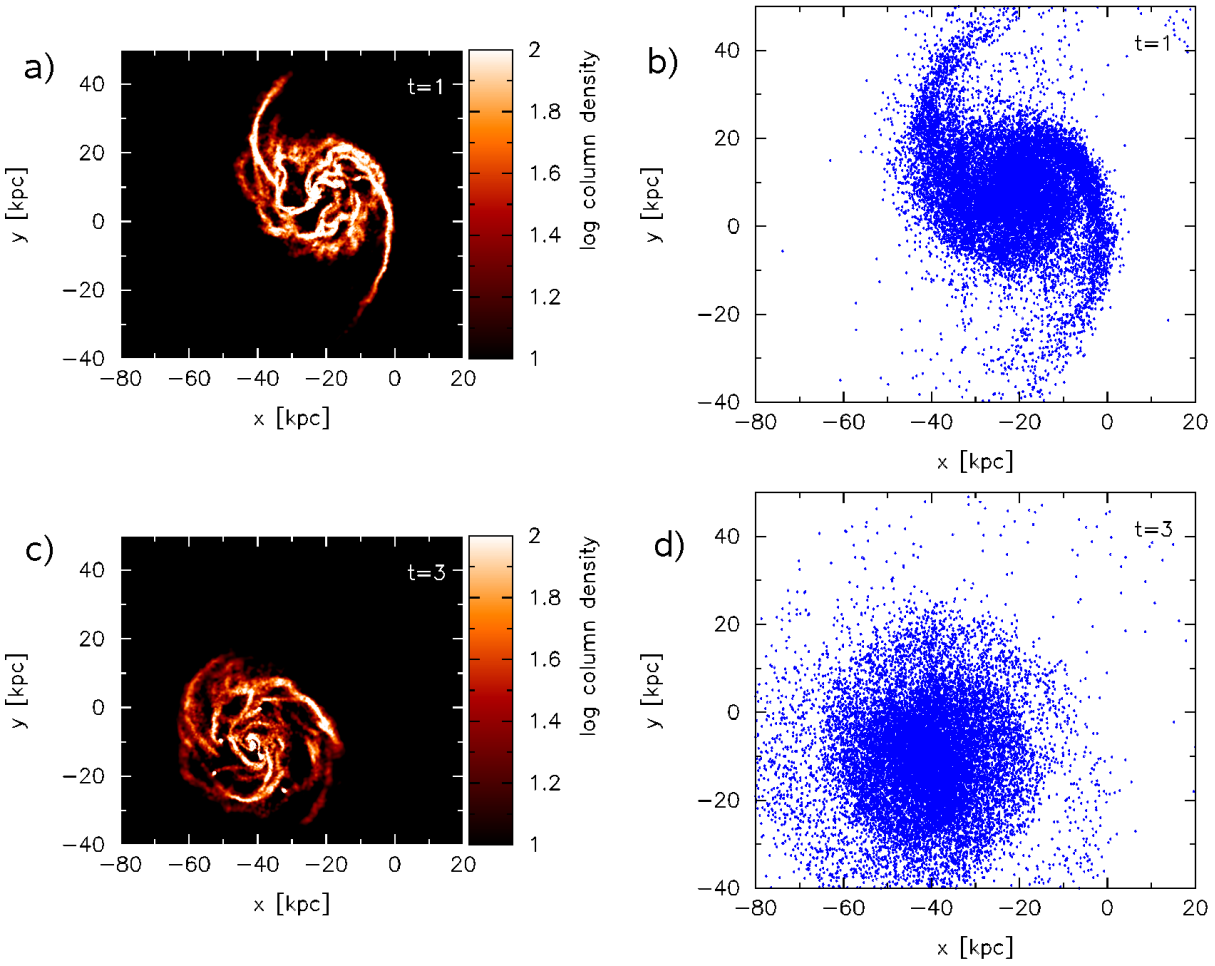

Figure 3.10: Gas density distribution (a) and c)) and collisionless disc particles (b) and d)) at $t = 1$ Gyr (a), b)) and $t = 3$ Gyr (c), d)), for model d80_200_50_1, at resolution level R1. Stellar feedback is deactivated.

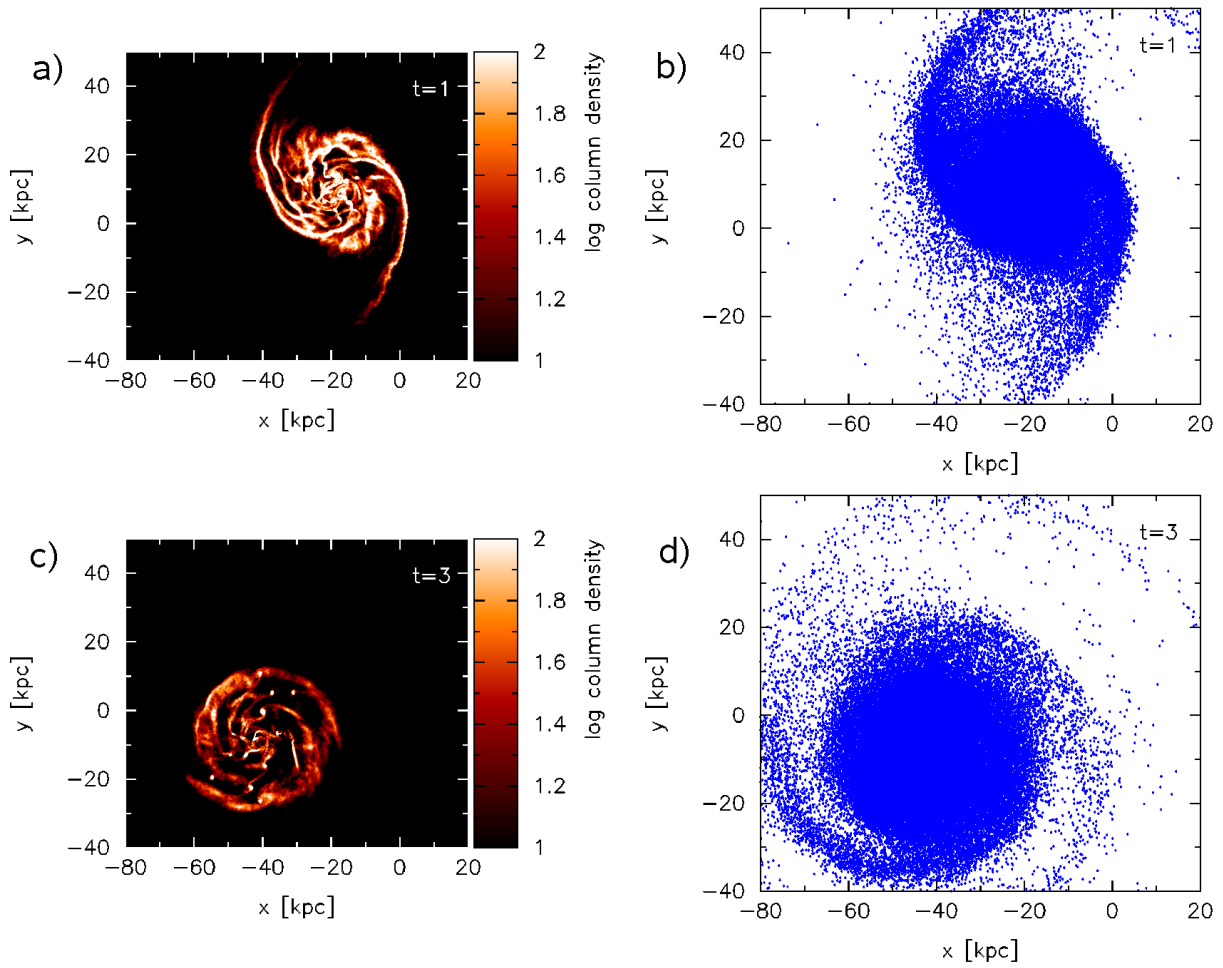

Figure 3.11: Gas density distribution (a) and c)) and collisionless disc particles (b) and d)) at $t = 1$ Gyr (a), b)) and $t = 3$ Gyr (c), d)), for model d80_200_50_1, at resolution level R4. Stellar feedback is deactivated.

At both resolution levels, the perturber is able to produce two pronounced spiral arms in the galaxy via gravitational interaction. Thereby, the arms are visible in the stellar disc (b) and d)) as well as in the gaseous disc (a) and c)). In the gaseous disc, many flocculent spiral arms are also present beside the two long spiral arms. These irregular flocculent arms are caused by randomly produced shock waves in the gaseous disc. After the deactivation of the perturber, the grand-design spiral structure disappears after approximately 2 Gyr for both R1 and R4. Thereby, a clear winding up of the long spiral arms can be found in the plots. The structure of the gaseous disc is more and more redominated by the irregular flocculent spiral arms.

An inclusion of stellar feedback in Figure 3.12 does not affect the large-scale evolution of the galaxy. The reason lies in an insufficient resolution in the gas disc, which only enables star

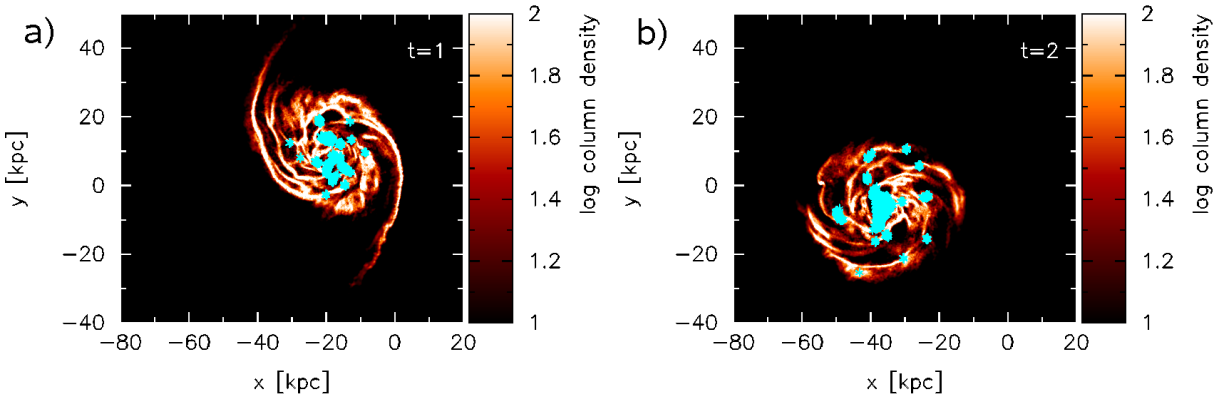

Figure 3.12: Gas density distribution and new stellar particles (turquoise stars) at time steps $t = 1$ Gyr a) and $t = 2$ Gyr b), for model d80_200_50_1, at resolution level R4. Stellar feedback is activated.

formation in the central regions and not in the spiral arms. The extended spiral arms have low gas densities, which do not satisfy star formation criterium (3.24). Hence, stellar feedback only affects the dynamics in the central regions but not in the grand-design spiral arms.

3.6.3 Model d80_200_0_1

In Figures 3.13 and 3.14, the evolution of model d80_200_0_1 at resolution levels R1 and R4 are shown. For this model, the perturber is also deactivated at time $t = 1.1$ Gyr.

In Figure 3.13, the evolution at resolution level R1 is studied up to $t = 4$ Gyr. Again, panel a) shows a combination of flocculent and grand-design spiral structure in the gaseous disc at time when the perturber still has a significant influence on the galaxy. But in the absence of the additional gravitational force, the grand-design spiral structure gets fainter and disappears due to winding up of the arms, while the discs redistribute back to their initial circular outer shape (c) and d)). The structure of the gaseous disc in panel c) is redominated by the irregular flocculent arms.

In Figure 3.14, the winding mechanism can be seen clearly by comparing the pitch angles of the spiral arms at $t = 1.5$ Gyr and 3 Gyr. For both resolution levels, R1 and R4, the time of complete disappearance of the grand-design structure can be estimated to approximately 2 - 3 Gyr.

Since the pattern speed of the spiral structure is dependent on the radius leading to the famous winding-up problem of the spiral arms, which was already discussed in detail by Oort (1962), the

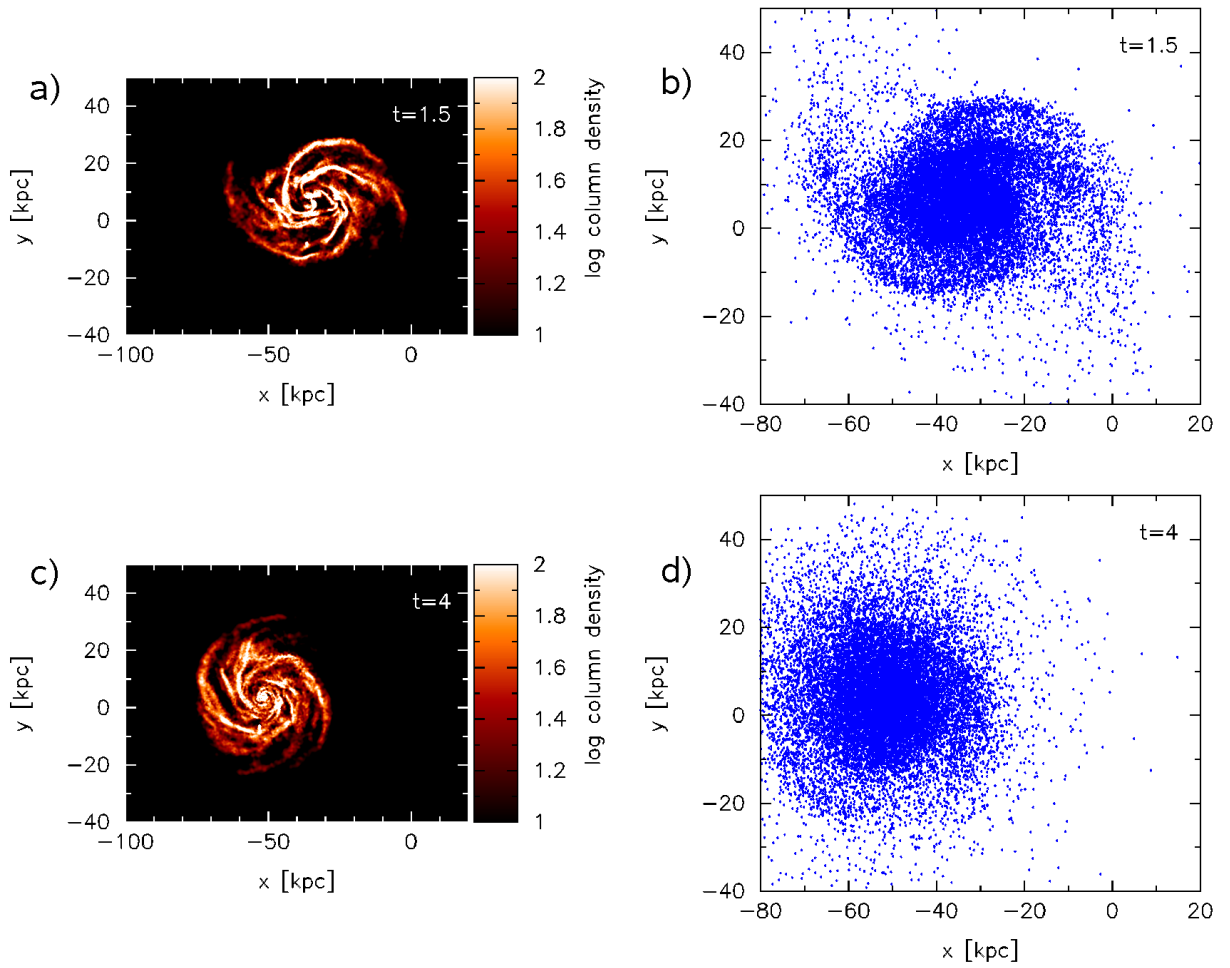

Figure 3.13: Gas density distribution (a) and c)) and collisionless disc particles (b) and d)) at $t = 1$ Gyr (a), b)) and $t = 3$ Gyr (c), d)), for model d80_200_0_1, at resolution level R1. Stellar feedback is deactivated.

numerically realized spiral arms do not represent classical density waves, but rather kinematic density waves or material arms.

Figure 3.14 a) shows that star formation is active again mainly in the central region and not in the grand-design spiral arms. Therefore, a longer persistence of the grand-design spiral arms due to support of stellar feedback cannot be expected. Once again it is remarkable that the grand-design structure stands in strong competition with the flocculent structure automatically generated by the disc itself.

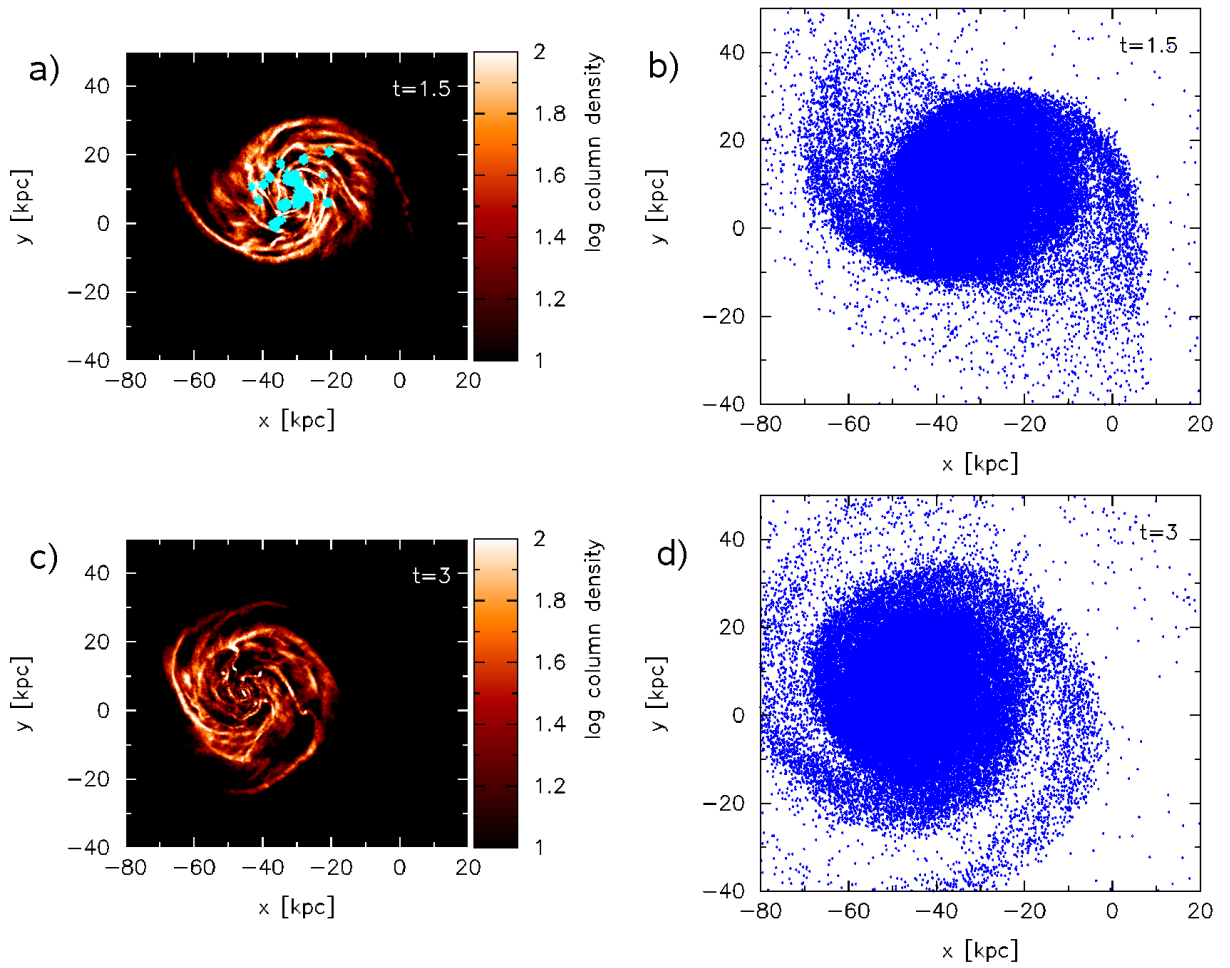

Figure 3.14: Gas density distribution (a) and c)) and collisionless disc particles (b) and d)) at $t = 1$ Gyr (a), b)) and $t = 3$ Gyr (c), d)), for model d80_200_0_1, at resolution level R4. Stellar feedback is deactivated.

3.6.4 Summary of galaxy-perturber interaction

As we have shown with the above examples of results, a grand-design spiral structure can indeed be constructed by the gravitational interaction between a disc galaxy and a passing companion. This has firstly been shown by Toomre & Toomre (1972) and recently by Oh et al. (2008) in a numerical simulation. Contrarily to previous studies, which only treated collisionless particles in the disc, we have studied a realistic disc composed of collisionless particles and dissipative gaseous particles.

Both models d80_200_50_1 and d80_200_0_1 lead to a spiral structure in the stellar as well as in the gaseous disc and show a winding mechanism of the spiral arms. This indicates that the

spiral arms are not the classical density waves firstly proposed by Lin & Shu (1964), but rather material arms. Our first result hence is that due to the interaction with a perturber, only material arms that wind up and disappear can be created. Naturally, these spiral structures are transient. These results have also been found by e.g. Oh et al. (2008).

There is however an additional result in our simulations. By considering the dissipative nature of the gas component, we find that there is a competition between the grand-design spiral structure and the flocculent structure in the disc, which is always won by the flocculent structure. This is due to the fact that the grand-design spiral arms are material arms that disappear automatically.

An inclusion of stellar feedback leads to the same results as in the absence of stellar feedback. Due to low gas densities in the grand-design spiral arms, no stellar particles are formed there and stellar feedback hence only affects the central regions. If the critical density was decreased, star formation could be active in the spiral arms, but the expected star formation in the interarm regions would also increase, which in turn excludes an isolated feedback treatment and therefore also support of the grand-design spiral arms.

It has to be emphasized at this stage of work that the question, whether a density wave can persist in the disc over a long time, cannot be answered with our simulations with a passing perturber. The reason is that a classical density wave still has not been numerically realized so far.

Very recently, Dobbs et al. (2009) presented high-resolution numerical results of gravitational interaction between a M51-like galaxy and a point mass. They showed that the simulations are able to reproduce many observational features of M51 under the influence of its companion galaxy NGC 5195. At the same time, they found out that the spiral arms are not classical density waves but rather ‘spiral density features’, which can also be called material arms. This is in good agreement with our results and also supports our thesis that galaxy-perturber interactions can only produce material arms.

3.7 External potential

By including an external potential with a grand-design spiral structure, a grand-design spiral structure can also be produced in the galactic disc, naturally. Thereby, it is not obvious, whether the produced spiral arms are density waves or so-called kinematic density waves, which stand for material arms.

Hence, the galactic spiral structure is studied for different parameters of the external potential $\Phi_{\rm ext}$. The equation for $\Phi_{\rm ext}$ is shown again in Equation (3.65). Additional details are described in Section 3.3.3.

$$\Phi_{\rm ext}(r,\theta,t) = -4\pi {\rm G} H \rho_0 \exp\left(-\frac{r-r_0}{R_{\rm s}}\right) \sum_{n=1}^{3} \frac{C_n}{K_n D_n} \cos(n\gamma) \; . \tag{3.65}$$

Variations of $R_{\rm s}$, ρ_0 are mainly studied. For the other parameters, we choose if not noted otherwise,

- number of arms $N = 2$,
- parameters for radial variation $r_0 = 8\ {\rm kpc}$, $H = 0.18\ {\rm kpc}$,
- pitch angle $\alpha = 20°$,
- pattern speed $\Omega_{\rm p} = 4\ \pi\ {\rm Gyr}^{-1}$
- time span of activated external potential $\Delta t = 4 \times 10^7\ {\rm yr}$
- critical density for star formation $\rho_{\rm crit} = 5 \times 10^7\ \frac{{\rm M}_\odot}{{\rm kpc}^3}$.

The reproduction of a realistic spiral structure in the disc can be divided into two steps. First, the values for $R_{\rm s}$ and ρ_0, which produce a spiral structure that extends to $r \sim 30\ {\rm kpc}$ while ensuring a certain minimum gas density in the interarm regions, must be found. Gas and molecular clouds are found to be primarily located in spiral arms of galaxies with an arm to interarm ratio $\rho_{\rm arm}/\rho_{\rm interarm}$ varying from a few in the inner regions of some galaxies (e.g. Vogel et al. 1988; Brouillet et al. 1998)) to greater than 20 in the outer regions of the Milky Way (Heyer & Terebey 1998; Digel et al. 1996).

In a second step, $\rho_{\rm crit}$ should be adjusted in order to realize star formation in a range as large as possible in the spiral arms. Naturally, the SFR will increase in the central regions. But it is expected that stellar feedback will prevent a SFR in the center that is too large.

In the following, gaseous density distributions are mainly studied, since we know that the dynamics of the gaseous and collisionless 'disc' particles are similar, with more pronounced flocculent spiral structures in the gaseous component.

3.7.1 Variation of R_s

The radial decrease of the external potential is described by the exponential function $\exp^{r-r_0/R_s}$, which is defined by the parameter R_s. In Figure 3.15, the exponential function for three different values of R_s is shown. $R_s = 7$ kpc is chosen according to Cox & Gomez (2002) and Dehmen & Binney (1998) for a model of the Milky Way. As shown in Figure 3.15, $R_s = 7$ kpc decreases strongly with increasing distance. In order to also study perturbations of smaller radial decreases, $R_s = 17$ kpc and $R_s = 27$ kpc are chosen in addition.

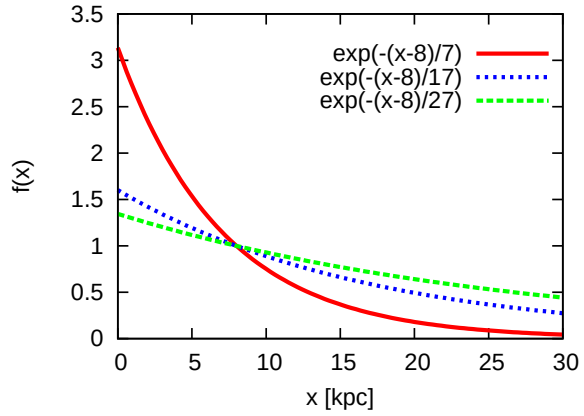

Figure 3.15: Radial dependence of the exponential function included in Φ_{ext} for different R_s.

In Figure 3.16, the density distributions and new stellar particles (turquoise stars) for $R_s = 7$ kpc (a) and b)), $R_s = 17$ kpc (c) and d)), $R_s = 27$ kpc (e) and f)) and $\rho_0 = 4 \times 10^8$ $M_\odot/\text{kpc}^3$ are shown for resolution level R1 and the case of no stellar feedback. At time $t = 1.4$ Gyr, the external potential is switched off. For $R_s = 7$ kpc (a) and b)), the spiral structure is very prominent, whereas in the interarm regions, the gas content is too low compared to typical gas contents in grand-design spiral galaxies. Star formation mainly takes place in the central region. In the spiral arms, little stellar particles are formed. After switching off the external potential, the grand-design structure disappears in a short time and the original flocculent spiral structure redominates the disc.

For $R_s = 17$ kpc (c) and d)), the spiral structure is also very prominent, with clear spiral arms also in the outer regions. This is due to the larger influence of Φ_{ext}. In the interarm regions, the gas content is even lower than for the case $R_s = 7$ kpc. After switching off the external potential, the grand-design structure also disappears in a short time and the original flocculent spiral structure redominates the disc. For $R_s = 17$ kpc, star formation is also dominant in the central regions.

For $R_s = 27$ kpc (e) and f)), the evolution of the galaxy is similar to the case $R_s = 17$ kpc.

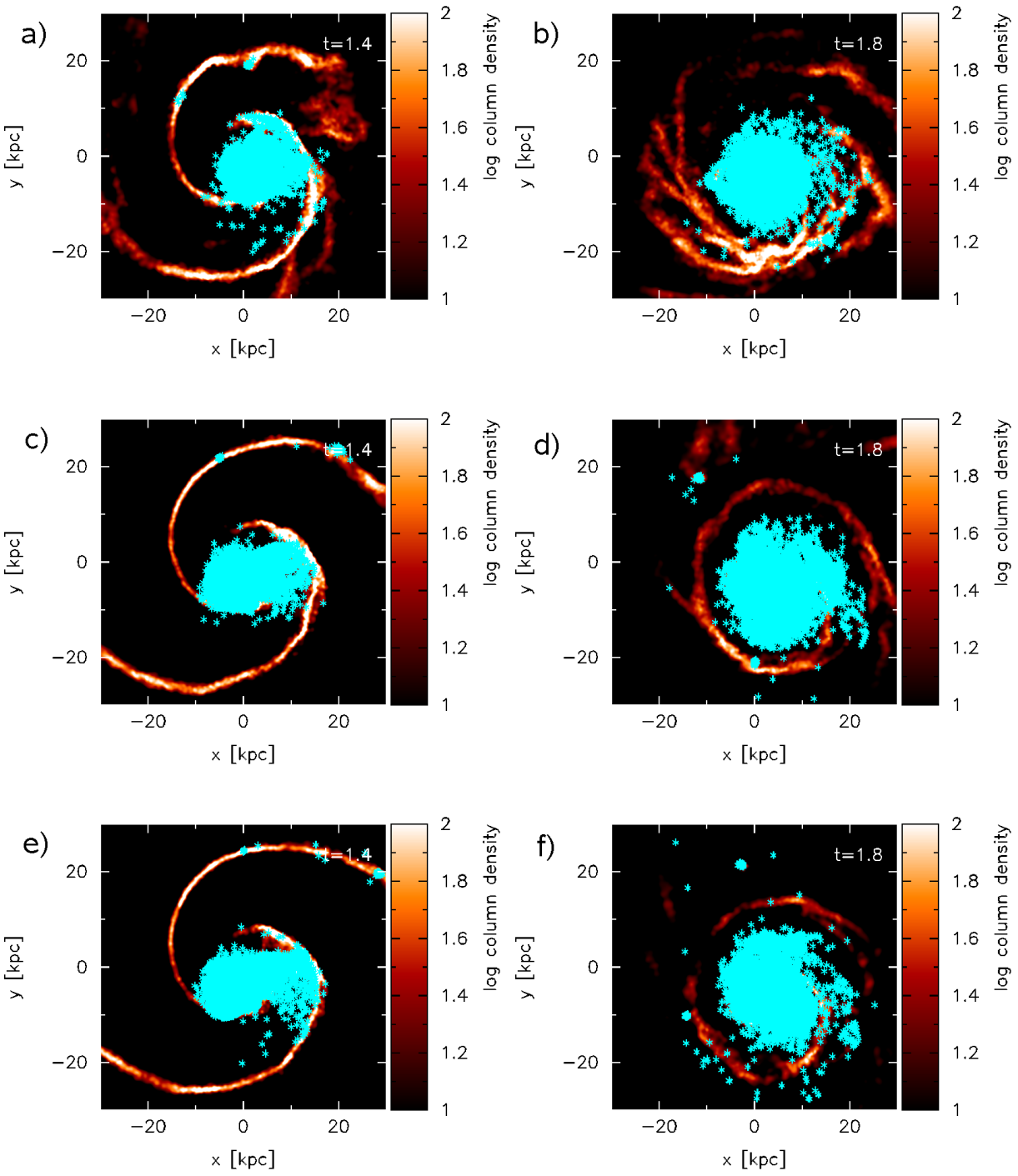

Figure 3.16: Gas density distribution and new stellar particles (turquoise stars) at resolution level R1, with $R_s = 7$ kpc (a), b)), $R_s = 17$ kpc (c), d)), $R_s = 27$ kpc (e), f)) and stellar feedback deactivated; for $t = 1.4$ Gyr (a), c), e)) and $t = 1.8$ Gyr (b), d), f)).

The clear grand-design spiral structure up to $r \sim 30$ kpc disappears after deactivation of the external potential. Star formation is again concentrated in the central region.

For all three cases of $R_{\rm s}$, after switching off the external potential, the galaxy undergoes a winding up phase during which the large-scale spiral structure, which was set into the disc, becomes less pronounced. The phase ends up in an irregular flocculent spiral structure. The larger $R_{\rm s}$ is chosen, the more the large-scale spiral structure in the outer parts is pronounced due to the stronger external gravitational potential there. Star formation takes place for all cases and the chosen critical density mainly in the central regions and less in the spiral arms.

3.7.2 Variation of ρ_0 without stellar feedback

The previous examples for different $R_{\rm s}$ have shown that a large ρ_0 leads to clear grand-design spiral arms and very low mass interarm regions. In addition, a large ρ_0 can destroy the rotational motion in the disc by holding the particles in the spiral arm regions for a long time. The parameter that has to be adjusted hence is ρ_0 in order to provide sufficiently large gas densities in the interarm regions. The strength of the external potential is therefore varied in this subsection by varying the parameter ρ_0. Starting from the value $\rho_0 \sim 4 \times 10^8$ $\mathrm{M}_\odot/\mathrm{kpc}^3$, we vary ρ_0 slightly for two different $R_{\rm s}$ values.

External potentials with $R_{\rm s} = 7$ kpc

In Figure 3.16 a) and b), it is shown that the interarm regions are too low-mass, whereas the spiral structure till $r \sim 20$ kpc is clearly visible. After 0.4 Gyr, an irregular flocculent spiral structure dominates the large-scale shape of the galaxy.

In Figures 3.17, the evolution of the galaxy is studied at resolution level R1 for $R_{\rm s} = 7$ kpc, $\rho_0 = 2 \times 10^8$ $\mathrm{M}_\odot/\mathrm{kpc}^3$ (a) and b)) and 10^8 $\mathrm{M}_\odot/\mathrm{kpc}^3$ (c) and d)), which is an external potential of the half and quarter strength, respectively, as shown in Figure 3.16 a), b). For $\rho_0 = 2 \times 10^8$ $\mathrm{M}_\odot/\mathrm{kpc}^3$ in a) and b), the outer interarm regions show larger, but still insufficient gas densities. In the central regions with $r \lesssim 15$ kpc, the interarm regions show almost no gas content. Hence, the external potential for $R_{\rm s} = 7$ kpc must be even weaker. For $\rho_0 = 10^8$ $\mathrm{M}_\odot/\mathrm{kpc}^3$ in c) and d), most of the regions show that the gas density ratio between spiral arm and interarm regions is $\rho_{\rm arm}/\rho_{\rm interarm} \lesssim 10$ and physically acceptable. In both simulations, the grand-design spiral arms wind up indicating the presence of material arms.

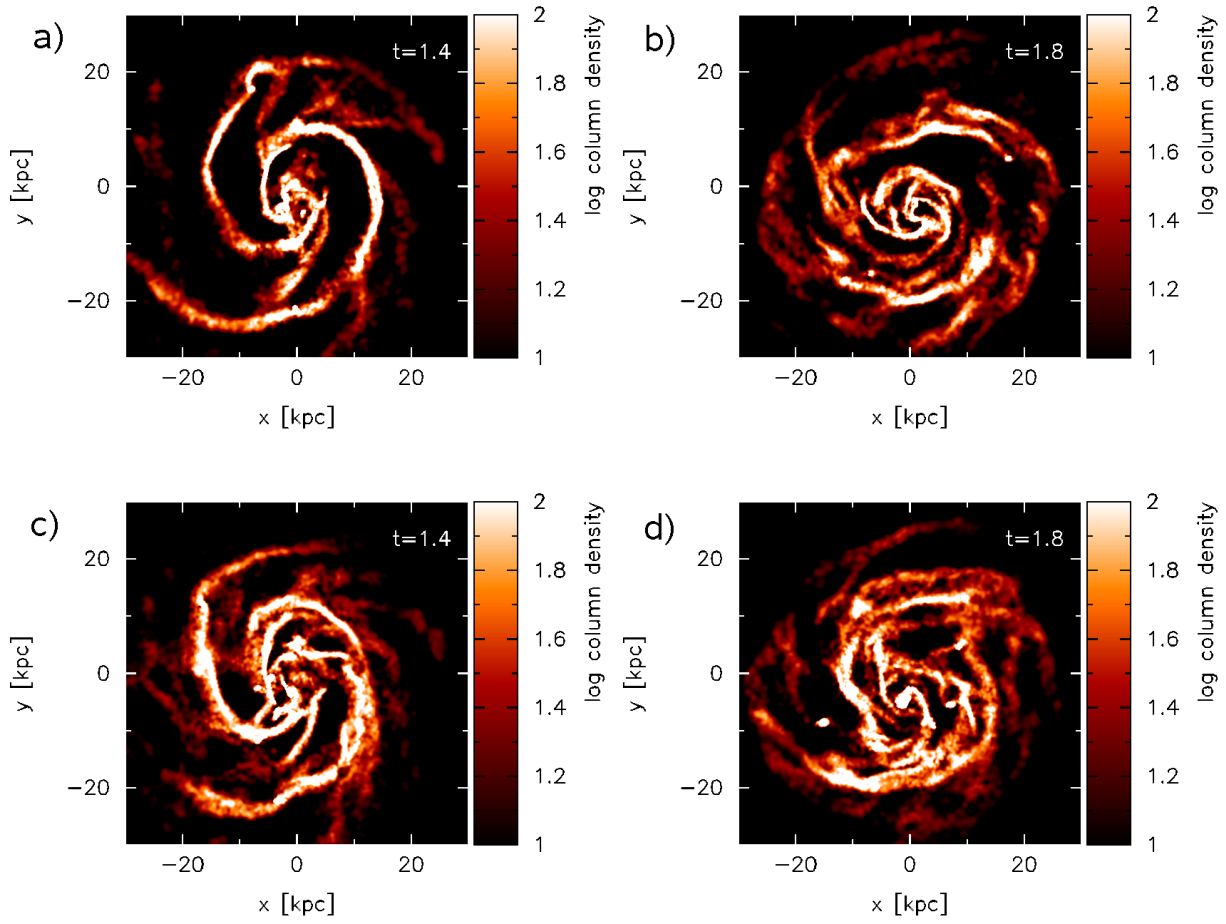

Figure 3.17: Gas density distribution for $t = 1.4$ Gyr (a), c)) and $t = 1.8$ Gyr (b), d)), at resolution level R1, for $R_\mathrm{s} = 7$ kpc, $\rho_0 = 2 \times 10^8$ $\mathrm{M}_\odot/\mathrm{kpc}^3$ (a) and b)) and $\rho_0 = 10^8$ $\mathrm{M}_\odot/\mathrm{kpc}^3$ (c) and d)). Stellar feedback is deactived and the critical density is $\rho_\mathrm{crit} = 5 \times 10^7$ $\mathrm{M}_\odot/\mathrm{kpc}^3$.

External potentials with $R_\mathrm{s} = 17$ kpc

For $R_\mathrm{s} = 17$ kpc, we have shown in Figure 3.16 c) and d) that the external potential is too strong even in very large distances $r \sim 30$ kpc leading to gasless interarm regions.

Figure 3.18 hence shows a galaxy at resolution level R1, with $R_\mathrm{s} = 17$ kpc, $\rho_0 = 10^8$ $\mathrm{M}_\odot/\mathrm{kpc}^3$ (a) and b)) and $\rho_0 = 5 \times 10^7$ $\mathrm{M}_\odot/\mathrm{kpc}^3$ (c) and d)), an external potential with only 1/4 and 1/8, respectively, of the potential used for Figure 3.16 c), d). For $\rho_0 = 10^8$ $\mathrm{M}_\odot/\mathrm{kpc}^3$, in the central region with $r \lesssim 10$ kpc, gas ist present both in the spiral and interarm regions. For larger distances, the influence of the external potential is again too strong leading to gas-poor interarm regions. After deactivating the external potential, the grand-design structure again

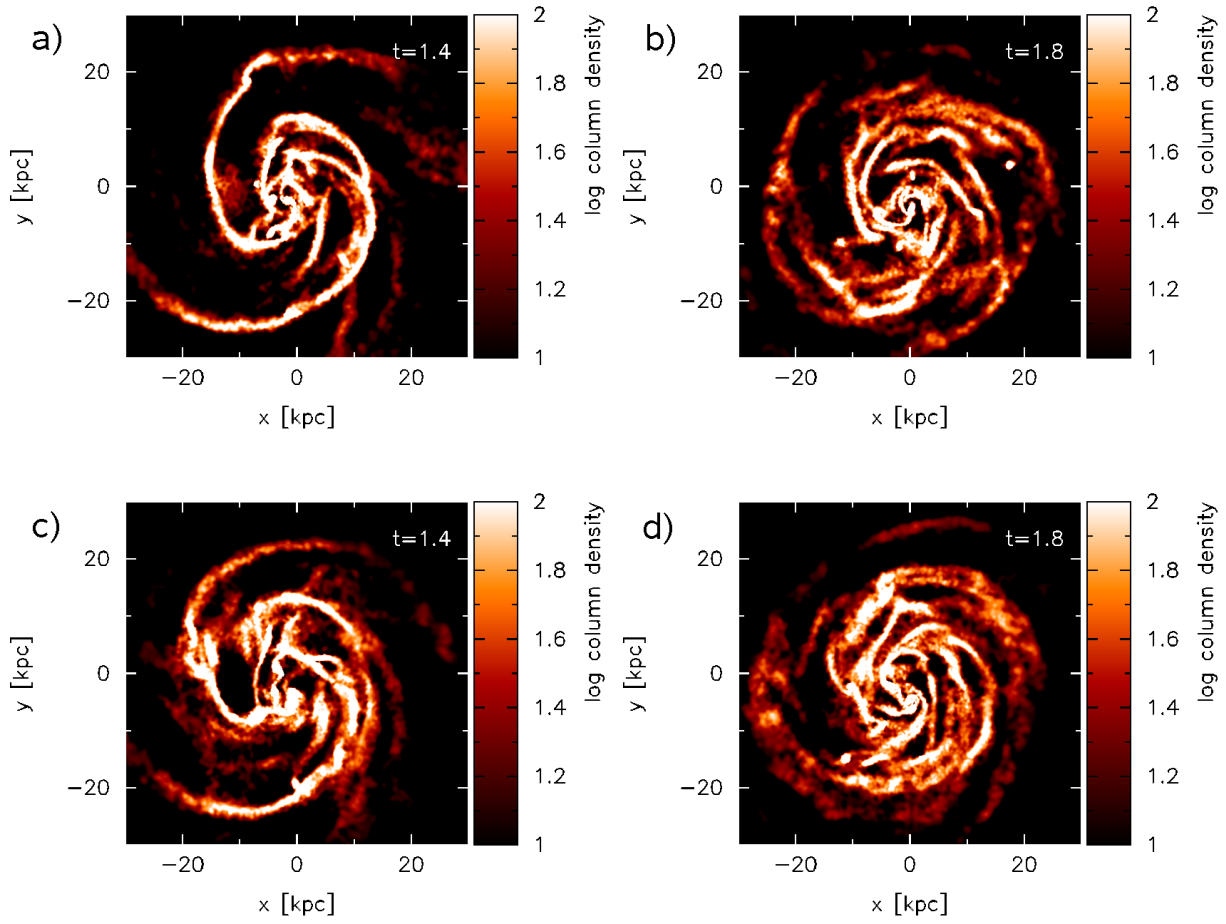

Figure 3.18: Gas density distribution for $t = 1.4$ Gyr (a), c)) and $t = 1.8$ Gyr (b), d)), at resolution level R1, with $R_\mathrm{s} = 17$ kpc, $\rho_0 = 10^8\ \mathrm{M}_\odot/\mathrm{kpc}^3$ (a) and b)) and $\rho_0 = 5 \times 10^7\ \mathrm{M}_\odot/\mathrm{kpc}^3$ (c) and d)). Stellar feedback is deactivated and the critical density is $\rho_\mathrm{crit} = 5 \times 10^7\ \mathrm{M}_\odot/\mathrm{kpc}^3$.

disappears within a short timespan.

A further decrease of the external potential to $\rho_0 = 5 \times 10^7\ \mathrm{M}_\odot/\mathrm{kpc}^3$, shown in c) and d) of Figure 3.18, results in interarm regions with higher gas densities, which at first sight is a positive result. But in the inner region, the weak external potential has such a small influence over the disc that the imposed spiral structure disappears in the irregular flocculent structure.

Again, as shown in Figure 3.18, both simulations of $R_\mathrm{s} = 17$ kpc produce grand-design spiral arms that are kinematic density waves or material arms. These arms wind up fast and disappear in the irregular flocculent structure of the disc.

3.7.3 Variation of ρ_0 with stellar feedback

External potentials with $R_s = 7$ kpc

Figure 3.19 shows the gas density distribution and new stellar particles (turquoise stars) for $R_s = 7$ kpc, $\rho_0 = 10^8$ M$_\odot$/kpc^3, $t = 1.4$ Gyr a) and $t = 1.8$ Gyr b), at resolution level R1 and with stellar feedback switched on. Due to the weak external potential in the whole galaxy, star

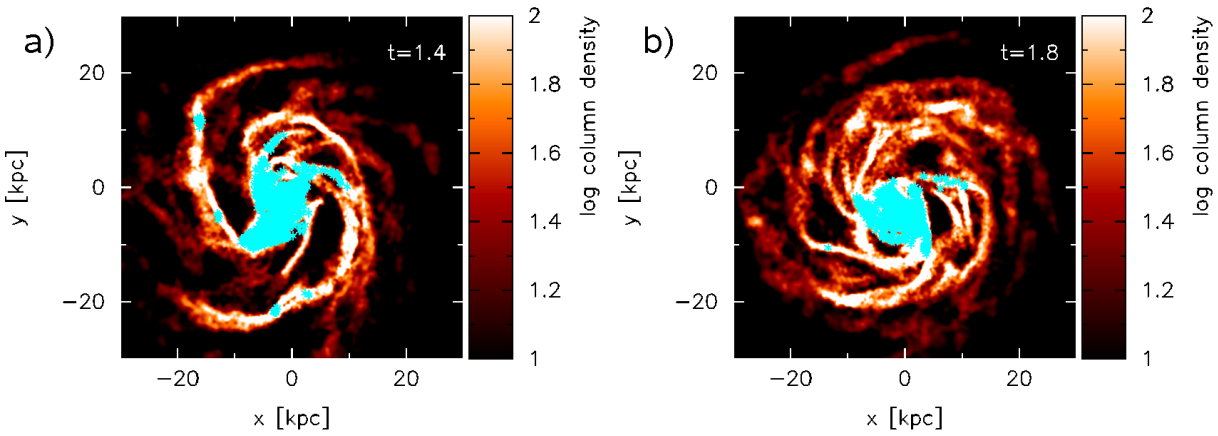

Figure 3.19: Density distribution of the gas phase and new stellar particles (turquoise stars) for $t = 1.4$ Gyr a) and $t = 1.8$ Gyr b), at resolution level R1, for $R_s = 7$ kpc and $\rho_0 = 10^8$ M$_\odot$/kpc^3. Stellar feedback is activated, the critical density is $\rho_{crit} = 5 \times 10^7$ M$_\odot$/kpc^3.

formation is mainly concentrated in the central region and absent in the spiral arms. Therefore, stellar feedback cannot affect the spiral arm evolution of the galaxy.

A way to enable star formation in the outer regions is to set the critical density for star formation to a lower value. This is done in Figure 3.20 for $R_s = 7$ kpc and $\rho_0 = 10^8$ M$_\odot$/kpc^3. In Figure 3.20 a) and b), the critical density for star formation is $\rho_{crit} = 10^7$ M$_\odot$/kpc^3, whereas for c) and d) it is $\rho_{crit} = 5 \times 10^6$ M$_\odot$/kpc^3.

A critical density of $\rho_{crit} = 10^7$ M$_\odot$/kpc^3 still shows no satisfactory star formation rate in the spiral arms. Star formation is still realized mainly in the central regions whereas the gas particles in the spiral arm regions do not reach the required critical density. A further decrease of the critical density down to $\rho_{crit} = 5 \times 10^6$ M$_\odot$/kpc^3 finally enables a significant large number of stellar particles forming in the spiral arm regions. But in the central regions, star formation is so dominant that stellar particles do not only mark the grand-design structure, but rather the combination of irregular flocculent and grand-design structure, leading to a diffuse and unsymmetric appearance. After deactivating the external potential, the grand-design spiral structure hence disappears as in

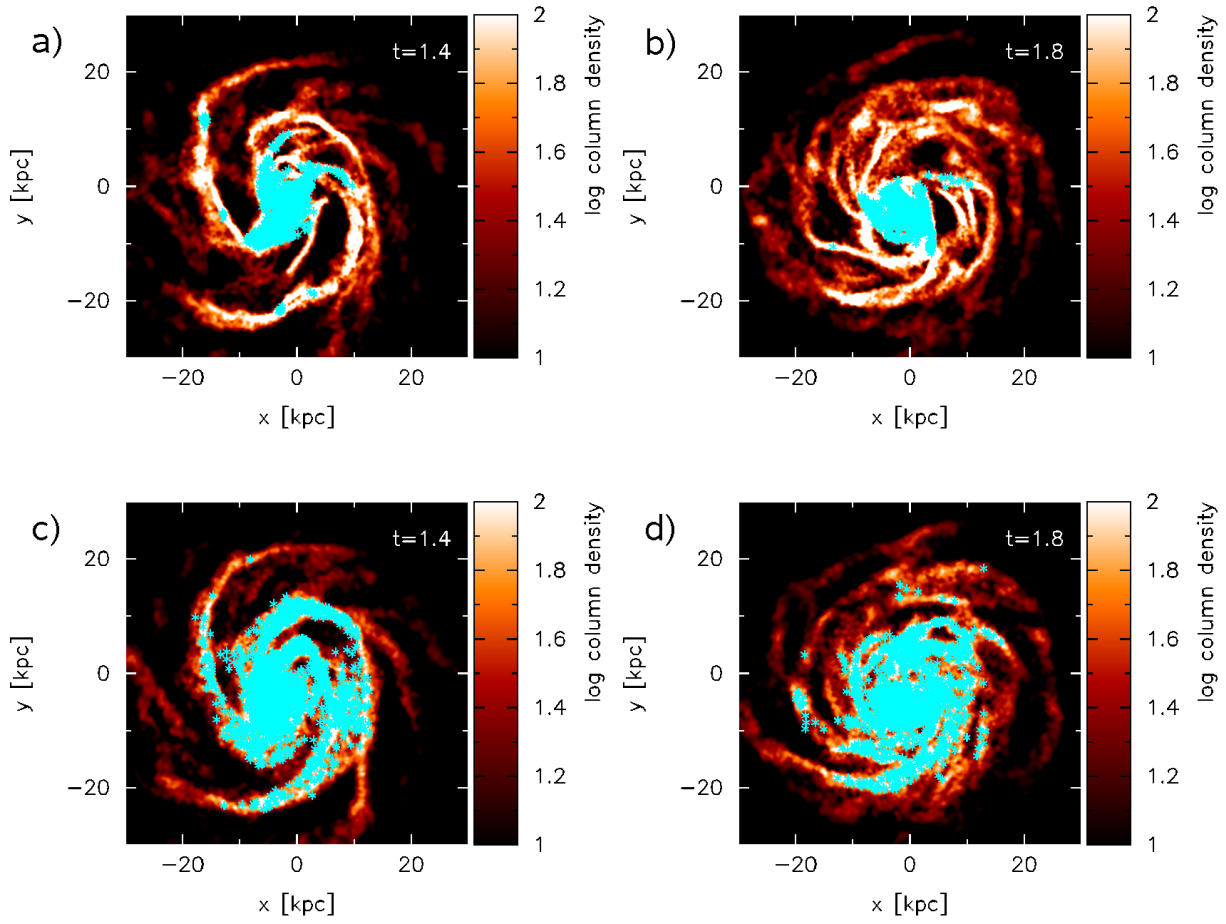

Figure 3.20: Gas density distribution and new stellar particles (turquoise stars) at level R1, for $t = 1.4$ Gyr (a), c)), $t = 1.8$ Gyr (b),d)), $R_{\rm s} = 7$ kpc, $\rho_0 = 10^8$ $\mathrm{M}_\odot/\mathrm{kpc}^3$ and stellar feedback enabled. Critical densities are $\rho_{\rm crit} = 10^7$ $\mathrm{M}_\odot/\mathrm{kpc}^3$ (a), b)) and $\rho_{\rm crit} = 5 \times 10^6$ $\mathrm{M}_\odot/\mathrm{kpc}^3$ (c), d)).

the previous cases. Stellar feedback does not only act near the grand-design spiral arms, but also in the flocculent arms, so that it cannot sustain a large-scale symmetric structure in the disc.

External potentials with $R_{\rm s} = 17$ kpc

For $R_{\rm s} = 17$ kpc, Figure 3.21 shows the gas density distribution and new stellar particles (turquoise stars) for $\rho_0 = 5 \times 10^7$ $\mathrm{M}_\odot/\mathrm{kpc}^3$, $\rho_{\rm crit} = 5 \times 10^7$ $\mathrm{M}_\odot/\mathrm{kpc}^3$, $t = 1.4$ Gyr (a) and $t = 1.8$ Gyr (b), at resolution level R1.

In Figure 3.21, the grand-design spiral arms in the outer regions are not clear due to its small density ρ_0, while the central region is a place of active star formation. The stellar particles are

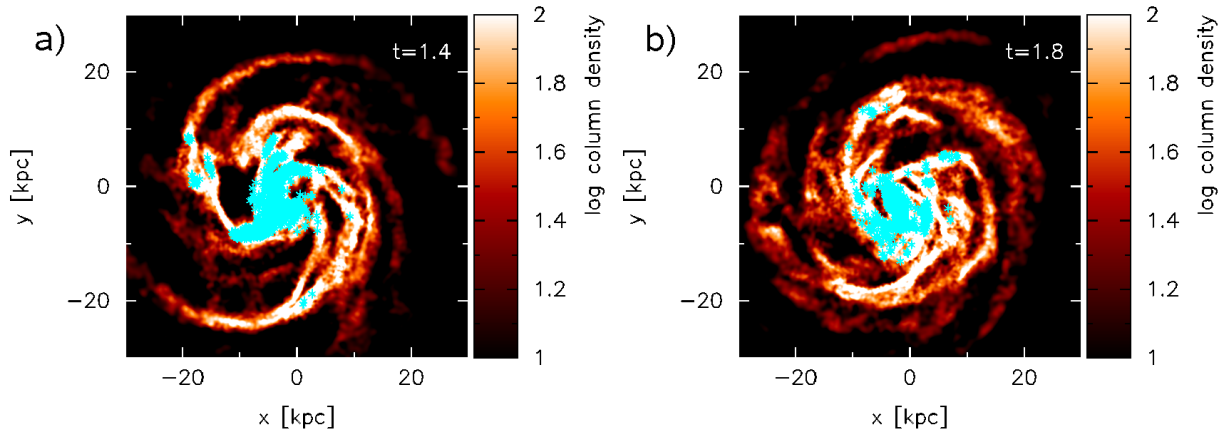

Figure 3.21: Density distribution of the gas phase and new stellar particles (turquoise stars) at resolution level R1, for $R_{\rm s} = 17$ kpc and $\rho_0 = 5 \times 10^7$ M$_\odot$/kpc^3 for a) $t = 1.4$ Gyr and b) $t = 1.8$ Gyr. Stellar feedback is switched on and the critical density is $\rho_{\rm crit} = 5 \times 10^7$ M$_\odot$/kpc^3.

again formed irregularly in the central regions.

In a last step, the critical density $\rho_{\rm crit}$ is again decreased for the case $R_{\rm s} = 17$ kpc. Instead of $\rho_{\rm crit} = 5 \times 10^7$ M$_\odot$/kpc^3 as for Figure 3.21 we apply $\rho_{\rm crit} = 10^7$ M$_\odot$/kpc^3 (a) and b)) and $\rho_{\rm crit} = 5 \times 10^6$ M$_\odot$/kpc^3 (c) and d)) in Figure 3.22.

Figure 3.22 shows that still star formation is mainly concentrated in the central regions. The grand-design gas spiral arms are still regions where star formation does not take place due to their small densities. A decrease of $\rho_{\rm crit}$ cannot enable star formation in the outer regions.

The two different values 7 kpc and 17 kpc for $R_{\rm s}$ largely lead to the same problems and structures in the galaxy. In the case of strong external potential, the interarm regions are too gas-poor. In the case of weak but still efficient external potentials, the interarm regions keep their irregular structures. Star formation in the spiral arms can only be enabled by decreasing the critical density $\rho_{\rm crit}$, which in turn necessarily increases the star formation rate in the center and interarm regions. The grand-design spiral structure disappears in a short time span of order 0.5 Gyr in all cases we have studied. This is mainly due to the nature of the created spiral arms and the insufficient resolution.

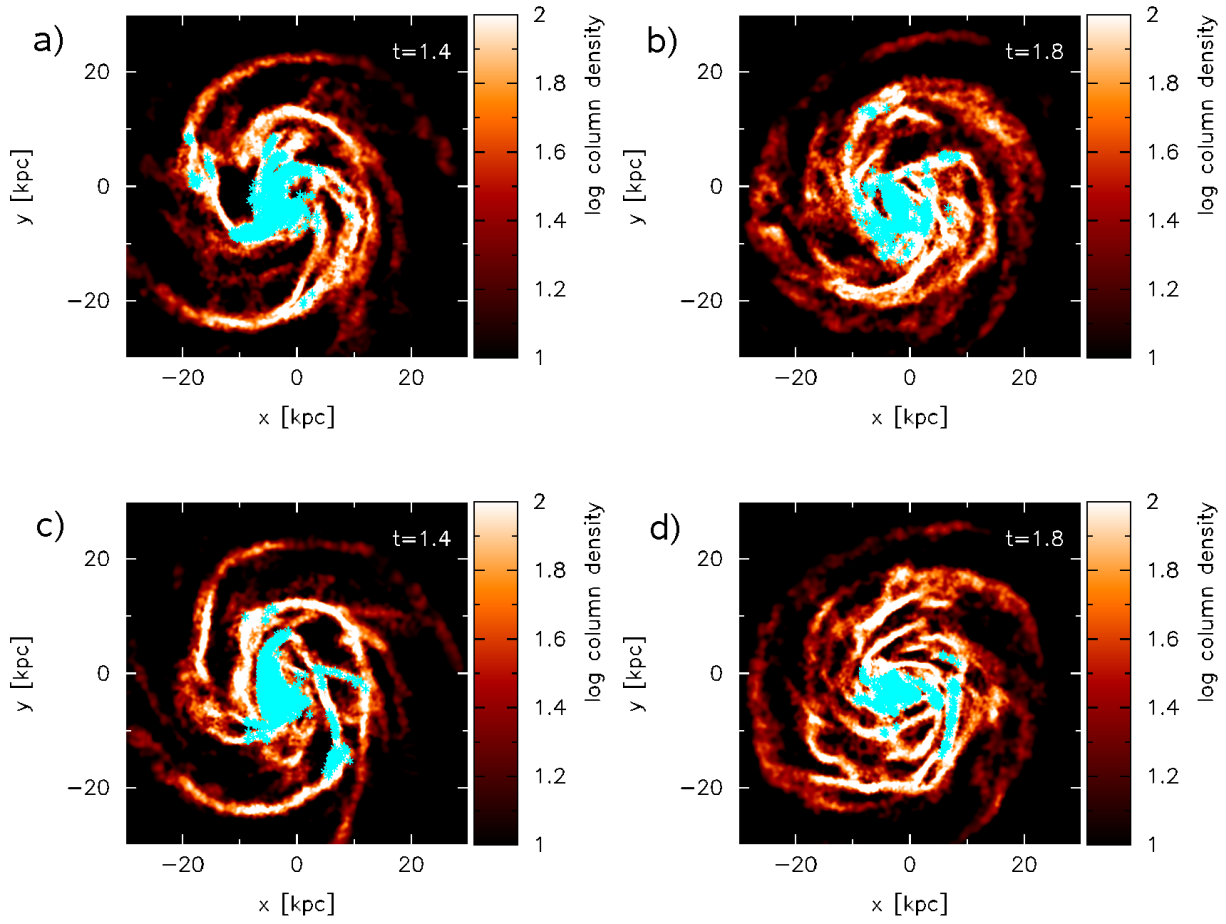

Figure 3.22: Gas density distribution and new stellar particles (turquoise stars) at resolution level R1, for $t = 1.4$ Gyr in a) and c), $t = 1.8$ Gyr in b) and d), $R_\mathrm{s} = 17$ kpc, $\rho_0 = 5 \times 10^7$ $\mathrm{M}_\odot/\mathrm{kpc}^3$ and stellar feedback activated. The critical densities are $\rho_\mathrm{crit} = 10^7$ $\mathrm{M}_\odot/\mathrm{kpc}^3$ for a) and b) and $\rho_\mathrm{crit} = 5 \times 10^6$ $\mathrm{M}_\odot/\mathrm{kpc}^3$ for c) and d).

3.7.4 Higher resolution levels

In Figure 3.23, the gas density distribution for the time steps $t = 0.8$ Gyr (a), c)), $t = 1.2$ Gyr (b), d)), $R_s = 7$ kpc, $\rho_0 = 10^8$ $M_\odot/\mathrm{kpc}^3$ and resolution level R4 is shown. In a) and b) stellar feedback is deactivated, whereas in c) and d) it is activated. In c) and d), new stellar particles (turquoise stars) are also shown. At this higher resolution level, the grand-design spiral structure in the gas density distribution also disappears after a short time (0.4 Gyr) after deactivating the external potential. The large-scale structures of the simulations with and without stellar feedback do not differ.

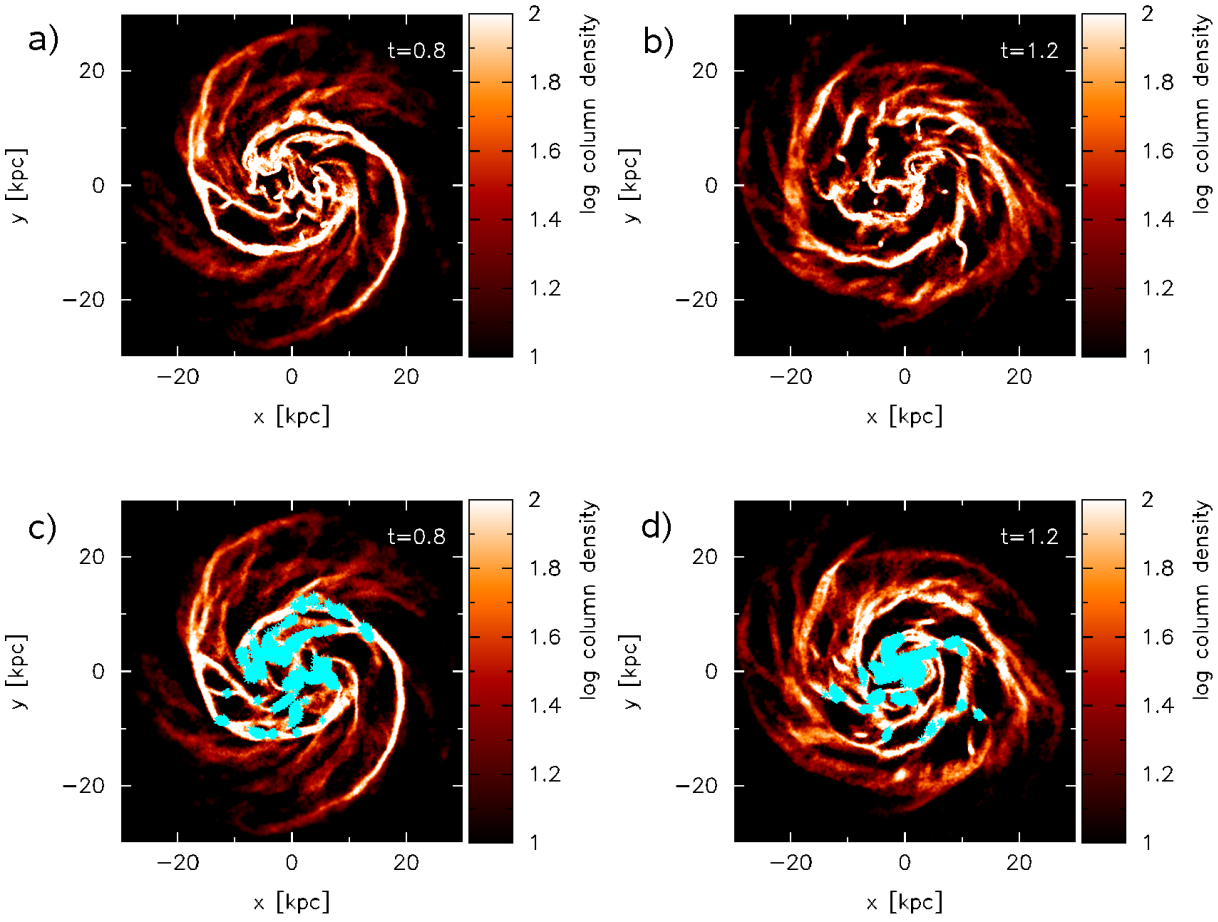

Figure 3.23: Gas density distribution and new stellar particles (turquoise stars) at resolution level R4, for $t = 0.8$ Gyr (a), c)), $t = 1.2$ Gyr (b), d)), $R_s = 7$ kpc and $\rho_0 = 10^8$ $M_\odot/\mathrm{kpc}^3$. In a) and b) no stellar feedback is active, while in c) and d) stellar feedback is activated. For both simulations, the critical density for star formation is $\rho_{\mathrm{crit}} = 5 \times 10^8$ $M_\odot/\mathrm{kpc}^3$.

In Figure 3.24, the gas density distribution for $t = 1$ Gyr (a), c)), $t = 1.4$ Gyr (b), d)), $R_s = 17$ kpc, $\rho_0 = 10^8$ $M_\odot/\mathrm{kpc}^3$ and resolution level R4 is shown for the case of stellar feedback activated. In a) and b), the critical density for star formation is $\rho_{\mathrm{crit}} = 10^9$ $M_\odot/\mathrm{kpc}^3$. In c) and d), it is $\rho_{\mathrm{crit}} = 10^8$ $M_\odot/\mathrm{kpc}^3$. The grand-design spiral structure disappears after a very short time after deactivating the external potential.

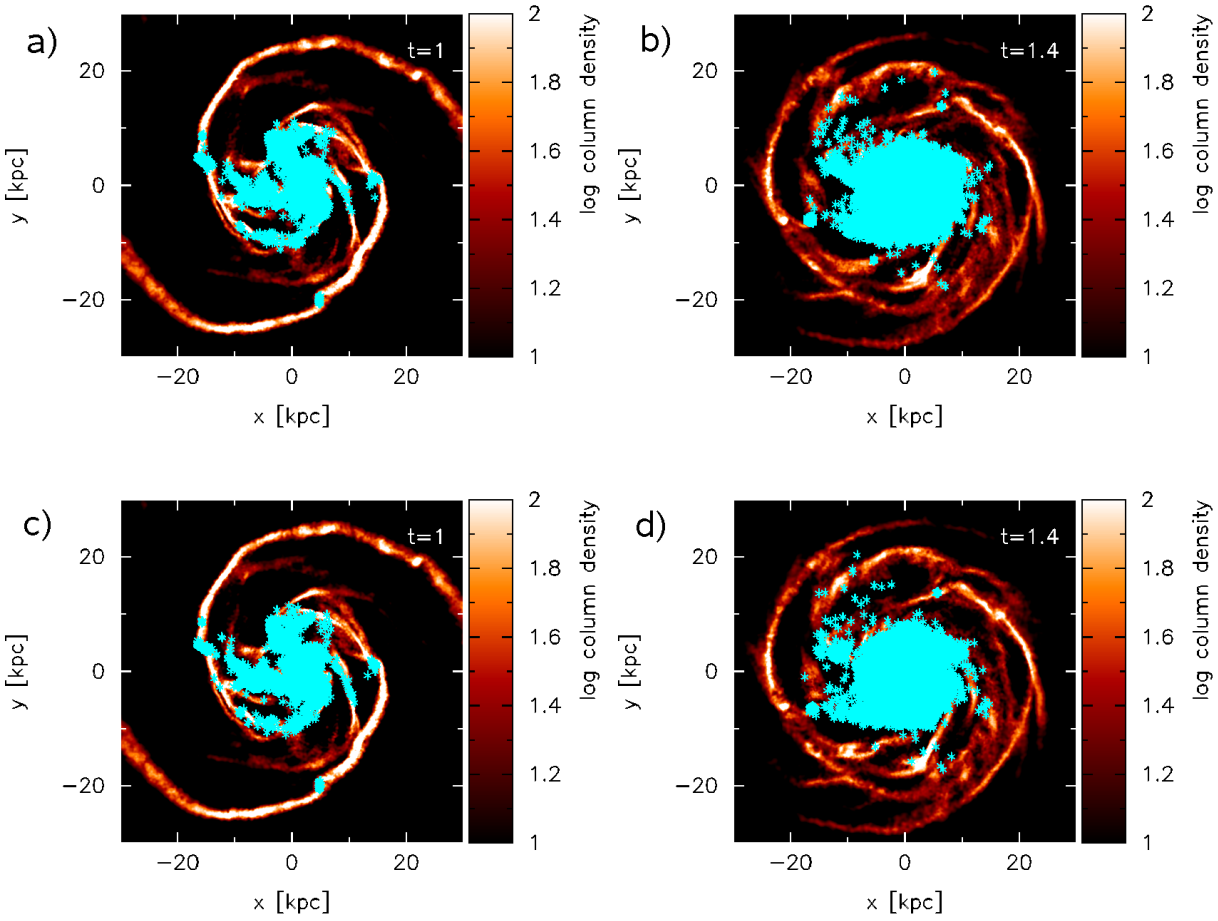

Figure 3.24: Density distribution of the gas phase and new stellar particles (turquoise stars) at resolution level R4, for $t = 1$ Gyr (a), c)), $t = 1.4$ Gyr (b), d)), $R_s = 17$ kpc and $\rho_0 = 10^8$ $M_\odot/\mathrm{kpc}^3$. Stellar feedback is activated. The critical densities are $\rho_{\mathrm{crit}} = 10^9$ $M_\odot/\mathrm{kpc}^3$ in a), b) and $\rho_{\mathrm{crit}} = 10^8$ $M_\odot/\mathrm{kpc}^3$ in c), d).

The external potential in Figure 3.24 is too strong which leads to very gas-poor interarm regions. Therefore, in Figure 3.25, a study of the galaxy with $R_s = 17$ kpc and $\rho_0 = 5 \times 10^7$ $M_\odot/\mathrm{kpc}^3$ is shown for resolution level R4, without and with stellar feedback.

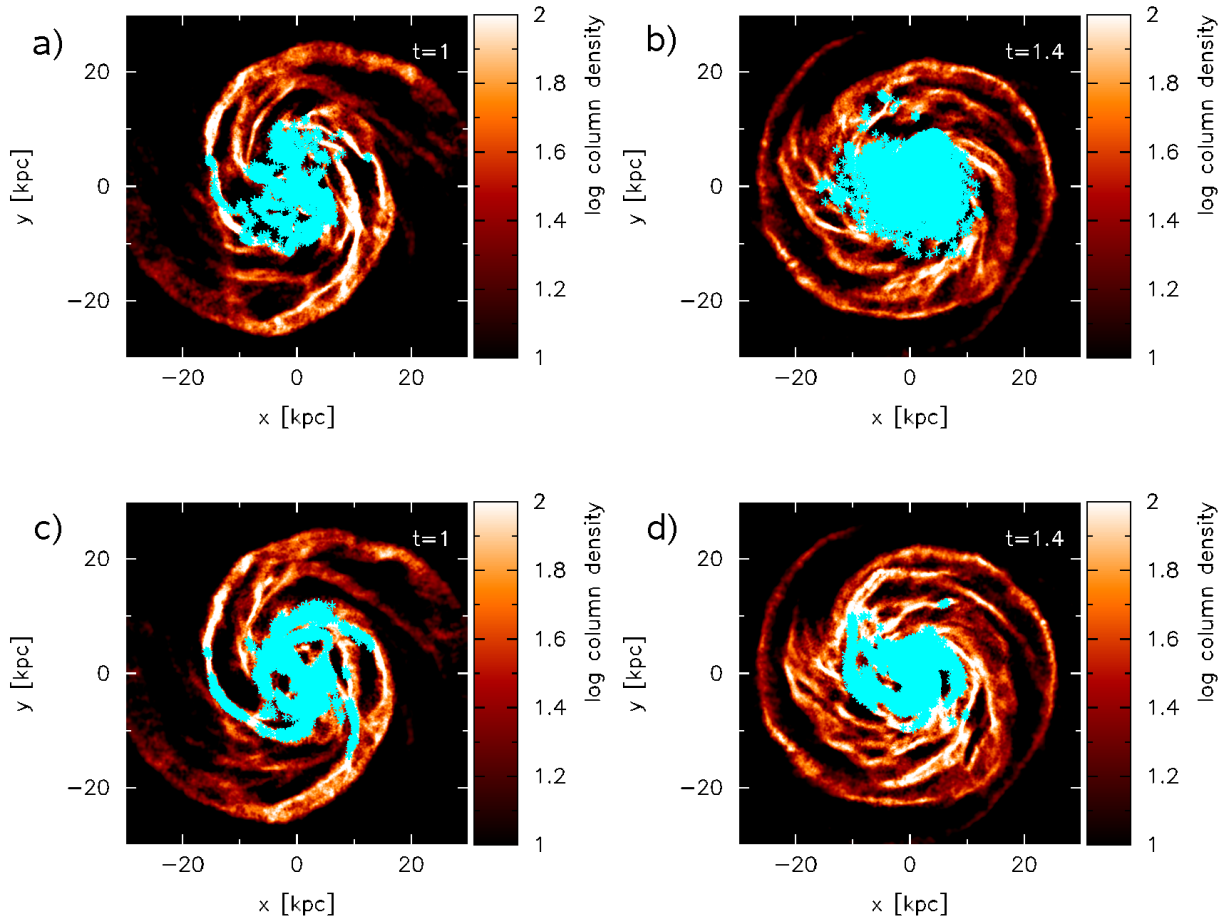

Figure 3.25: Gas density distribution and new stellar particles (turquoise stars) at resolution level R4, for $t = 1$ Gyr (a), c)), $t = 1.4$ Gyr (b), d)), $R_{\rm s} = 17$ kpc and $\rho_0 = 5 \times 10^7$ $\mathrm{M}_\odot/\mathrm{kpc}^3$. Stellar feedback is deactivated in a), b) and active in c), d). The critical density is $\rho_{\rm crit} = 10^8$ $\mathrm{M}_\odot/\mathrm{kpc}^3$.

At time $t = 1$ Gyr, when the external potential is switched off, the grand-design structure is very prominent, with moderate interarm gas densities and star formation in the grand-design spiral arm up to $r \sim 10$ kpc. After 0.4 Gyr, the two spiral arms have wound up and are only visible in the outermost regions. For $r \lesssim 20$ kpc, the irregular flocculent spiral structure is predominant.

Simulations at resolution level R4 have shown that due to the smaller gravitational softening length (R4: $\epsilon_{\rm g} = 0.2$ kpc compared to R1: $\epsilon_{\rm g} = 0.4$ kpc), grand-design as well as flocculent spiral structures in the galaxy are better resolved. However, the winding up problem arises for all studied cases. This indicates that all the produced spiral arms are kinematic density waves or material arms. The enhancement of resolution has not changed the nature of the spiral arms.

3.8 Modified external potential

In comparison to the classical density wave theory (DWT), the original external potential that was applied in Subsection 3.7 affects the disc material in another way than it is predicted by the DWT. In the framework of DWT, a small density perturbation propagates in the disc, which itself is in equilibrium. Most of the disc matter hence should experience no external force.

However, the external potential used in Subsection 3.7 affects almost all disc particles significantly. This can be seen clearly in many previous plots with almost empty interarm regions. The reason for this non-vanishing external force in the numerical simulation lies in the fact that the gas particles randomly create shock fronts due to dissipation, which can be seen as flocculent spiral arms. In order to generate a large-scale spiral structure, the external potential thus has to overwhelm this flocculent feature leading to significantly large perturbations of the external potential.

In order to approach the DWT as much as possible and create a density wave, we hence apply a modified external potential. This modified external potential is characterized by the following properties.

- All $\Phi_{\text{ext}}(r,\theta) > 0$ are ignored, thus set to $\Phi_{\text{ext}}(r,\theta) = 0$,
- $\Phi_{\text{ext}}(r,\theta) < 0$ only affects the disc particles, if it is smaller than $u \cdot \Phi_{\min}$, with $0 < u < 1$ and $\Phi_{\min} = -4\pi \text{G} H \rho_0 \exp\left(-\frac{r-r_0}{R_\text{s}}\right) \sum_{n=1}^{3} \frac{C_n}{K_n D_n}$.

Figure 3.26 shows the unmodified external potential Φ_{ext} in a) and b) in comparison to two modified external potentials $\Phi_{\text{ext}} \leq 1/3\ \Phi_{\min}$ in c) and $\Phi_{\text{ext}} \leq 2/3\ \Phi_{\min}$ in d). The larger u is, the narrower are the spiral arms of the modified external potential.

We now discuss simulation results for one specific external potential and two different values of u. The external potential is specified by the amplitude of the perturbation $\rho_0 = 10^8\ \text{M}_\odot/\text{kpc}^3$, $N = 2$, $r_0 = 8$ kpc, $R_\text{s} = 17$ kpc, $H = 0.18$ kpc, pitch angle $\alpha = 20°$, pattern speed $\Omega_p = 4\,\pi/\text{Gyr}$, $\Delta t = 4 \times 10^7$ yr, critical density for star formation $\rho_{\text{crit}}(\text{R1}) = 5 \times 10^7\ \text{M}_\odot/\text{kpc}^3$ and $\rho_{\text{crit}}(\text{R4}) = 5 \times 10^8\ \text{M}_\odot/\text{kpc}^3$.

3.8.1 $u = 1/3$

A modified external potential with $u = 1/3$ and resolution level R1 in Figure 3.28 a) and b) only shows a faint grand-design spiral structure at time of deactivation of the modified potential. Beside the faint grand-design spiral structure, irregular flocculent spiral arms are very dominant in the disc. After a short time the grand-design structure is not visible any more, leaving the flocculent structure in the disc.

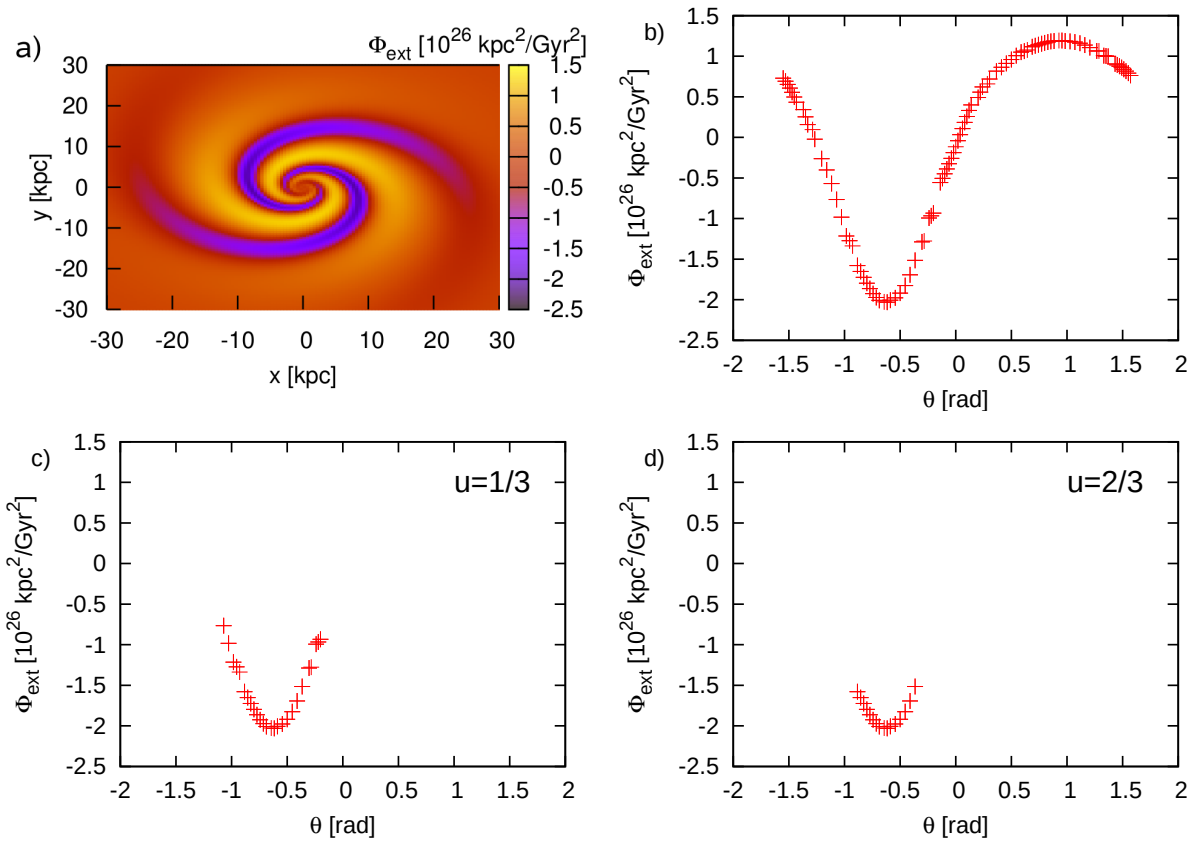

Figure 3.26: Comparison between the unmodified external potential Φ_{ext} in a), b) and the modified external potential in c) ($u = 1/3$) and d) ($u = 2/3$).

The higher resolution level R4 with $u = 1/3$ (Figure 3.28 c) and d)) creates a more clear grand-design structure. After 0.4 Gyr, two tightly wound spiral arms are still visible in the outermost regions of the disc. However, most of the regions in the disc are dominated by irregular flocculent structures.

Both simulations again show the known winding up of the two spiral arms. Resolution level R4 with $u = 1/3$ and additionally stellar feedback (Figure 3.28 e) and f)) creates the same grand-design structure as R4 without stellar feedback. The structure after 0.4 Gyr is also a flocculent one with two faint tightly wound spiral arms in the outer regions of the disc. Star formation mainly takes place randomly in the central region. In the spiral arms, star formation is not common due to insufficient gas densities.

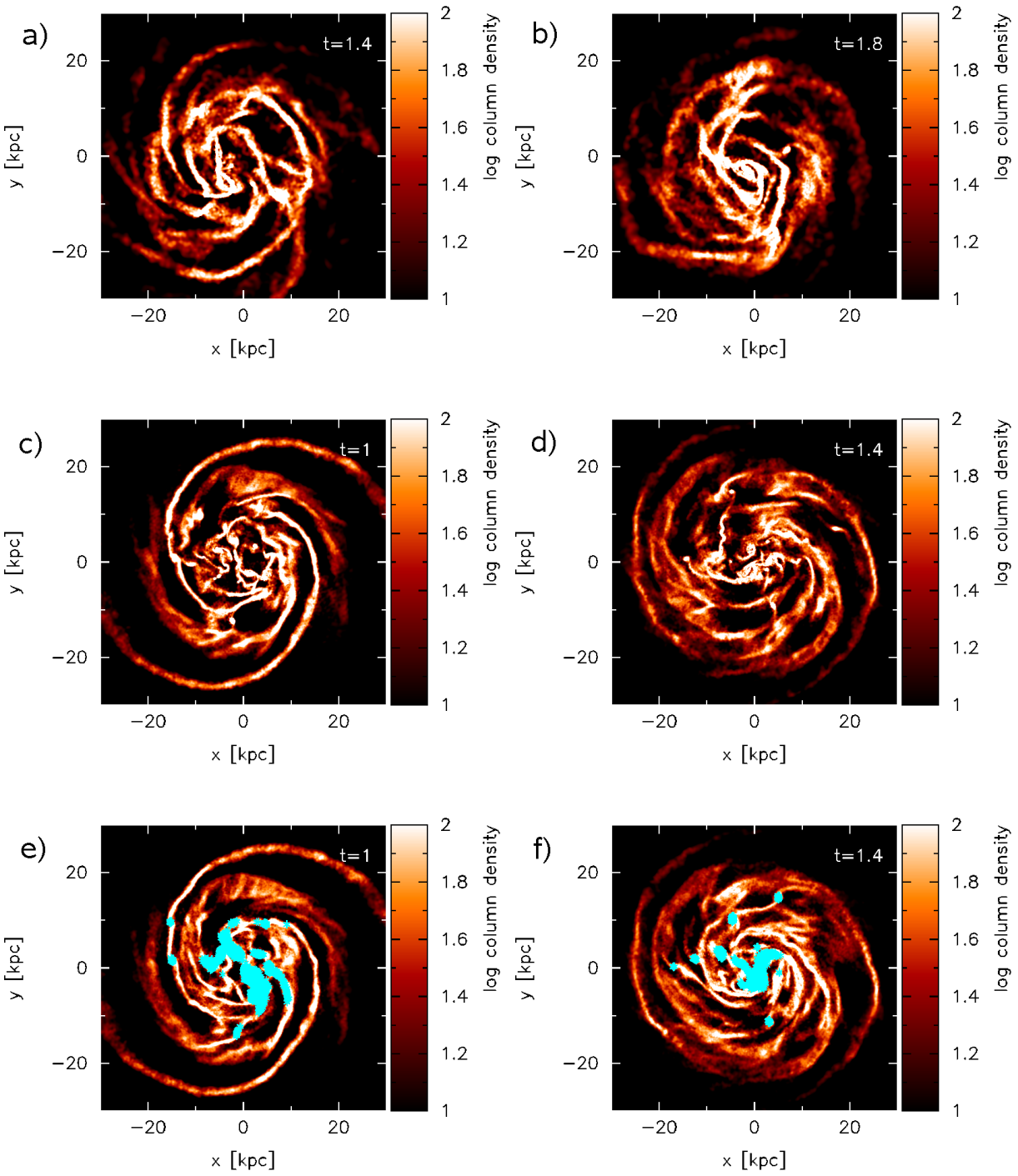

Figure 3.28: Gas density distribution and new stellar particles (turquoise stars) at different times for $u = 1/3$, at resolution levels R1 (a), b)), R4 (c) - f)), without stellar feedback (a) - d)) and with stellar feedback (e), f)).

3.8.2 $u = 2/3$

By applying a potential with $u = 2/3$ and resolution level R1 in Figure 3.27 a) and b), no grand-design spiral structure is visible at time of deactivation of the modified potential. The whole disc is still dominated by irregular flocculent spiral arms.

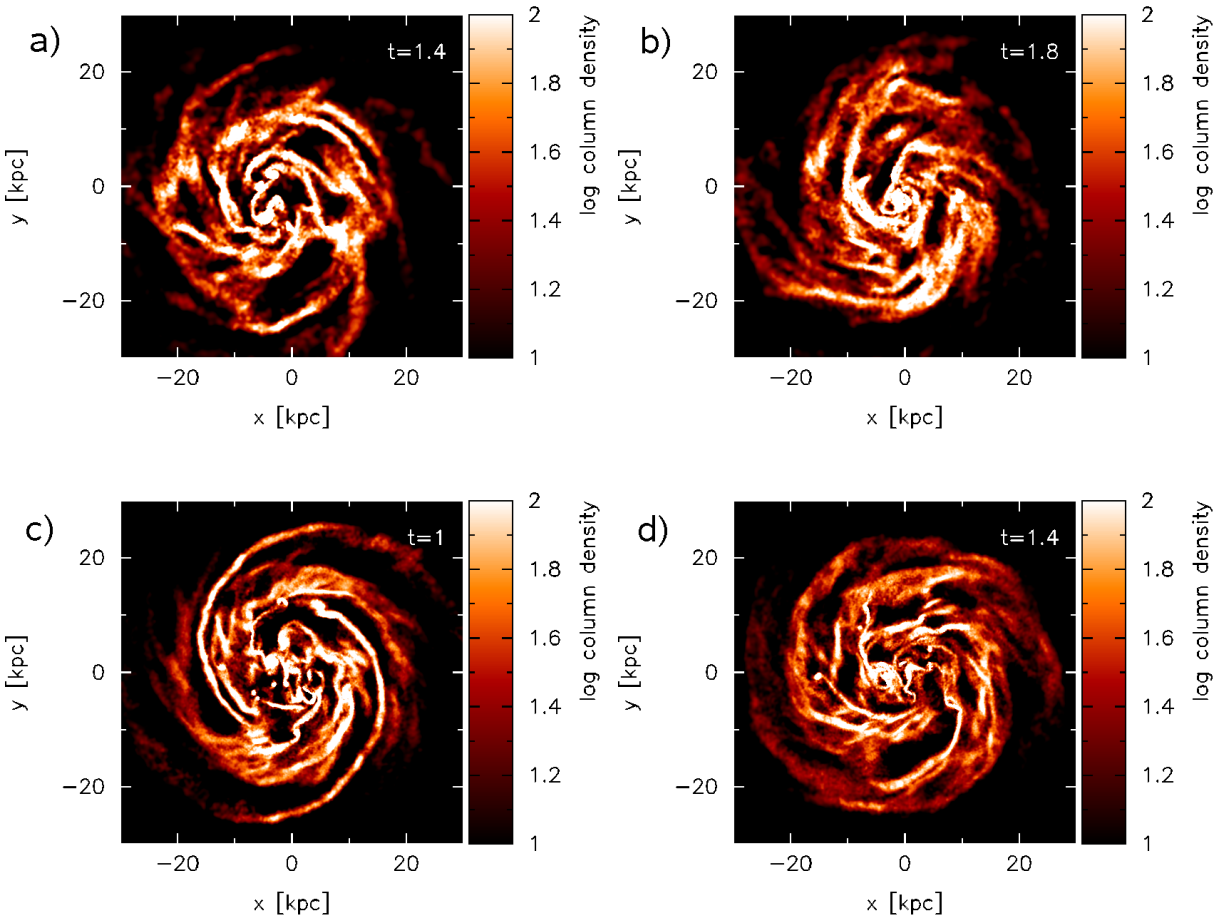

Figure 3.27: Gas density distribution at different times for $u = 2/3$, at resolution level R1 (a), b)) and R4 (c), d)). Stellar feedback is deactivated.

The higher resolution level R4 with $u = 2/3$ (Figure 3.27 c) and d)) in contrast creates two grand-design spiral arms besides flocculent spiral arms in the interarm regions. After 0.4 Gyr, the flocculent structure again dominates the large-scale structure of the disc.

In this Subsection we have shown that the modified external potential is able to produce grand-design spiral structures by not affecting the total disc. But, due to the absence of the potential in the interarm regions, these regions are strongly dominated by irregular flocculent spiral arms.

After the deactivation of the modified external potential, the pitch angle of the grand-design spiral arms decreases indicating a winding up of the arms, which we have already found in the previous subsections. Hence, the result is again the production of material arms.

3.9 Conclusion

In this Chapter, we have presented simulation results of disc galaxies performed with the N-body / SPH code GADGET-2. Here, the main results are summarized, problems and shortcomings of current simulation works are discussed.

3.9.1 Isolated galaxies

Isolated galaxies show prominent flocculent spiral structures in their gas phase, which are transient.

Stellar feedback does not affect the large-scale structure evolution. The only difference that can been seen on galactic scales is that the gaseous densities are larger in the case of stellar feedback activated. This is due to the fact that star formation is strongly suppressed by stellar feedback. The study of the total mass of new stellar particles verifies this statement clearly. Stellar feedback decreases the strong enhancement of star formation in the early phases. Due to the thermal energy, which the gas particles get in the environments of exploding SNe, they are prevented from forming stars quickly. In this way, star formation can take place for a longer period.

3.9.2 Galaxy-perturber interaction

With a punctual mass passing the galaxy, it is possible to create grand-design spiral structures in the galactic disc that agree qualitatively with previous studies (Toomre & Toomre 1972; Oh et al. 2008). A quantitative comparison is not possible due to several different treatments of the galaxies. For example, previous authors have studied collisionless particles whereas in our study, collisionless as well as hydrodynamic particles are studied.

The spiral structures that are created all disappear after a time span, which is dependent on the pitch angle of the created spiral structure. The smaller the pitch angle is, the faster the structure disappears and vice versa the larger the pitch angle is, the longer it takes for the spiral structure to disappear. The structure that is left in the gas phase is always an irregular flocculent spiral structure.

Based on our models, we conclude that the spiral structures that are created with a perturber are transient due to the fact that these are material arms and not density waves.

The question, whether a grand-design spiral structure that originates from a density wave is transient or can survive for a long time can therefore not been answered by using the method of a perturber passing the galaxy since with this method only material arms are created.

3.9.3 External potential

By applying an external gravitational potential, grand-design spiral structures can be produced in a very simple way. Thereby, values in the range $[7, 17]$ kpc for the parameter $R_{\rm s}$, which describes the radial decrease of the external potential, can produce spiral structures up to 30 kpc. A very important observational feature is the ratio between spiral arm and interarm densities, which is a few up to ~ 20 in extreme regions. The external potential hence should reproduce a ratio of e.g. ~ 5 in the inner parts, which increases with increasing radius. This is done by varying the amplitude ρ_0 of the external potential. For $R_{\rm s} = 7$ kpc and 17 kpc, we find $\rho_0 = 10^8\ {\rm M}_\odot/{\rm kpc}^3$ and $\rho_0 = 5 \times 10^7\ {\rm M}_\odot/{\rm kpc}^3$ respective, which lead to interarm regions with sufficient gas content. These realistic grand-design spiral structures undergo a short phase of transformation after deactivation of the external potential and end up in an irregular flocculent spiral structure in the gas phase. In some cases tightly wound spiral arms still exist in the outer regions indicating that the spiral arms are material arms.

The *first* result hence is that all chosen models for the external potential can only produce kinematic density waves or material arms and not classical density waves.

Star formation is realized in the central regions. In the grand-design spiral arms, the density is insufficient to fullfill the star formation criterion. By minimizing the critical density $\rho_{\rm crit}$, star formation can only be realized in the grand-design spiral arms for some isolated cases, which at the same time is accompanied by strong star formation activities in the flocculent spiral arms.

The *second* result hence is that it is not possible to enable star formation only in the grand-design spiral arms. The reason for it is insufficient resolution that always causes large-scale high-density flocculent arms. These flocculent arms have densities at least similar to densities of grand-design spiral arms.

Stellar feedback does not affect the large-scale spiral structure evolution of the galaxy. The main reason lies in the spatial distribution of the new stellar particles. Since the stellar particles mainly form in the central regions, they do not affect the grand-design spiral arms. For small $\rho_{\rm crit}$, stellar particles form in the grand-design spiral arms, but also in the flocculent arms. Hence, the SNe are randomly distributed and cannot only support the grand-design spiral structure.

The *third* result is that stellar feedback at this stage of work still has no influence on the large-scale evolution of galaxies due to the lack of strong star formation processes in the spiral arms.

3.9.4 Modified external potential

Finally, we have concentrated our study on one specific model for the modified external potential. For the chosen modified external potential, only regions with $\Phi_{\mathrm{ext}} \leq 1/3 \cdot \Phi_{\mathrm{min}}$ are affected. The grand-design spiral structure can be seen at resolution level R1 very faintly. For the higher resolution level R4, the grand-design spiral structure is produced clearly among the irregular flocculent structure. After deactivation of the modified external potential, the two spiral arms wind up, get fainter and can only be found in the outer regions.

In the case of $\Phi_{\mathrm{ext}} \leq 2/3 \cdot \Phi_{\mathrm{min}}$, R1 shows no grand-design spiral structure. For the higher resolution level R4, the grand-design spiral structure is again clearly visible. After deactivation of the modified external potential, the same evolution is found as for $u = 1/3$.

For both $u = 1/3$ and $u = 2/3$, stellar feedback has no influence on the large-scale evolution of the galaxy again due to insufficient resolution and its impossibility to enable star formation in the grand-design spiral arms.

3.9.5 Problem analysis

To conclude, a major problem has been found for all mechanisms of creating grand-design spiral structures. In all simulations, the grand-design spiral arms are in fact material arms and not density waves. There is one possible explanation at this stage of work. The resolution is still low for simulations up to 3 Gyr.

Due to the acceleration-dependent regulation of time step in GADGET-2, infinitesimal large accelerations lead to infinitesimal small time steps and this must be prevented. Therefore, the gravitational softening length ϵ_i must be included, which is a completely numerical tool and modifies the gravitational force between the particles. For $\epsilon_i \rightarrow 0$, the gravitational force determined by GADGET-2 converges to the real gravitational force. But $\epsilon_i \rightarrow 0$ can only be realized in the case of infinitesimal large numbers of particles with small masses. The creation and evolution of a density wave is mainly based on the gravitational interactions between the particles. Therefore, an uncertainty of the gravitational force is counteractive to a density wave. If the gravitational softening length is many orders smaller than the widths of the grand-design spiral arms ($\sim 1\ \mathrm{kpc}$), this uncertainty should be negligible. However, with the current resolution levels, this is still not the case. R1 has $\epsilon_{\mathrm{g}} = 0.4\ \mathrm{kpc}$ and R4 $\epsilon_{\mathrm{g}} = 0.2\ \mathrm{kpc}$. For R8, Li et al. (2005) used $\epsilon_{\mathrm{g}} = 20\ \mathrm{pc}$, we used $\epsilon_{\mathrm{g}} = 100\ \mathrm{pc}$. Both lengths already define a very high resolution. Nevertheless, a simulation with $10^6 - 10^7$ particles and all included processes still takes at least several months up to years to reach $t \geq 3\ \mathrm{Gyr}$. For this work, such long time spans are unachievably large computation times.

The insufficient resolution brings along another physical problem. The flocculent spiral arms in the gas phase are strongly exaggerated with high densities and broad arm widths. They dominate the dynamics on galactic scales. Due to their presence, a grand-design spiral structure that is able to overwhelm the gaseous flocculent structure can only be produced if the assumed perturbation (pertuber or external potential) is comparably strong. This however does not represent a classical density wave with small amplitudes anymore. The strong perturbation naturally only produces material arms in the discs.

We therefore claim that a classical grand-design density wave can only be produced numerically in a realistic disc composed of collisionless and gaseous particles, if the discs harbour very small density fluctuations. The upper limit for these density fluctuations, which still allow the production of density waves, must thereby be found numerically with high resolution simulations based on more than $10^6 - 10^7$ particles.

4

Summary and Outlook

4.1 Summary of results

4.1.1 Disc galaxies in the presence of isopedic magnetic fields

We studied scale-free discs embedded in an axisymmetric dark matter halo and crossed by an isopedic magnetic field. For this configuration, the relations between different variables of the equilibrium state are first derived. Then, the dispersion relation for small perturbations in the discs are found. By applying the dispersion relation on stationary perturbations, we studied aligned and unaligned perturbations in the discs.

For aligned perturbations, isopedic magnetic fields have stronger influences on the dark matter content of galaxies of higher redshifts, which contain higher gas ratios than late-type disc galaxies with less gas content.

For unaligend perturbations, realistic magnetic fields require a much higher ratio f between the dark matter and visible content than the typical value $f \sim 10$ in disc galaxies.

We hence have found a relation between the dark matter content and the isopedic magnetic field strength in disc galaxies. For the application of our relation, observations have to yield several parameters such as the surface mass densities or the sound speeds. But the most challenging feature to be determined is whether the structure is stationary (or quasi-stationary) or not. When all required parameters are found, the dark matter content of a galaxy can be determined with the help of the magnetic field strength and vice versa.

4.1.2 Numerical simulation of disc galaxies

We have chosen the N-body / SPH code GADGET-2 for the simulation of disc galaxies. By using up to 4×10^5 particles we studied the evolution of galaxies during a long period of at least $3\ \mathrm{Gyr}$. The three methods that were applied for the creation of a grand-design spiral structure all succeeded in creating the grand-design structure in the disc. The study of the time-dependent evolution of the produced grand-design spiral structures however showed that they all disappear after a short time. Thereby, the structure created by a perturber, survived the longest. The external gravitational potential and the modification of it both created grand-design structures, which disappeared after only $\sim 0.5\ \mathrm{Gyr}$.

In all cases, our results are material arms, which wind up with time. The reason for the production of material arms lies in an insuffient resolution of the simulation. The insuffient resolution leads to a physical discrepancy between numerical and observational studies. In our simulations, the gas phase produces irregular flocculent spiral arms on galactic scales, which dominate the dynamics of the galaxy. Due to their presence, grand-design density waves are not able to persist. In reality, gas and molecular clouds are indeed dissipative, but on a much smaller scale. Therefore, a flocculent spiral structure cannot be expected by only using differential rotation of the disc. This however is found in our numerical simulations, as well as in e.g. Li et al. (2005), and is an indication for the exaggeration of the gas dissipation.

Our study has shown, that the current treatment of gas in galaxies is insuffient for the study of detailed physics in the discs. Due to low resolution and its resulting large-scale flocculent structures, density waves with small density amplitudes cannot be produced.

4.2 Outlook

In the context of analytical studies of disc galaxies, which imply modifications or increments of the density wave theory, we are already at the upper limit of possible studies. Co-planar magnetic fields that lie in the discs have been studied by Lou & Zou (2004, 2006) and Lou & Bai (2006). In disc galaxies, two very important mechanisms are the star formation in molecular clouds and stellar feedback in terms of e.g. stellar winds or SNe. These processes cannot be included in the analytical work.

Contrarily to the analytical work, high-performing parallel simulations are able to realize the two phase transformations between gas and stellar components. However, as we have shown in the second part of this work, resolution plays a very important role in the context of galaxy evolution. In the case of insufficient resolution, numerical simulations are not able to describe the right physical processes in the galaxy. Therefore, very high resolutions with more than $10^6 - 10^7$

particles are necessary which will probably be realized in the future.

The numerical simulations that we have presented in the second part of this work are performed with a hybrid N-body / SPH method. Beside the SPH method, there are also other possibilities in simulating the gas phase. There are several similar so-called grid based simulation types, e.g. the Eulerian hydrohynamic method with an uniform Cartesian grid presented by Wada & Norman (2001), Wada & Norman 2007, Wada (2008). This method solves the mass, energy and momentum conservation equations and the Poisson equation for the gas. The entire disc is devided into grid cells with e.g. $512 \times 512 \times 64$ grid points. Compared to the present alternative simulation types, GADGET-2 is the most powerful simulation package since it is able to simulate the dynamics of different types of particles with transformations between the particle types. The resolution problem is a general numerical problem and not only limited to GADGET-2. Therefore, an advance in this field of study can only be reached if high-performing computation is further improved.

A

Real stationary dispersion relation

Our main purpose is to establish relations between dark matter halo (represented by the ratio f) and an isopedic magnetic field in the gaseous disc (represented by the isopedic ratio λ). For the two cases of $\beta_1^d = \beta_1 = \beta$ (with $\nu = 0$) and of $\beta_1 = 1/4$ (with $\nu \neq 0$), we show in the following that M and Y_m as defined by Equations (2.91) and (2.37) become real numbers. In literature, $\beta_1^d = \beta$ is called the aligned case since the radial wavenumber parameter ν vanishes in this case and only azimuthal, but no radial wave variations are present. In this case, we have

$$M = \frac{m^2 - 2(1-\beta)}{m^2 + 4\beta(1-\beta)} \,, \tag{A.1}$$

$$Y_m(\beta) = \frac{\pi\Gamma(m/2 - \beta + 1/2)\Gamma(m/2 + \beta)}{\Gamma(m/2 - \beta + 1)\Gamma(m/2 + \beta + 1/2)} \,. \tag{A.2}$$

For $\nu \neq 0$ and thus a complex β_1^d, the general expressions for M and $Y_m(\beta_1^d)$ are

$$M = \frac{m^2 - 2(1-\beta)}{m^2 + 2(\beta + \beta_1 - 2\beta_1^2 + \nu^2/2) + i\nu(4\beta_1 - 1)} \,, \tag{A.3}$$

$$Y_m(\beta_1^d) = \frac{\pi\Gamma(m/2 - \beta_1 + i\nu/2 + 1/2)\Gamma(m/2 + \beta_1 - i\nu/2)}{\Gamma(m/2 - \beta_1 + i\nu/2 + 1)\Gamma(m/2 + \beta_1 - i\nu/2 + 1/2)} \,. \tag{A.4}$$

By setting $\beta_1 = 1/4$ in expressions (A.3) and (A.4), we get

$$M = \frac{m^2 - 2(1-\beta)}{m^2 + 2\beta + 1/4 + \nu^2} \,, \tag{A.5}$$

$$Y_m(\beta_1^d) = \left| \frac{\Gamma(m/2 + 1/4 + i\nu/2)}{\Gamma(m/2 + 3/4 + i\nu/2)} \right|^2 \,. \tag{A.6}$$

Expression (A.6) is based on the relation $\Gamma(z)^* = \Gamma(z^*)$ for Gamma-function where * denotes the complex conjugate operation. For these two cases $\beta_1^d = \beta_1 = \beta$ (with $\nu = 0$) and of $\beta_1 = 1/4$ (with $\nu \neq 0$ in general), we numerically explore the behaviour $f(\lambda)$ by specifying other relevant model parameters.

B

Dependence of gravity potential ratio f on perturbation orders m

Here, we briefly describe the gravitational potential ratio f as a function for different m values and provide an upper limit for the difference of $f(m+2) - f(m)$. In general, the function f depends on m through functional parameters M and $Y_m(\beta_1^d)$. In the limit of $m \to \infty$, we have $M \to 1$ and therefore the difference $\Delta M = M(m+1) - M(m) \to 0$. For the property of functional parameter $Y_m(\beta_1^d)$, the property of Gamma-function is first discussed. For Gamma functions, the well-known recursion formula is

$$\Gamma(x+1) = x\Gamma(x) \,, \tag{B.1}$$

which leads to the following four relations

$$\Gamma((m+2)/2 - \beta_1^d + 1/2) = (m/2 - \beta_1^d + 1/2)\Gamma(m/2 - \beta_1^d + 1/2) \,, \tag{B.2}$$

$$\Gamma((m+2)/2 + \beta_1^d) = (m/2 + \beta_1^d)\Gamma(m/2 + \beta_1^d) \,, \tag{B.3}$$

$$\Gamma((m+2)/2 - \beta_1^d + 1) = (m/2 - \beta_1^d + 1)\Gamma(m/2 - \beta_1^d + 1) \,, \tag{B.4}$$

$$\Gamma((m+2)/2 + \beta_1^d + 1/2) = (m/2 + \beta_1^d + 1/2)\Gamma(m/2 + \beta_1^d + 1/2) \tag{B.5}$$

as applied to our case under consideration. Therefore, we have

$$Y_{m+2}(\beta_1^d) = \frac{\left(m - 2\beta_1^d + 1\right)\left(m + 2\beta_1^d\right)}{\left(m - 2\beta_1^d + 2\right)\left(m + 2\beta_1^d + 1\right)} Y_m(\beta_1^d) \,. \tag{B.6}$$

For $m \to \infty$, it follows that $Y_{m+2}(\beta_1^d) \to Y_m(\beta_1^d)$, indicating the difference $\Delta Y_m(\beta_1^d) = Y_{m+2}(\beta_1^d) - Y_m(\beta_1^d) \to 0$. Based on these analyses, we conclude that for very large values of m

there is no significant difference between $f(m+2)$ and $f(m)$, and therefore $f(m+2) \to f(m)$ in the limit of large m values.

For $m = 2$, Equations (2.91) and (B.6) lead to

$$M(4) - M(2) = \frac{7+\beta}{8 - 2(\beta_1^d)^2 + \beta_1^d + \beta} - \frac{1+\beta}{2 - 2(\beta_1^d)^2 + \beta_1^d + \beta}\,, \tag{B.7}$$

$$Y_4(\beta_1^d) - Y_2(\beta_1^d) = \left[\frac{(3-2\beta_1^d)(1+\beta_1^d)}{(2-\beta_1^d)(3+2\beta_1^d)} - 1\right] Y_2(\beta_1^d) = \left[\frac{3+\beta_1^d - 2(\beta_1^d)^2}{6+\beta_1^d - 2(\beta_1^d)^2} - 1\right] Y_2(\beta_1^d) \equiv N Y_2(\beta_1^d)\,. \tag{B.8}$$

They define the coefficient N as a function of β_1^d that is complex for $\nu \neq 0$. The difference

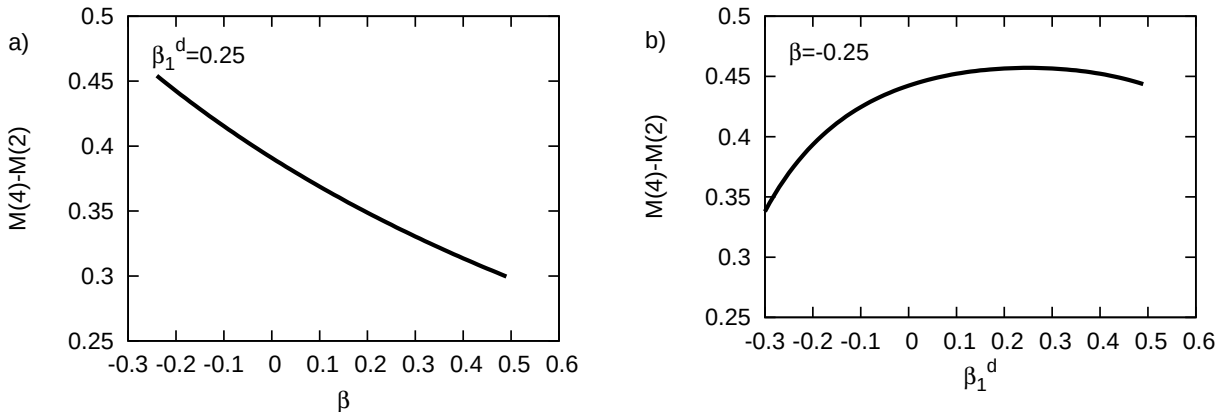

Figure B.1: In a), the difference of $M(4) - M(2)$ is shown as a function of β and $\beta_1^d = 0.25$, with a maximum at $\beta = -0.25$; for a real value of β_1^d, the difference $M(4) - M(2)$ appears to be a monotonically decreasing function with increasing β value. In b), the difference of $M(4) - M(2)$ is shown as a function of β_1^d and $\beta = -0.25$. A maximum value can be readily identified.

$M(4) - M(2)$ is a function of both β and β_1^d. The largest difference is found for $\beta = -0.25$ and $\beta_1^d \sim 0.2 - 0.3$ with $\Delta M \equiv M(4) - M(2) = 0.46$ (see Figure B.1). In a), the difference of $M(4) - M(2)$ is shown as a function of β with a fixed real β_1^d, with a maximum at $\beta = -0.25$ and $\beta_1^d = 0.25$; for a real value of β_1^d, the difference $M(4) - M(2)$ appears to be a monotonically decreasing function with increasing β value. In b), the difference of $M(4) - M(2)$ is shown as a function of real β_1^d values with a fixed value $\beta = -0.25$. A maximum value can be readily identified. For applications to spiral galaxies, only positive β values are physically relevant. But for a theoretical consideration, a negative β is allowed to estimate limits. To conclude, we obtain $\Delta M \leq 0.46$. For a real range of $\beta_1^d \in [-0.5, 0.5]$ with $\nu = 0$ and $\beta = 0.25$, functional parameter

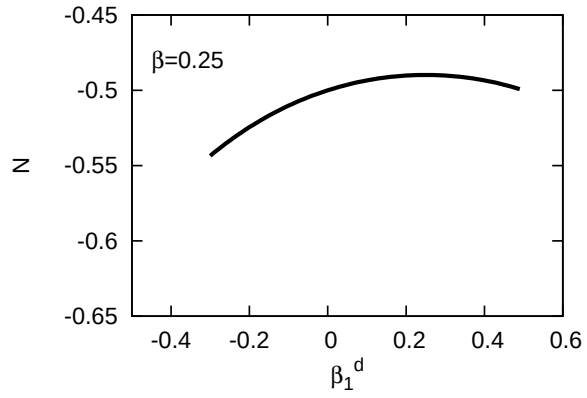

Figure B.2: Variation of $N(\beta_1^d)$ defined by Equation (B.8) as a function of real β_1^d values and $\beta = 0.25$.

$N(\beta_1^d)$ is plotted in Figure B.2. The smallest N is -0.6 for $\beta_1^d = -0.5$. From Equation (B.6), one can also see that $Y_{m+2}(\beta_1^d)$ is always smaller than $Y_m(\beta_1^d)$. This fact explains the negative values shown in Figure B.2. For the absolute difference, we get inequality

$$|\Delta Y_m| = |Y_{m+2} - Y_m| \leq 0.6 Y_m \; . \tag{B.9}$$

In contrast to ΔM, which can be determined as a constant, ΔY_m is a function of Y_m. For Δf, the upper limit is $f(4) - f(2)$, which is different each time depending on the chosen parameters. As a result, the difference of two functions $f(n)$ and $f(n+2)$ with $n = m, m+1, \cdots$ goes towards zero, namely

$$f(m+2) - f(m) \to 0 \qquad \text{for} \qquad m \to \infty \; . \tag{B.10}$$

$$f(m+3) - f(m+1) \to 0 \qquad \text{for} \qquad m \to \infty \; . \tag{B.11}$$

List of Figures

List of Tables

Bibliography

Adams F. C. (2003). Star formation and the stellar initial mass function. *Publications of the Astronomical Observatory of Belgrade 75*, 9-15

Balsara D. S. (1995). von Neumann stability analysis of smooth particle hydrodynamics–suggestions for optimal algorithms. *Journal of Computational Physics 121*, 357-372

Balbus S. A. (2003). Enhanced Angular Momentum Transport in Accretion Disks. *Annual Review of Astronomy and Astrophysics 41*, 555-597

Balbus S. A., Hawley J. F. (1991). A powerful local shear instability in weakly magnetized disks. I - Linear analysis. II - Nonlinear evolution. *The Astrophysical Journal 376*, 214-233

Balbus S. A., Hawley J. F. (1998). Instability, turbulence and enhanced transport in accretion disks. *Reviews of Modern Physics 70*, 1-53

Baldwin J. E., Lynden-Bell D., Sancisi R. (1980). Lopsided galaxies. *Monthly Notes of the Royal Astronomical Society 193*, 313-319

Beck R., Brandenburg A., Moss D., Shukorov A., Sokoloff D. (1996). Galactic Magnetism: Recent Developments and Perspectives. *Annual Review of Astronomy and Astrophysics 34*, 155-206

Bertin G., Lin C. C. (1996). *Spiral Structure in Galaxies*, MIT Press, Cambridge, MA

Binney J., Tremaine S. (1987). *Galactic Dynamics*, Princeton Univ. Press, Princeton

Bonnell I. A., Larson R. B., Zinnecker H. (2007). The Origin of the Initial Mass Function. *Protostars and Planets*, V, B. Reipurth, D. Jewitt, and K. Keil (eds.), University of Arizona Press, Tucson, 149-164

Brouillet N., Kaufman M., Combes F., Baudry A., Bash F. (1998). Identification of molecular complexes in M81. *Astronomy & Astrophysics 333*, 92-100

Brown J. C., Taylor A. R., Wielebinski R., Mueller P. (2003). On Large-Scale Magnetic Field Reversals in the Outer Galaxy. *The Astrophysical Journal*, 592, L29-L32

Chakrabarti S., Laughlin G., Shu F. H. (2003). Branch, Spur, and Feather Formation in Spiral Galaxies. *The Astrophysical Journal 596*, 220-239

Chandrasekhar S. (1960). The Stability of Non-Dissipative Couette Flow in Hydromagnetics. *Proceedings of the National Academy of Sciences of the United States of America 46*, 253-257

Diemand J., Kuhlen M., Madau P., Zemp M., Moore B., Potter D., Stadel J. (2008). Clumps and streams in the local dark matter distribution. *Nature 454*, 735-738

Cox D. P., Gomez G. C. (2002). Analytical expressions for spiral arm gravitational potential and density. *The Astrophysical Journal Supplement Series 142*, 261-267

Dehnen W., Binney J. (1998). Mass models for the Milky Way. *Monthly Notes of the Royal Astronomical Society 294*, 429-438

Digel S. W., Lyder D. A., Philbrick A. J., Puche D., Thaddeus P. (1996). A Large-Scale CO Survey toward W3, W4, and W5. *The Astrophysical Journal 458*, 561-575

Dobbs C. L., Bonnell I. A. (2007). Spiral shocks and the formation of molecular clouds in a two-phase medium. *Monthly Notes of the Royal Astronomical Society 376*, 1747-1756

Dobbs C. L., Bonnell I. A. (2008). Simulations of spiral galaxies with an active potential: molecular cloud formation and gas dynamics. *Monthly Notes of the Royal Astronomical Society 385*, 1893-1902

Dobbs C. L., Bonnell I. A., Pringle J. E. (2006). The formation of molecular clouds in spiral galaxies. *Monthly Notes of the Royal Astronomical Society 371*, 1663-1674

Dobbs C. L., Theis C., Pringle J. E., Bate M. R. (2009). Hydrodynamic Simulations of M51 and the interaction with NGC 5195. astro-ph/09083599

Elmegreen B. G. (2000). Two stellar mass functions combined into one by the random sampling model of the initial mass function. *Monthly Notes of the Royal Astronomical Society 311*, L5-L8

Fan Z. H., Lou Y.-Q. (1997). Swing amplification of fast and slow density waves in thin magnetized gaseous discs. *Monthly Notes of the Royal Astronomical Society*, 291, 91-109

Gerritsen J. P. E. (1997). PhD thesis, Kapetyn Astronomical Institute

Gerola H., Seiden P. E. (1978). Stochastic star formation and spiral structure of galaxies. *The Astrophysical Journal 223*, 129-139

Gingold R. A., Monaghan J. J. (1977). Smoothed particle hydrodynamics - Theory and application to non-spherical stars. *Monthly Notes of the Royal Astronomical Society 181*, 375-389

Gittins D. M., Clarke C. J. (2004). Constraining corotation from shocks in tightly wound spiral galaxies. *Monthly Notes of the Royal Astronomical Society 349*, 909-921

Goldreich P., Tremaine S. (1979). The excitation of density waves at the Lindblad and corotation resonances by an external potential. *The Astrophysical Journal 233*, 857-871

Griv E., Chiueh T. (1994). The weakly nonlinear theory of density waves in a stellar disk. *Physica A 205*, 299-306

Heyer M. H., Terebey S. (1998). The Anatomy of the Perseus Spiral Arm: 12CO and IRAS Imaging Observations of the W3-W4-W5 Cloud Complex. *The Astrophysical Journal 502*, 265-277

Katz N. (1992). Dissipational galaxy formation 2. Effects of star formation. *The Astrophysical Journal 391*, 502-517

Katz N., Weinberg D.H., Hernquist L. (1996). Cosmological simulations with TreeSPH. *The Astrophysical Journal Supplement Series 105*, 19-35

Kendall S., Kennicutt R. C., Clarke C., Thornley M. D. (2008). Tracing spiral density waves in M81. *Monthly Notes of the Royal Astronomical Society 387*, 1007-1020

Kim W., Ostriker E. C. (2001). Amplification, saturation, and Q thresholds for runaway: Growth of self-gravitating structures in models of magnetized galactic gas disks. *The Astrophysical Journal*, 559, 70-95

Kim W., Ostriker E. C., Stone J. M. (2002). Three-dimensional Simulations of Parker, Magneto-Jeans, and Swing Instabilities in Shearing Galactic Gas Disks. *The Astrophysical Journal 581*, 1080-1100

Li Y., Mac Low M., Klessen R.S. (2005). Star formation in isolated disk galaxies I. Models and characteristics of nonlinear gravitational collapse. *The Astrophysical Journal*, 626, 823-843

Li Z.-Y., Shu F. H. (1996). Interaction of Wide-Angle MHD Winds with Flared Disks. *The Astrophysical Journal 468*, 261-268

Lin C. C., Shu F. H. (1964). On the Spiral Structure of Disk Galaxies. *The Astrophysical Journal 140*, 646-655

Lin C. C., Shu F. H. (1966). On the Spiral Structure of Disk Galaxies, II. Outline of a Theory of Density Waves. *Proceedings of the National Academy of Sciences of the United States of America 55*, 229-234

Lizano S., Shu F. H. (1989). Molecular cloud cores and bimodal star formation. *The Astrophysical Journal 342*, 834-854

Lou Y.-Q., Bai X. N. (2006). Global structures in a composite system of two scale-free discs with a coplanar magnetic field. *Monthly Notes of the Royal Astronomical Society 372*, 81-112

Lou Y.-Q., Fan Z. H. (1998). Coupled galactic density-wave modes in a composite system of thin stellar and gaseous discs. *Monthly Notes of the Royal Astronomical Society 297*, 84-100

Lou Y.-Q., Fan Z. H. (2000). Large-scale magnetohydrodynamic density-wave structures in the Andromeda nebula. *Monthly Notes of the Royal Astronomical Society 315*, 646-654

Lou Y.-Q., Shen Y. (2003). Perturbation configurations in a two-fluid system of singular isothermal discs. *Monthly Notes of the Royal Astronomical Society 343*, 750-770

Lou Y.-Q., Wu Y. (2005). Global perturbation configurations in a composite disc system with an isopedic magnetic field. *Monthly Notes of the Royal Astronomical Society 364*, 475-502

Lou Y.-Q., Zou Y. (2004). Stationary perturbation configurations in a composite system of stellar and coplanarly magnetized gaseous singular isothermal discs. *Monthly Notes of the Royal Astronomical Society 350*, 1220-1252

Lou Y.-Q., Zou Y. (2006). Axisymmetric stability criteria for a composite system of stellar and magnetized gaseous singular isothermal discs. *Monthly Notes of the Royal Astronomical Society 366*, 1037-1049

Lucy L. B. (1977). A numerical approach to the testing of the fission hypothesis. *Astrophysical Journal 82*, 1013-1024

Lynden-Bell D., Lemos J. P. S. (1999). Equiangular spiral modes of power law disks. (astro-ph/9907093)

Miller G. E., Scalo J. M. (1979). The initial mass function and stellar birthrate in the solar neighborhood. *The Astrophysical Journal Supplement Series 41*, 513-547

Monaghan J. J., Gingold R. A. (1983). Shock Simulation by the Particle Method SPH. *Journal of Computational Physics 52*, 374

Monaghan J. J. (1997). SPH and Riemann Solvers. *Journal of Computational Physics 136*, 298-307

Monaghan J. J. (1992). Smoothed particle hydrodynamics. *Annual Review of Astronomy and Astrophysics 30*, 543-574

Nakano T. (1979). Quasistatic Contraction of Magnetic Protostars due to Magnetic Flux Leakage - Part One - Formulation and an Example. *Astronomical society of Japanese Publications 31*, 697-712

Oh Sang Hoon, Kim Woong-Tae, Lee Hyung Mok (2008). Physical Properties of Tidal Features in Interacting Disk Galaxies. *The Astrophysical Journal 683*, 94-142

Oort J. H. (1962). Spiral Structure. *The Distribution and Motion of Interstellar Matter in Galaxies*, ed. L. Woltjer (New York: W. A. Benjamin, Inc), 234-244

Ostriker J. P., Peebles P. J. E. (1973). A Numerical Study of the Stability of Flattened Galaxies: or, can Cold Galaxies Survive? *The Astrophysical Journal 186*, 467-480

Ostriker J. P., Peebles P. J. E., Yahil A. (1974). The size and mass of galaxies, and the mass of the universe. *The Astrophysical Journal 193*, L1-L4

Persic M. & Salucci P. (1988). Dark and visible matter in spiral galaxies. *Monthly Notes of the Royal Astronomical Society 234*, 131-154

Persic M., Salucci P., Stel F. (1996). The universal rotation curve of spiral galaxies - I. The dark matter connection. *Monthly Notes of the Royal Astronomical Society 281*, 27-47

Price D. J. (2007). splash: An Interactive Visualisation Tool for Smoothed Particle Hydrodynamics Simulations. *Publications of the Astronomical Society of Australia 24*, 159-173

Qian E. (1992). Potential-density pairs for flat discs. *Monthly Notes of the Royal Astronomical Society 257*, 581-592

Roberts M. S. (1962). The neutral hydrogen content of late-type spiral galaxies. *Astronomical Journal 67*, 437-446

Safronov V. S. (1960). On the gravitational instability in flattened systems with axial symmetry and non-uniform rotation. *Annales d'Astrophysique 23*, 979-983

Shen Y., Liu X., Lou Y.-Q. (2005). Structures in a class of magnetized scale-free discs. *Monthly Notes of the Royal Astronomical Society 356*, 1333-1356

Shen Y., Lou Y.-Q. (2004). Gravitationally coupled scale-free discs. *Monthly Notes of the Royal Astronomical Society 353*, 249-269

Shetty R., Ostriker E. C. (2006). Global Modeling of Spur Formation in Spiral Galaxies. *The Astrophysical Journal 647*, 997-1017

Shu F.-H., Laughlin G., Lizano S., Galli D. (2000). Singular Isothermal Disks. I. Linear Stability Analysis. *The Astrophysical Journal 535*, 190-210

Shu F.-H., Li Z.-Y. (1997). Magnetic Forces in an Isopedic Disk. *The Astrophysical Journal 475*, 251-259

Sofue Y., Fujimoto M., Wielebinski R. (1986). Global structure of magnetic fields in spiral galaxies. *Annual Review of Astronomy and Astrophysics 24*, 459-497

Springel V. (2005). The cosmological simulation code GADGET-2. *Monthly Notes of the Royal Astronomical Society 364*, 1105-1134

Springel V., Yoshida N., White S. D. M. (2001). GADGET: a code for collisionless and gasdynamical cosmological simulations. *New Astronomy 6*, 79-117

Steinmetz M. (1996). GRAPESPH: cosmological smoothed particle hydrodynamics simulations with special-purpose hardware GRAPE. *Monthly Notes of the Royal Astronomical Society*, 278, 1005-1017

Suto Y., Silk J. (1988). Self-similar dynamics of polytropic gaseous spheres. *The Astrophysical Journal 326*, 527-538

Syer D., Tremaine S. (1996). Non-axisymmetric, scale-free, razor-thin discs. *Monthly Notes of the Royal Astronomical Society 281*, 925-936

Thacker R. J., Couchman H. M. P. (2000). Implementing Feedback in Simulations of Galaxy Formation: A Survey of Methods. *The Astrophysical Journal 545*, 728-752

Toomre A. (1964). On the gravitational stability of a disk of stars. *The Astrophysical Journal 139*, 1217-1238

Toomre A. (1969). Group velocity of spiral waves in galactic disks. *The Astrophysical Journal 158*, 899-914

Toomre A. (1981). The Structure and Evolution of Normal Galaxies, eds. S.M. Fall & D. Lynden-Bell, Cambridge: Cambridge Univ. Press, 111

Toomre A., Toomre J. (1972). Galactic bridges and tails. *The Astrophysical Journal 178*, 623-666

Visser H. C. D. (1980a). The dynamics of the spiral galaxy M81. I - Axisymmetric models and the stellar density wave. *Astronomy & Astrophysics 88*, 149-158

Visser H. C. D. (1980b). The dynamics of the spiral galaxy M81. II - Gas dynamics and neutral-hydrogen observations. *Astronomy & Astrophysics 88*, 159-174

Vogel S. N., Kulkarni S. R., Scoville N. Z. (1988). Star formation in giant molecular associations synchronized by a spiral density wave. *Nature 334*, 402-406

Wada K. (2008). Instabilities of Spiral Shocks. II. A Quasi-Steady State in the Multiphase Inhomogeneous ISM. *The Astrophysical Journal 675*, 188-193

Wada K. & Norman C. A. (2001). Numerical models of the multiphase interstellar matter with stellar energy feedback on a galactic scale. *The Astrophysical Journal 547*, 172-186

Wada K. & Norman C. A. (2007). Density Structure of the Interstellar Medium and the Star Formation Rate in Galactic Disks. *The Astrophysical Journal 660*, 276-287

Wentzel D. G. (1963). Magnetic Fields and Spiral Structure. *Annual Review of Astronomy and Astrophysics 1*, 195-218

Wu Y., Lou Y.-Q. (2006). Scale-free thin discs with an isopedic magnetic field. *Monthly Notes of the Royal Astronomical Society 372*, 992-1018

Yoshida N., Sokasian A., Hernquist L., Springel V. (2003). Early Structure Formation and Reionization in a Warm Dark Matter Cosmology. *The Astrophysical Journal 591*, L1-L4

Zhang S. J., Jin J. M. (1996). *Computation of Special Functions*, John Wiley & Sons, New York

Zweibel E. G., Heiles C. (1997). Magnetic fields in galaxies and beyond. *Nature 385*, 131-136

Acknowledgment

- Zuerst möchte ich mich bei Prof. Dr. Wolfgang J. Duschl für die Betreuung dieser Arbeit bedanken und auch für seine Unterstützung und Hilfe bei allen vergangenen und gegenwärtigen Problemen.
- Ich danke Prof. Dr. Holger Kersten für die Erstellung des Zweitgutachtens.
- I would like to thank Prof. Yu-Qing Lou from the Tsinghua University, P.R. China, for his hospitality in China and for our successful collaboration.
- Der Studienstiftung des deutschen Volkes danke ich für die finanzielle Unterstützung während meiner Promotion, insbesondere durch das Programm „Zeit gegen Geld“.
- Ich danke dem Deutschen Akademischen Austauschdienst (DAAD) für die finanzielle Hilfe während meines Forschungsaufenthaltes in Beijing, V.R. China.
- Ich möchte mich besonders bei meinem ehemaligen Physiklehrer Herrn Rockenbach vom Herzog-Johann-Gymnasium in Simmern bedanken. Bereits sehr früh wurde mein Interesse an der Physik und vor allem an der Astronomie geweckt, doch erst durch den spannenden und anspruchsvollen Physikunterricht in der Oberstufe hat Herr Rockenbach mich in die wahre Welt der Physik geführt.
- Ich danke allen meinen Kolleginnen und Kollegen am Institut, mit denen ich interessante Diskussionen geteilt habe.
- Besonders möchte ich mich bei Dr. Simone Knief vom Universitäts-Rechenzentrum und bei unserem Systemadministrator Holger Boll für ihre große Hilfe bei allen aufgetretenen Computer- und Softwareproblemen bedanken. Ebenfalls danke ich Frau Birgit Kuhr für die reibungslose Bearbeitung aller organisatorischen Angelegenheiten.
- Meiner Mutter Dr. Xi Sun und meinem Vater Prof. Guanqi Xiang danke ich aus tiefstem Herzen für alles, was sie bis heute für mich getan haben. Diese Arbeit konnte nur mit ihrer Hilfe fertig gestellt werden und ist ihnen gewidmet.
- Meiner Schwester Ying Xiang danke ich für einige anregende Diskussionen und Korrekturen der Doktorarbeit. Ich danke meinen jüngeren Schwestern Mai und Ting für ihre moralische Unterstützung auf diesem schweren Weg. Ting danke ich besonders für ihre Zeit und Geduld mit meinen Kindern.

- Ich danke meinen Schwiegereltern Margret und Heinz Grüß für ihre Hilfe während der letzten Jahre.
- Jürgen Sailer, Andreas Walker und Mai Xiang danke ich für das Korrekturlesen der Doktorarbeit.
- Am Ende möchte ich mich bei meinem Mann Simon Grüß und meinen Kindern Katharina und Leopold Grüß bedanken, die mich die letzten Jahre begleitet haben und das Leben für mich zwar anstrengender, dafür aber auch schöner und lebenswerter gemacht haben.

Eidesstattliche Erklärung

Hiermit erkläre ich an Eides statt, dass die vorliegende Promotionsarbeit - abgesehen von der Beratung durch meine wissenschaftlichen Betreuer - nach Inhalt und Form meine eigene Arbeit ist.

Sie wurde weder ganz noch in Teilen an anderer Stelle im Rahmen eines Prüfungsverfahrens vorgelegt.

Teile dieser Arbeit wurden bei der Zeitschrift *Monthly Notices of the Royal Astronomical Society* veröffentlicht.

Kiel, September 2009

.....

(Meng Xiang-Grüß)